FINITE ELEMENT ANALYSES OF ELECTROMAGNETIC FORCES AND THERMAL STRESS EFFECTS ON TRANSFORMER WINDING DUE TO SWITCHING IMPULSE VOLTAGE

By

NURUL FARAHWAHIDA BT MD YASID

Thesis Submitted to the School of Graduate Studies, Universiti Putra Malaysia, in Fulfilment of the Requirements for Degree of Doctor of Philosophy

January 2025

FK 2025 6

© COPYRIGHT UPM

All material contained within the thesis, including without limitation text, logos, icons, photographs and all other artwork, is copyright material of Universiti Putra Malaysia unless otherwise stated. Use may be made of any material contained within the thesis for non-commercial purposes from the copyright holder. Commercial use of material may only be made with the express, prior, written permission of Universiti Putra Malaysia.

Copyright © Universiti Putra Malaysia

© COPYRIGHT UPM

Abstract of thesis presented to the Senate of Universiti Putra Malaysia in fulfilment of the requirement for the degree of Doctor of Philosophy

FINITE ELEMENT ANALYSES OF ELECTROMAGNETIC FORCES AND THERMAL STRESS EFFECTS ON TRANSFORMER WINDING DUE TO SWITCHING IMPULSE VOLTAGE

By

NURUL FARAHWAHIDA BT MD YASID

January 2025

Chairman : Norhafiz bin Azis, PhD
Faculty : Engineering

Recurrence switching impulses in power system induce overvoltage attenuation along a transformer winding, leading to abnormal stresses. This study presents a comprehensive approach using Finite Element Method (FEM) to analyse the behaviour of a 33/11 kV disc-type winding under recurrence switching impulses. Firstly, the effects of standard switching impulse (SSI) and non-standard switching impulse (NSSI) voltages on electromagnetic forces were examined based on analytical and numerical methods. The electromagnetic forces were calculated analytically based on the winding's geometrical design and numerical simulations were conducted in Ansys Maxwell. Structural analysis was conducted in Ansys Workbench to evaluate the impact of these forces on disc windings. Then, the interrelated electrical, thermal and structural response of disc winding under SSI voltage were analysed. Ohmic losses were computed through electric transient analysis and transferred to thermal analysis to determine temperature distribution and

© COPYRIGHT UPM

thermal stress. The thermal stress was used in structural analysis to assess disc winding deformation and displacement. Buckling analysis was conducted to evaluate winding stability, while stress-strain and load-displacement curves to examine the mechanical behaviour of the winding materials. Lastly, a safety factor analysis was conducted to assess the disc winding's structural reliability to electromagnetic forces and thermal effects. The electromagnetic force analysis shows that the highest force experienced by the disc winding is the axial force that reached 207 mN under NSSI voltage, approximately five times greater than under SSI voltage. SSI voltage results in localised hoop tension, axial displacement and conductor tilt, while NSSI causes similar deformation and displacement but on a global scale. The ohmic losses are unevenly distributed across the winding, with high concentrations at the topmost disc layers and outer circumference with hot-spot temperature of 428.6 °C. This leads to significant temperature and substantial structural deformations in that area. The thermal stress causes copper conductors to expand and form wavy bends. The fixed supports exert pressure as it restrain the expansion of the conductors and cause a bend. Kraft insulation paper deformations include crinkles, distortion and tears. The buckling analysis indicates localised instability at the top disc and winding circumferences under electromagnetic force while thermal dependent buckling leads to global instability. The safety factor analysis highlights critical stress levels under thermal effects, with values as low as 0–1, that indicate a high risk of mechanical failure.

Keywords: electromagnetic force, resonance, switching, transformer, transient, thermal

SDG: GOAL 4: Quality Education, GOAL 9: Industry, innovation and infrastructure

© COPYRIGHT UPM

Abstrak tesis yang dikemukakan kepada Senat Universiti Putra Malaysia
sebagai memenuhi keperluan untuk ijazah Doktor Falsafah

ANALISIS ELEMEN TERHINGGA TERHADAP KESAN DAYA ELEKTROMAGNET DAN TEKANAN TERMA PADA LILITAN PENGUBAH AKIBAT VOLTAN IMPULS PENGHIDUPAN

Oleh

NURUL FARAHWAHIDA BT MD YASID

Januari 2025

Pengerusi : Norhafiz bin Azis, PhD
Fakulti : Kejuruteraan

Pendedahan berulang impuls penghidupan dalam system kuasa mendorong pegaliran lebihan voltan sepanjang lilitan pengubah yang membawa kepada tekanan yang tidak normal. Kajian ini membentangkan pendekatan menyeluruh menggunakan Kaedah Unsur Terhingga (FEM) untuk menganalisis tingkah laku penggulungan jenis cakera 33/11 kV di bawah impuls penghidupan berulang. Pertama, kesan voltan impuls penghidupan standard (SSI) dan impuls penghidupan tidak standard (NSSI) diperiksa berdasarkan kaedah analitik dan numerik. Daya elektromagnetik dikira secara analitik berdasarkan reka bentuk geometri penggulungan, manakala simulasi numerik dijalankan menggunakan Ansys Maxwell. Analisis struktur dilakukan di Ansys Workbench untuk menilai kesan daya ini keatas konduktor penggulungan cakera. Seterusnya, tindak balas elektrik, terma dan struktur penggulungan cakera di bawah voltan SSI telah dianalisis. Kehilangan ohmik

© COPYRIGHT UPM

dikira menggunakan analisis transien elektrik dan dipindahkan ke analisis terma untuk menentukan taburan suhu dan tekanan terma. Tekanan terma ini kemudiannya digunakan dalam analisis struktur untuk menilai ubah bentuk dan anjakan penggulungan cakera. Analisis lekuk dilakukan untuk menilai kestabilan penggulungan, manakala lengkung tegasan-regangan dan anjakan beban digunakan untuk mengkaji tingkah laku mekanikal bahan penggulungan. Akhir sekali, analisis faktor keselamatan dijalankan bagi menilai kebolehpercayaan struktur penggulungan terhadap daya elektromagnet dan kesan terma. Analisis daya elektromagnet menunjukkan bahawa daya tertinggi yang dialami oleh lilitan cakera ialah daya paksi, yang mencapai 207 mN dibawah voltan NSSI, kira-kira lima kali lebih besar berbanding dibawah voltan SSI. Voltan SSI menyebabkan ketegangan lingkaran setempat, anjakan paksi, dan kecondongan konduktor, manakala NSSI menyebabkan ubah bentuk dan anjakan yang serupa tetapi pada skala global. Kajian ini menunjukkan bahawa kehilangan ohmik tidak diedarkan secara sekata di seluruh lilitan, dengan kepekatan tinggi pada lapisan cakera paling atas dan lilitan bahagian luar dengan suhu titik panas mencapai 428.6 °C. Pengedaran yang tidak sekata ini membawa kepada peningkatan suhu yang ketara dan ubah bentuk struktur yang besar pada bahagian tersebut. Tekanan terma menyebabkan konduktor tembaga mengembang dan membentuk lekuk beralun. Sokongan tetap mengenakan tekanan kerana ia menahan pengembangan konduktor, menyebabkan ia membengkok. Kertas penebat kraft mengalami kedutan, distorsi dan koyakankan. Analisis lekukan menunjukkan ketidakstabilan setempat di cakera atas dan lilitan penggulungan di bawah daya elektromagnet, manakala lekuk bergantung

© COPYRIGHT UPM

kepada terma menyebabkan ketidakstabilan berskala global. Analisis faktor keselamatan menonjolkan tahap tekanan kritikal di bawah kesan terma, dengan nilai serendah 0–1, menunjukkan risiko kegagalan mekanikal yang tinggi.

Kata Kunci: daya elektromagnetik, resonans, penghidupan, pengubah, peralihan, terma

SDG: MATLAMAT 4: Pendidikan Berkualiti, MATLAMAT 9: Industri, inovasi dan infrastruktur

© COPYRIGHT UPM

ACKNOWLEDGEMENTS

First and foremost, I would like to express my sincere gratitude to my supervisor, Assoc. Prof. Ir. Dr. Norhafiz Azis, for his unwavering support, expert guidance and encouragement throughout this research. His investment of time and effort, along with his constructive criticism have been valuable to my development as a researcher. I would like to thank the rest of the supervisory committee, Assoc. Prof. Dr. Jasronita Jasni, Assoc. Prof. Ir. Dr. Mohd Fairouz bin Mohd Yousof and Ir. Dr. Mohd Aizam Talib for their valuable insights and assistance.

I would like to express my deepest gratitude to my family for their unwavering emotional and financial support as well as encouragement throughout my journey in pursuing this PhD. Their love and belief in my abilities have been a constant source of motivation.

Special thanks go to my colleagues and peers for the insightful discussions, advice and camaraderie that made this journey enjoyable and fulfilling. Lastly, I would like to acknowledge everyone who contributed directly or indirectly to this thesis. Your efforts are deeply appreciated.

© COPYRIGHT UPM

This thesis was submitted to the Senate of Universiti Putra Malaysia and has been accepted as fulfilment of the requirement for the degree of doctor of philosophy. The members of the Supervisory Committee were as follows:

Norhafiz bin Azis, PhD
Associate Professor, Ir
Faculty of Engineering
Universiti Putra Malaysia
(Chairman)

Jasronita binti Jasni, PhD
Associate Professor
Faculty of Engineering
Universiti Putra Malaysia
(Member)

Mohd Fairouz bin Mohd Yousof, PhD
Associate Professor, Ir
Faculty of Electrical and Electronics Engineering,
Universiti Tun Hussein Onn Malaysia
(Member)

Mohd Aizam bin Talib, PhD
Head, Ir, Ts
Advanced Diagnostic Services
TNB Labs Sdn Bhd
(Member)

ZALILAH BINTI MOHD SHARIFF, PhD
Professor and Dean
School of Graduate Studies
Universiti Putra Malaysia

Date: 8 May 2025

© COPYRIGHT UPM

TABLE OF CONTENTS

© COPYRIGHT UPM

© COPYRIGHT UPM

© COPYRIGHT UPM

LIST OF TABLES

© COPYRIGHT UPM

LIST OF FIGURES

© COPYRIGHT UPM

© COPYRIGHT UPM

© COPYRIGHT UPM

© COPYRIGHT UPM

LIST OF ABBREVIATIONS

AC	Alternating current
ATP	Alternative Transient Program
BIL	Basic Impulse Level
ºC	Degree Celsius
CCF	Correlation Coefficient Factor
CIGRE	International Council on Large Electric Systems
EMI	Electromagnetic interference
EMTP	Electromagnetic Transient Program
F_a	Axial force
F_r	Radial force
FEM	Finite Element Method
FTA	Fault Tree Analysis
HV	High voltage
IEC	International Electrotechnical Commission
IEEE	Institute of Electrical and Electronics Engineers
LV	Low voltage
NSSI	Non-standard Switching Impulse
SF	Safety factor
SSI	Standard Switching Impulse
3D	3 dimensions

© COPYRIGHT UPM

CHAPTER 1

INTRODUCTION

1.1 Research background

Transformers are described as static electrical devices in power system networks used to transfer voltage/current of different levels through the concept of electromagnetic induction [1]. It is an important component in the electrical power system which plays a key role in maintaining the reliability and efficiency of the electricity supply. The topics related to condition monitoring of transformers have been vastly examined over the last few decades. It is important to reduce the possibility of transformer failures during in-service operations, which can lead to a significant financial loss.

Windings are the crucial components of a transformer and its reliability significantly impacts the transformer system. Winding faults could cause reduction of power transfer capability, lead to voltage instability and result in uneven power distribution across different regions of the grid. The overall reliability of the grid could be compromised and may lead to increased downtime, frequent disruptions and inability to meet electricity demand during peak periods, affecting industrial, commercial and residential consumers. In the worst case, it can cause cascade effects where a fault in one area can potentially impact the interconnected components in the grid and cause a broader disruption across the grid.

© COPYRIGHT UPM

According to CIGRE WG A2/C4.39, the manufacturers consider the issues of transient voltages can be adequately addressed by current impulse testing standards [2]. However, many unknown transformer failures are dielectric origin and can be related to the frequent transient phenomena [3], [4]. Even though transformers are designed to withstand the switching transients during operations, resonance behaviours still can occur [5], [6]. The induced voltage can be significantly higher than the normal operating voltage, which can lead to transient overvoltage in the transformers.

A survey by Hermann reveals that 49.4% of all recorded faults occur within the winding with deformations as one of the primary causes [7], [8]. Deformations of windings are mostly caused by the behaviour of high electromagnetic forces within the transformer. One of the contributing factors of high electromagnetic force is the recurrence of switching transients [3]. Lightning transient is particularly destructive and requires robust protection compared to switching transient. However, the high frequency of occurrence and cumulative impact of switching transients in transformers make it a significant concern for long-term stability and reliability. It can cause severe deviations in the electrical, thermal and mechanical parameters of the windings.

In recent years, the industry has aimed to improve the condition monitoring of transformers through formula approximations, design, analytical testing and software validations [9], [10]. These approaches are proposed to reduce operational costs and at the same time to provide a reliable and effective non-destructive analysis. The use of FEM has emerged as effective and is

© COPYRIGHT UPM

suggested as one of the best cost-efficient alternative methods to obtain data as well as solve engineering problems [11], [12]. It can simulate complex physical phenomena in transformers and provide findings that are quite close to the actual conditions [13], [14]. The transient analysis through FEM involves solving the mathematical equations that describe the dynamic behaviour of the transformer during the transient events. It implements the time-dependent nature of the transients, whereby it can capture the evolution of variables over time.

1.2 Problem Statement

Switching transients occur more frequently in power systems because of its inherent part of routine switching operations during the normal and abnormal conditions of power systems and equipment. Switching transients have a lower magnitude with fast rise times that cause rapid and high-frequency voltage changes in power systems. The transformer industry has adopted various condition monitoring techniques, including dissolved gas analysis (DGA), frequency response analysis (FRA) and partial discharge measurements to detect potential faults. However, none of these methods directly monitor electromagnetic force that can induce structural degradation, which is one of major contributors to transformer winding failures. Currently, no sensors are installed in transformers to assess switching transient’s effect to transformer winding, making predictive maintenance challenging. This limitation leads to a critical gap in understanding electromagnetic force due to switching transient's dynamic interactions and effects on transformer winding.

© COPYRIGHT UPM

General transient modelling guidelines for transformers are discussed in previous literature but do not cover all the modelling aspects. The determination of related parameters for specific transient models remains a complex task. It is inevitable for some reasons which include the complicated winding structure, practical limitations of construction as well as the complex relationship between its components. Previous studies acknowledge the integrated impact of switching transients on transformer winding electrically, thermally and mechanically. Despite this knowledge, there is a noticeable gap in the literature that fully accounts for the interactions between electrical, thermal and mechanical responses within transformer windings. This lack of comprehensive modelling leaves manufacturers without a precise framework to optimise transformer designs and insulation systems against switching transient effects.

Frequent switching transients in power systems generate high electromagnetic forces and thermal stress in transformer windings that lead to structural deformations. These mechanical effects are critical for ensuring transformer reliability, yet current industry practices lack real-time monitoring and predictive assessment tools to evaluate its long-term impact. As a result, manufacturers and utilities face challenges in preventing failures and improving transformer designs to withstand transient-induced stresses. Despite the known risks, limited research has been conducted to quantify the mechanical response and structural stability of disc windings under recurring switching transients. Existing studies often analyse electrical effects without

© COPYRIGHT UPM

fully capture the interdependent mechanical behaviours that affect transformer integrity. Additionally, winding material properties and structural responses vary under different conditions, making it difficult to develop a generalised interpretation of structural behaviour.

1.3 Objective of study

This study aims to investigate the impact of switching transients on a disc-type transformer winding through the FEM. To achieve the above aim, several objectives have been established.

1. To examine the impact of the switching transients on the electromagnetic force behaviours in a disc-type winding based on the analytical and numerical method through mathematical formulation and FEM.
2. To evaluate the dynamic interrelated response of electrical, thermal and structural response in a disc winding due to switching transient through the three-ways coupling of electric-thermal-structural transient analyses via FEM.
3. To quantify mechanical response and structural stability of a disc winding due to the electromagnetic force and thermal stress that results from the recurrence of switching transients.

1.4 Scope of study

The scope of this study will be limited as follows:

© COPYRIGHT UPM

i. The study presents a case of 1-phase HV winding of a 30 MVA, 33/11 kV disc-type distribution transformer. The physical geometry of a disc winding is simulated through Ansys Maxwell and Ansys Workbench.

ii. The study is based on the 3D model of 8 discs from 96 discs winding. Each of the discs consists of 6 conductors and 5 turns. This proportional modelling is made with the assumption that the winding behaviours are homogenous, where the simulation based on 8 discs can capture the essential transient characteristics of the winding.

iii. The analysis involves standard switching impulse (SSI) and non-standard switching impulse (NSSI) voltage waveforms. SSI voltage waveform refers to the specific impulse waveforms of 250/2500 µs as defined by IEC 60060. NSSI voltage waveform is based on its real-world occurrence during the energisation of a transmission line in the actual field. This study focuses on this NSSI due to its high occurrence in power system operations and field measurement data availability which has been recorded in actual field conditions making it suitable for reference and comparative analysis in this study.

iv. The force in each disc layer is computed from the analytical method via the winding design formulation. Meanwhile, the forces along the disc winding are computed from the numerical method through FEM in Ansys Maxwell.

v. The three-way coupling analysis includes electrical, thermal and mechanical analysis.

© COPYRIGHT UPM

- The electrical response is investigated through the Ansys Maxwell via electric transient analysis. The analysis computes the electromagnetic force and ohmic losses generated in the winding.
- The generated thermal behaviour is investigated through the Ansys Workbench via transient thermal analysis. The output analysis includes total heat flux, thermal gradient and thermal stress in the winding.
- The mechanical behaviour analysis is investigated through the Ansys Workbench via transient structural analysis. The analysis includes total deformation, directional deformation, equivalent elastic strain and stress.

1.5 Contribution of research

The present study attempts to address multiple gaps and to make important contributions as follows:

Technical

i. The study contributes to the interpretation of switching transient effects on the electromagnetic force behaviours within the disc winding by employing analytical and numerical methods. The study also contributes to introducing a progressive transient model that goes beyond conventional approaches by simultaneously considers electrical, thermal and structural aspects. This electric-thermal-structural coupled model enables a practical representation of the complex interactions within the disc winding during switching transient. This model can be further

© COPYRIGHT UPM

exploited to simulate disc winding behaviours under different operating conditions. This finding can lead to new insight into transformer behaviours and help to identify potential issues regarding the conditions.

ii. Industry practitioners can identify potential issues such as the likelihood of winding hot spots, displacement and deformation through the electromagnetic force and electric-thermal-structural coupled studies due to switching transients. The findings provide valuable insights for transformer designers and manufacturers to design the corresponding control strategies and enhance the reliability of disc-type transformers under the switching transient. These strategies may include the optimization of insulation materials and placement to reduce localised heating. The enhancement of mechanical reinforcement of windings helps minimize displacement and deformation. Additionally, damping and shock absorption methods can be introduced to counteract transient forces and vibrations. Winding configuration adjustments involve modifying the arrangement of transformer windings or conductor spacing to ensure a more uniform distribution of electrical and thermal stress. These changes may help to reduce localised overheating, dielectric stress and mechanical deformation.

1.6 Thesis outline

This written thesis consists of five chapters. Chapter 1 of this thesis includes the research background, problem statements, objectives and scopes of this research study. This chapter starts by highlighting the significance of

© COPYRIGHT UPM

transformers and introduces the challenges posed by transformers during switching transient. The problem statements emphasize the gaps in current understanding. The expected research contributions are clearly outlined at the end of this chapter.

Chapter 2 provides a comprehensive review of relevant literature. It begins with exploration the structure of transformers, highlighting the importance of windings. Followed by an analysis of transients in power system networks focusing on switching transients. This chapter includes the evolution of analytical and numerical methods for transient analysis, highlighting the FEM. The previous approaches to coupling analysis for transformer analyses are emphasised. The chapter concludes with the previous study on the transformer winding stability assessment methods.

Chapter 3 of this thesis focuses on the methodologies to achieve the objective of studies. A clear roadmap to achieve the 3 research objectives of the study is provided. The research design that includes the concept and methodology approaches of each objective is elaborated. The procedures to obtain electromagnetic force distributions based on analytical and numerical methods are presented. Followed by the methods for the transient coupling model development. At the end of this chapter, the methodologies to obtain the structural buckling behaviours and reliability of a disc winding due to electromagnetic force and thermal effect are clearly outlined.

© COPYRIGHT UPM

Chapter 4 addresses the results analyses and discussions of research findings. The results, followed by discussions interpreting the findings in relation to the 3 research objectives are reported. Firstly, the comparison of electromagnetic force based on analytical and numerical methods is presented. Then, the output parameters from the three-way coupling of electric-thermal-structural analysis are presented. Finally, the results of the structural buckling on the disc winding response to the electromagnetic force and thermal effect under switching transients are evaluated.

The final chapter of this thesis summarises the main findings and conclusions from this study. The recommendations for future works highlight potential paths for further research and the practical implications of the study in the power industry are presented.

© COPYRIGHT UPM

CHAPTER 2

LITERATURE REVIEW

2.1 Introduction

This chapter discusses the electrical, thermal and structural behaviour studies of a disc-type power transformer in switching transient. The transformer winding configurations and current issues on switching transient condition monitoring of the winding are presented. The characteristics of transient power systems are also discussed. Then, the impacts of switching transient on the transformer winding based on electrical, thermal and mechanical aspects are reviewed. The switching transient analysis of transformer winding through Finite Element Modelling (FEM) is studied. Lastly, the winding reliability assessment through FEM and gaps in the current transient issues are examined.

2.2 Structure of transformer

The transformer operates based on the induction principle with alternating current (AC) supply in the power system network. The insulated winding operating at different voltages is built closely around the magnetic core circuit to minimise stray magnetic fields and ensure maximum efficient energy transfer. The whole assembly is located within a metallic tank, which provides a contained insulating environment to the transformer. The winding ends

© COPYRIGHT UPM

connect the nodes of the external circuit through bushings. The transformer components are divided into 2 main parts which are the active and passive parts. The core and winding are known as the active part. Meanwhile, the passive parts are the tank, tap changer, cooling system and bushings as shown in Figure.2.1

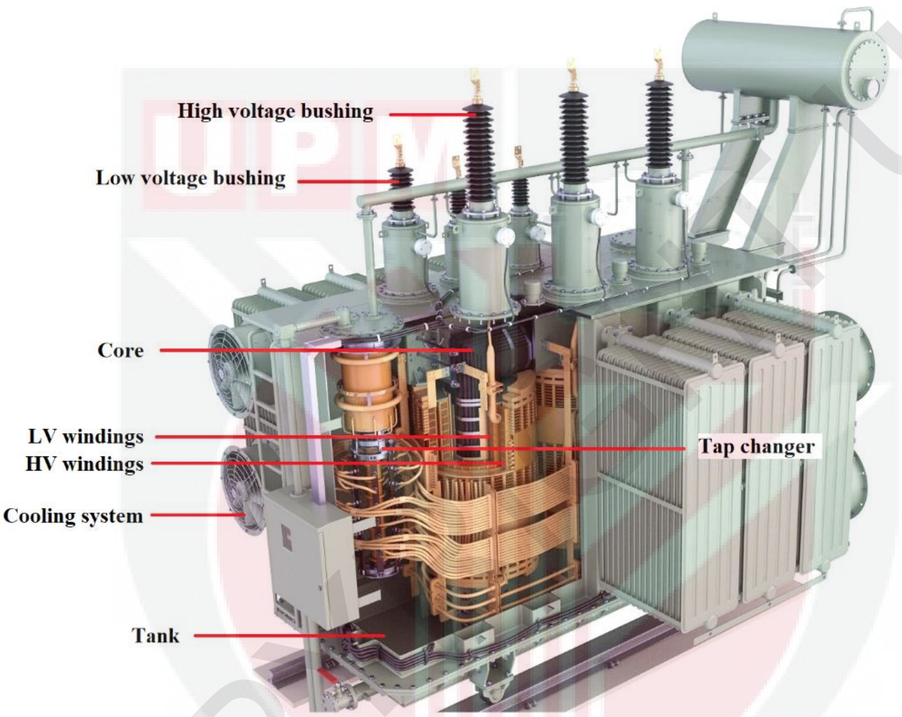

Figure 2.1: Components of a transformer [15]

The transformer experiences losses during operation, which can be classified as no-load and load losses [16]. No load losses also known as the excitation losses, originate from either the core or iron losses which are due to circulating eddy current in the core and magnetic hysteresis. The load losses are mainly due to copper and stray losses. Copper losses also known as ohmic losses, occur in the winding due to conductor resistance and are equal to I^2R. Stray losses are mainly caused by leakage flux in the windings and tank. Stray

© COPYRIGHT UPM

losses are determined through subtraction of the I^2R losses calculated from the measured resistance and load losses.

2.2.1 Winding of transformers

Windings are known as the heart of a transformer since they are the main electrical circuits that determine the voltage/current transformation capability [17]. The winding configuration can be used to determine the types of transformers [18]. Each of the winding configurations should be able to withstand normal and transient overvoltages. The type of winding is usually selected based on the apparent power rating and its applications. The most widely assembled windings are the layer- and disc- wound types.

The layer-type winding is an axially wound winding as shown in Figure 2.2 (a). The rated voltage for layer-type winding is distributed along the width of the winding. It is mostly used in the low voltage (LV) winding whereby it can carry large currents due to the large cooling surface of each conductor [18]. It is usually built with electrostatic shields between each of the layers to enhance the impulse voltage withstand capability [19]. The disc-type winding is a radially wound winding as shown in Figure 2.2 (b). The rated voltage for disc-type winding is distributed along the height of the winding. Disc-type winding is easy to construct due to the straight discs and it can be applied to either HV or LV winding. The distance between each of the discs creates radial duct that allows oil flow for cooling purposes [20]. Continuous disc-type winding is the

© COPYRIGHT UPM

most common design used in transformers due to its robust design and suitability for different types of power ratings [18].

The disc-type winding is better than layer-type winding in terms of voltage distribution or insulation as the rate of voltage increases. Layer-type winding is quite common for LV sections but it lacks the capability to withstand impulse voltages and short circuits. It is also used in some of the HV sections whereby it can reduce the overall voltage stress between the insulated layers. The application of disc-type winding for high-temperature superconducting transformers requires electrical bonding between the discs, which can lead to high losses [21].

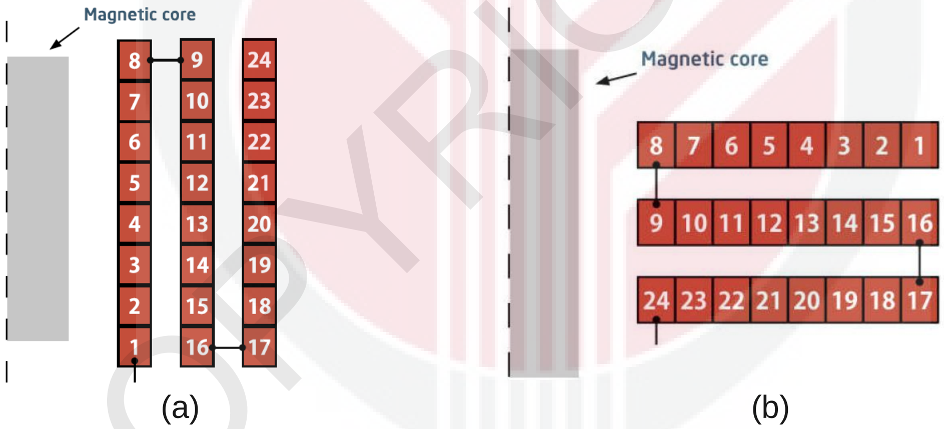

Figure 2.2: Commonly assembled winding structure; (a) Layer and (b) disc winding [18].

The winding should be properly insulated, supported and within acceptable temperature ranges. Rectangular conductor is commonly used because of its ability to provide maximum utilization of windings. Copper is the preferred conductor material due to its high conductivity and mechanical strength but in some cases, aluminium is used [22]. Aluminium is lighter and cheaper than copper but it has 50% lower conductivity than copper. The material used to insulate the winding is either varnish or insulation paper made from cellulose. The fibre in the cellulose is made up of long polymer chains, which provides elasticity to the insulation paper [23].

2.3 Transients in the power system network

Transient is defined as a very short duration of rapid increase of system voltage within a power system. It can be classified into external and internal overvoltages [3]. The most common and severe external transient overvoltage is the lightning surge. Internal transient overvoltage originates from the electromagnetic interactions within the electrical circuits. The most common internal transient overvoltages are switching and temporary surges. These overvoltages are characterised based on the wave shapes and its amplitude is dependent on the operation voltage of the power system network.

2.3.1 Mechanism of switching transient

The energisation or de-energisation of transmission lines, cables, capacitive, inductive and reactive loads like large capacitor banks, motors and transformers lead to sudden interruptions in power flows [24]. These interruptions result in rapid changes in magnetic and electric fields that can lead to transient overvoltage. During short circuit conditions, the power system initiates rapid and substantial changes in current and voltage. The protective

© COPYRIGHT UPM

devices response to the faults can create switching events, which can lead to the switching transient effects.

In general, the highest switching overvoltage in a high voltage network is caused by energizing and re-energizing of unloaded line [25]. When the line is connected to the source, travelling wave will start to travel along the line towards the receiving end and double there at the open end with an overvoltage near 3.3 p.u. This overvoltage may become significant because arrester operating voltages are relatively close to normal system voltage and lines are usually long, so the energy stored on the lines may be large. When these waves encounter a connected transformer, part of the wave is transmitted into the transformer and will put the transformer into saturation, causing core heating and copious harmonic current generation.

The making and breaking of the electrical network can result in abnormal voltage oscillation. High resonance overvoltage can occur in a transformer once the oscillation of the switching operation matches the resonance of the transformer [26]. This condition can occur once the frequency of switching transient voltage is close to the frequency of the transformer [27]. A typical power system network of the switching phenomenon with a connected transformer is illustrated in Figure 2.3.

© COPYRIGHT UPM

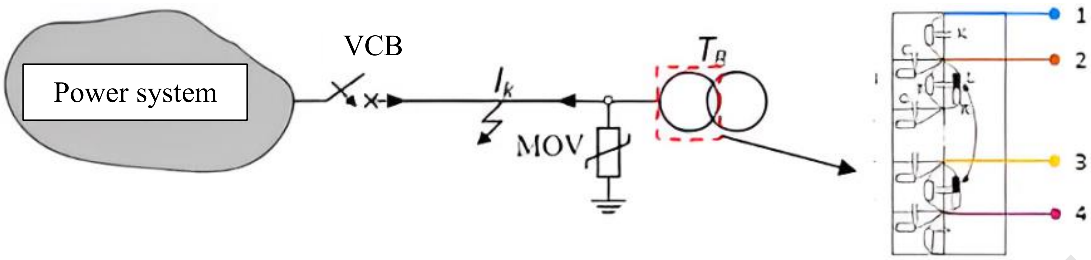

Figure 2.3: Switching transient event in a power system connected to a transformer [28]**.**

The switching transient from other parts propagates along the line through the travelling waves in the form of voltage and current. It can continue to propagate into the transformer windings through electromagnetic induction [26]. The primary winding is connected to the circuit where the switching event occurs. Once it propagates into the primary winding, it leads to a rapid change in the magnetic field of the winding. The transient induces voltage build-up across the primary windings. According to [29], the magnitude of the switching transient can be up to 3.5 times the nominal power frequency voltage. Earlier studies found that switching transient overvoltage can be as high as 5 times the normal power frequency voltage [30].

Switching transient is attributed to the combination of 2 factors in motor applications, the mechanical energy stored in a rotating machine and the electrical energy stored in an inductive load [31]. These transients are short-lived and oscillatory in nature. The inductive loads are most sensitive to an abrupt circuit change as a sudden current chop can induce voltage transients within the loads. Figure 2.4 illustrates that the current lags the voltage in an inductive load. Current chop before the current zero-crossing causes voltage spikes that lead to a severe transient overvoltage. As the current decreases,

© COPYRIGHT UPM

the voltage increases to its peak. The combination of induced transient voltage with the system line voltage results in a high voltage across the contact gap and causes abnormal stresses within the inductive load. In the case of transformers, it could trigger relatively large voltage stresses in the windings [32]

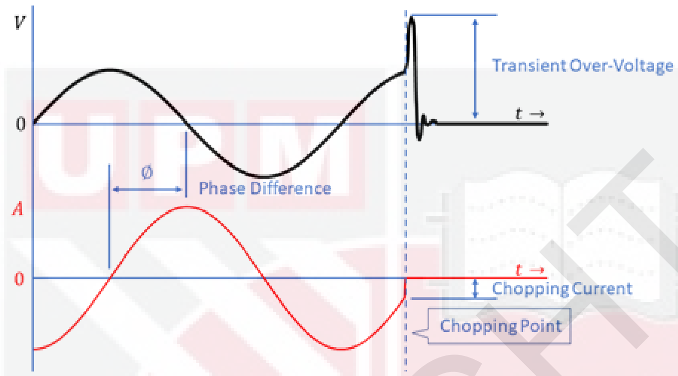

Figure 2.4: The current lags the voltage in an inductive load [31].

The Standard Switching Impulse (SSI) level is determined by the transformer operating level with a duration of a time to peak, T_p of 250 μs and a time to half value, T_2 of 2500 μs, 250/2500 μs as per IEEE Std C57.98 [33]. The tolerances that can be allowed in the front and tail times are ± 30% and ± 20%. The SSI waveforms can be seen in Figure 2.5.

© COPYRIGHT UPM

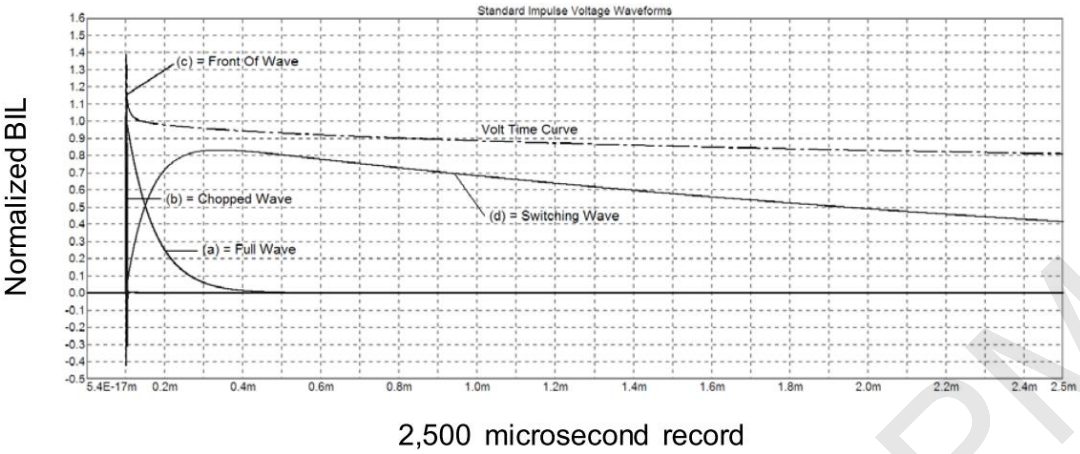

Figure 2.5: The standard switching impulse waveforms [33]**.**

The voltage distribution curves can describe the behaviour of the impulse propagation at different periods of time. It can be classified into 3 significant periods [34]. At the beginning of the phenomenon or wavefront, the capacitances of the circuit are the predominant elements that produce a non-uniform voltage distribution. At the end of the phenomenon or wave tail, the resistances govern the response of the circuit, which results in a uniform potential distribution. Between the periods described in wavefront and tail, the interaction of the electrical and magnetic energies that are stored in the capacitances and inductances of the circuit is developed. This interaction increases the oscillatory period whereby overvoltages can be obtained at different points along the winding.

Literature survey showed that there is no standard guidance on how to determine T_p for non-standard impulses. In IEC 60060-1, it is stated that for non-standard impulses, T_p can be determined by various methods of digital curve fitting depending on the actual shape. Another method is to directly capture transient overvoltages from high voltage equipment. Modify a standard

© COPYRIGHT UPM

impulse generator circuit by adjusting RLC components to replicate the observed and new non-standard waveforms [35]. Using software like MATLAB or EMTP to model transient responses in power systems [36].

The transient overvoltages can be obtained based on the mathematical modelling of a system using digital computers and scale modelling using transient network analysers. Field test measurements were conducted to obtain the amplitudes, waveforms and durations of the transient overvoltages at different points on the line. The recorded transient overvoltages on the power system network are useful for the design purposes of transformers [25].

2.3.2 Impact of switching transients on transformer windings

Transformers are designed to withstand and interrupt the high frequency transients during operation. Various protective measures are employed to mitigate the impact of the high frequency transients such as the use of surge arresters [37], snubber circuits [38], shields [19] and filters [39]. Surge arresters are the common protective method used but it only sensitive to voltage amplitudes and do not filter high frequency oscillations [6]. The incoming transient wave might still cause resonance behaviours in the winding even when the amplitude is well below the protection level when the frequencies are matched [5], [40], [41].

Another practice protective element is the RC filter with a large phase to ground capacitance [42]. This type of solution is characterised by its large size

© COPYRIGHT UPM

and cost which typically limits its applicability. Apart from the RC filter, synchronized switching can be used to provide mitigation against overvoltages [42]. This solution however requires significant modification of circuit breakers and results in a high cost of implementation. It is assumed that transformers are properly designed and protected against the abnormal voltages that arise during its operations. However, many unknown failures are related to transient phenomena [3], [4].

During normal power frequency excitation, the voltage distribution along the winding is nearly linear and is governed by the turn ratio and resistive losses along the length of the winding [43]. This condition is the typical inductive behaviour of a winding during low frequency excitation. If the excitation waves contain high frequency components, the capacitive nature of the transformer winding structure becomes apparent [44]. The presence of these capacitances along with the inductive properties of the transformer winding forms an electromagnetic system of high order. This system is capable of resonating at various excitation frequencies, which leads to voltage amplification at different parts of the transformer winding structures [45]. The linearity of the voltage distributions can also be affected [33].

The rapid change in voltage can expose the transformer winding to a high voltage stress. This voltage stress can lead to insulation breakdowns and electrical faults. The oscillations along the winding cause abnormal electromagnetic stresses not only to the turn-to-turn but also in section-to-section insulation and the conductor itself. These conditions induce

© COPYRIGHT UPM

mechanical stresses on the winding structure. The mechanical stresses are caused by 2 main modes of force subjected to the winding, which are axial, F_a and radial, F_r forces as illustrated in Figure 2.6.

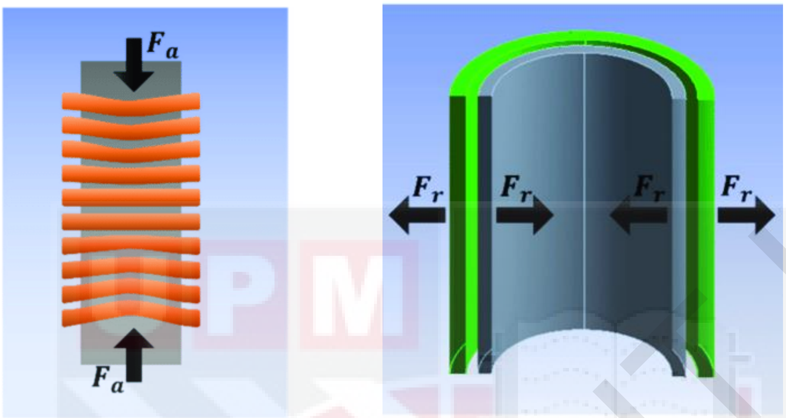

Figure 2.6: (a) Axial and (b) radial behaviour of force on transformer winding [46]**.**

These forces cause mechanical faults in the winding. It can be divided into 2 main modes, which are axial displacement and radial deformation [47]–[51]. Axial displacement occurs due to axial forces being generated in parallel to the winding height [52]. Due to the pattern of axial forces, windings will experience opposing forces. This condition may generate compressive forces and lead to displacement, titling and bending of windings. The radial force acts parallel to the axis of the transformer winding. The radial force can cause hoop tension, forced and free buckling. When both forces are excessive, it can cause spiralling and telescoping of windings. Figure 2.7 shows a few cases of radial deformation and axial displacement of transformer winding.

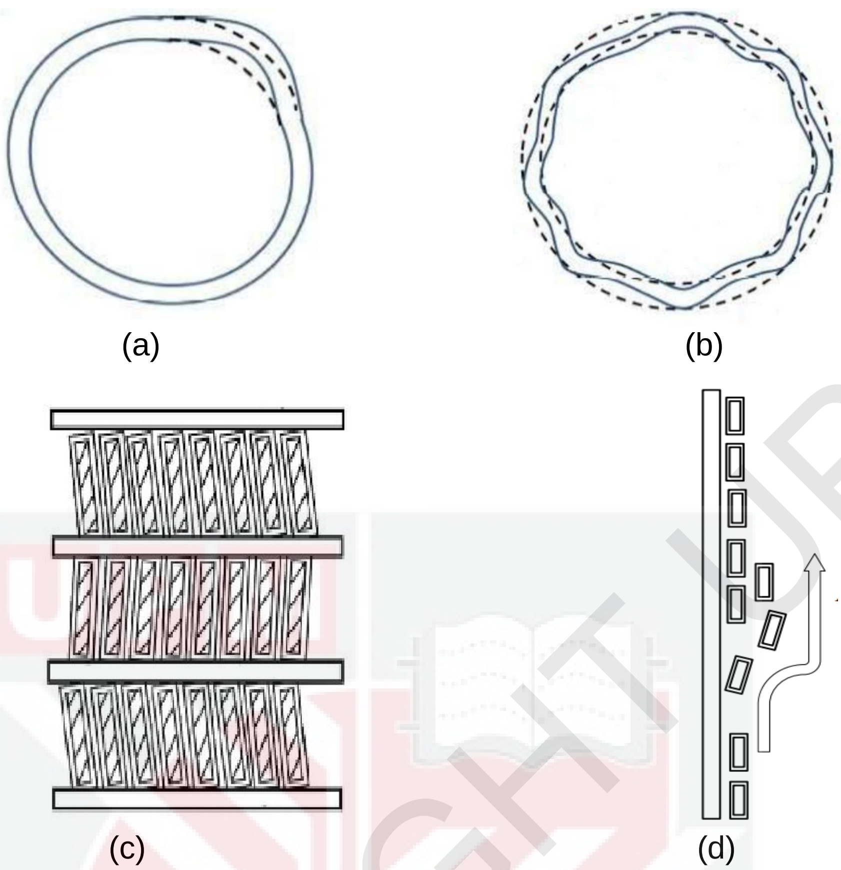

Figure 2.7: (a) Free buckling, (b) force buckling, (c) tilting and (d) telescoping of transformer winding [26], [53], [54]**.**

Apart from electrical and mechanical indicators, thermal is one of the fundamental parameters that provide valuable information about potential abnormalities in transformers. A previous study by Blume and Boyajian shows that the current from the transient voltage excitation causes energy dissipation [44]. This dissipation represents the losses that can be observed in copper conductors, cores and dielectrics. It is found that during overvoltage with high frequencies, losses are higher in the copper conductors than in the core and dielectric.

In steady-state conditions, the conductor heat gain is equal to the heat loss meaning that no heat energy is stored in the conductor [55]. During transient

© COPYRIGHT UPM

conditions, internal heating in winding may occur due to the increased ohmic losses caused by rapid changes in transient current flow through the winding. Rapid changes in magnetic flux during transient induce high frequency eddy current in the core, which results in a significant heating effect.

Skin effect occurs as a result of the high number of electrons travel to the outer circumference of the conductor caused by the high frequency. This condition causes the effective cross-sectional area of current flow to reduce and increase copper losses. These losses associated with the eddy current that is induced during switching transient contribute to localised heating in the transformer winding. The uneven distribution of currents and the concentration of energy in specific regions can create hot spots within the winding. This condition can accelerate ageing processes, degrade insulation and increase the risk of thermal breakdown.

2.4 Switching transient analysis

Throughout the years, several methods have been implemented for the switching transient analyses in transformers. From traditional testing techniques to advanced numerical simulations, each of the methods offers significant insights into the behaviours of transformers during switching transient. The established methods satisfy important criteria like sensitivity towards important parameters of the transformer conditions and provide results that closely match the real behaviour of the transformer during switching transient.

© COPYRIGHT UPM

2.4.1 Switching transient analysis through analytical methods

As the operating voltage of transmission systems increases, switching surge overvoltage determines the insulation design rather than lightning overvoltage [56], [57]. The switching impulse voltage withstands test is one of the acceptance tests carried out for transformers before put in service [2]. During the test, the transformer winding is connected to a high-voltage switching impulse generator. As the switching impulse voltage is applied across the winding terminals, the transformer responses to the transient voltage are monitored.

The observed responses include visible signs of insulation breakdown, such as corona discharge or flashover. The insulation resistance and capacitance are measured before and after the tests to assess any changes resulting from the switching impulse voltage. The switching impulse test is conducted in accordance with international standards such as the IEEE Std 339-1972, IEEE Std C57.98-2011 and IEC 60076. These standards specify the test procedure, test parameters and acceptance criteria for the switching impulse test. The factory acceptance test offers direct validation of the system's transient response under realistic conditions and confidence in its performance. However, the test can be expensive, time-consuming and requires specialised equipment and expertise.

The Laplace Transform method is a mathematical technique that is commonly used to analyse the transient response of linear time-invariant systems, including switching transient in transformers [30], [31]. This method involves the transformation of complex differential equations that govern the transformer behaviours into Laplace domains known as algebraic equations. These equations typically include Kirchhoff's voltage law, current-voltage relationships and transformers equivalent mathematical models.

The transient response typically includes voltage and current transfer functions, impedance characteristics and frequency of the system [58], [59]. Once the transient response in the Laplace domain is obtained, it is inversed back into the time domain. The transient response provides insights into transient response time, oscillations, damping, steady-state behaviour, transient recovery, voltage and current peaks and the effect on impedance parameters. However, Laplace transform analysis often involves simplifications and assumptions about the circuit behaviour, which might be imprecise to capture the complexity of real system conditions. The computations of differential equations from the Laplace transform analysis can be computationally intensive and time-consuming for a complex system of switching transient in a transformer.

Transient field measurement is another analytical method that can be used to analyse switching transients in transformers [31]. Field measurements typically focus on 3 categories, transient generated by switching operations, regular commutation and external operations. The external operations include lightning strikes, inception and interruption of faults. Specific equipment required for the transient measurement includes oscilloscopes, spectrum

© COPYRIGHT UPM

analysers, transient recorders, electromagnetic field probes, antennas or specialised sensors to capture the transient.

Since electrical transients are often unpredictable, continuous monitoring of circuits is necessary to detect and record the disturbances. Computer-based instruments facilitate digital capture and retrieval of transient data for further analysis. This method provides direct observations of the transient phenomena in real environments and insights into the transient behaviour of transformers under in-service operating conditions [60], [61]. External factors such as electromagnetic interference (EMI), noises and environmental conditions can affect the accuracy and reliability of this method.

2.4.2 Switching transient analysis through numerical methods

The Electromagnetic Transient Program (EMTP) or a similar concept method, Alternative Transient Program (ATP) is a numerical simulation tool used to analyse transient phenomena in electrical systems, including switching transient in transformers. These methods simulate the transient behaviours using circuit-based models [62]–[64]. It involves solving complex differential and algebraic electrical circuit equations to predict transient responses. A detailed model of the transformer is created and incorporated into the power system circuit model. This includes connecting the transformer to other components such as transmission lines, switches, circuit breakers and loads. The configuration should accurately represent the actual topology of the power system.

© COPYRIGHT UPM

Several parameters are analysed to understand the transient behaviour of a transformer such as voltage spikes, current surges or oscillations. The stresses on transformer windings and insulation can be obtained based on peak voltage and current. The EMTP/ATPs software allows for detailed simulation of transient behaviours in the electrical systems and offers a wide range of modelling options for various phenomena. The accuracy of simulation results depends on the accuracy of the models used to represent the system components and phenomena.

Another numerical method is the FEM which is found as one of the best non-intrusive methods used to simulate and analyse the behaviours of transformers under various operating conditions, including switching transient [13], [14]. It can analyse different phenomena such as the electromagnetic, thermal, structural, fluid, acoustic and vibration within a transformer. The simulation methods mainly utilise empirical formulas, circuit models and numerical calculations [43], [65]. The calculation is fundamentally based on the integral or differential forms of Maxwell's equations [58].

The usability of FEM was first demonstrated by O. C. Zienkiewicz in the late 1960s and was quickly extended to many application fields in the 1970s. The FEM was first used for transient studies by Abetti [66]. The model consisted of an equivalent circuit representing discrete subdivisions of the transformer winding. Each of the divisions had its particular self-inductance, mutual inductance to all other sections and capacitive coupling to adjacent sections

© COPYRIGHT UPM

and earth. It was discovered that not every characteristic of the transformer is affected by transient phenomena.

2.4.2.1 Transient modelling through FEM

The IEEE working groups produce standards for the modelling and analysis of system transients based on digital programs and present the guidelines for different types of studies [67]. IEEE 1597.1-2022 and 1597.2-2010 discuss the validation methods for computer modelling and simulations [68]. CIGRE WG 33-02 covers the importance of power components and proposes the representation for each component with consideration of the frequency ranges of the transient phenomena [69]. IEC 60071-4 provides the modelling guidelines for insulation coordination studies based on the numerical simulation [70]. The modelling guidelines on the consideration of transformer parameters based on transient frequency ranges are shown in Table 2.1.

Table 2.1: Modelling guidelines for transformers [34].

Parameter / Effect	Low frequency transients	Slow front transients	Fast front transients	Very fast front transients
Short circuit impedance	Very important	Very important	Important	Negligible
Saturation	Very important	Important	Negligible	Negligible
Iron losses	Important	Negligible	Negligible	Negligible
Eddy currents	Very important	Important	Negligible	Negligible
Capacitive coupling	Negligible	Important	Very important	Very important

© COPYRIGHT UPM

The simulation of a transient phenomenon implies that the selection of models and the selection of the system area must be represented. For low frequency and slow front transients within the ranges from 0.1 Hz to 3 kHz and from 50 Hz to 20 kHz, the model must incorporate saturation effects, as well as core and winding losses. For fast front and very fast front transients within the ranges from 10 kHz to 3 MHz and from 100 kHz to 50 MHz, the core losses and saturation can be neglected. In addition, the coupling between phases must be considered.

The effect of the iron core is neglected in various inductance models used for voltage transient studies [71], [72]. Once the winding structure is excited with high frequency impulse, the inability of current to change instantaneously through an inductor implies that a negligible amount of flux will be set up in the core during the initial response period [71]. Furthermore, the effective permeability of the core steel decreases at high frequencies [73]–[75]. Through consideration of these matters, most of the inductance models are assumed to be air-core. The flux is assumed to be radially unbounded at the top and bottom yokes where the core is considered an infinite permeability. Hence, no radial flux component from the core is considered. Several studies show acceptable results on the effect of neglected core at frequencies higher than 10 kHz [76]–[78].

Since limited data on the high frequency characteristics of insulating materials can be obtained, the high frequency modelling of the transformer focuses on constant permittivity without consideration of the dielectric losses. In addition,

© COPYRIGHT UPM

the impact of dielectric losses is less on the high frequency modelling of the transformer [26]. The primary requirement of high frequency transformer modelling is its ability to describe the inductive behaviour of winding structures as specified in [34]. The critical aspects that need to be considered are the modelling properties, initial conditions of the system, boundary conditions and the frequency ranges. Another consideration is that all the non-impulse winding terminals should be grounded.

For electric analysis, properties such as conductivity and permeability are crucial since it can affect the distributions of current and electric fields within the winding [79]. Additionally, the dielectric properties of insulation layers are important to assess the insulation integrity under transient conditions. In thermal analysis, properties like thermal conductivity, specific heat capacity and coefficient of thermal expansion are required to predict temperature distribution, heat transfer rates and thermal stresses within the winding [80]. These properties govern the response of winding material to changes in temperature, impacting its mechanical behaviours. For structural analysis, mechanical properties such as Young's modulus, Poisson's ratio and yield strength are essential. Young's modulus and Poisson's ratio determine the material's stiffness and deformation characteristics under applied loads, while yield strength defines its mechanical limits [81]. Figure 2.8 shows the yield stress of copper material by its stress-strain relationship graph.

© COPYRIGHT UPM

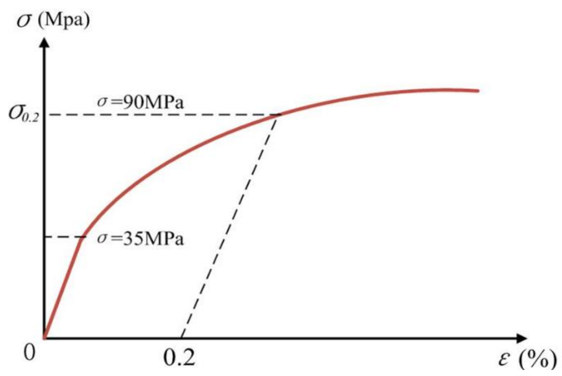

Figure 2.8: Mechanical properties of copper [81].

The plastic deformation model in the mechanical analysis of copper includes 3 essential parts which are yield, flow and hardening criteria. The yield criterion determines the stress level at which yielding begins, σ. Once the maximum stress value exceeds the yield stress level, $\sigma_{0.2}$, plastic deformation will occur. The flow criterion is characterized by its ability to undergo uniform deformation and strain hardening. The strain hardening results in an upward slope after the yield point, indicating an increase in strength with continued deformation.

In transformer modelling, the initial conditions must be set in accordance with the simulated parameters. In electric transient analysis, the initial condition can be the voltage and current values. In thermal analysis, it can be the initial temperature within the transformer. These initial conditions play a crucial role in determining how the transformer behaves and evolves under the switching transient conditions.

Boundary conditions in FEM are set to simulate the real-world interaction of the transformer with its external environment. Typically, voltage and current boundary conditions are applied to nodes or surfaces within the model for the

© COPYRIGHT UPM

electrical analysis [82], [83]. For magnetostatic simulations, the boundary conditions are usually defined by the behaviours of the vector potentials. The magnetic flux is either specified as tangential or perpendicular to the boundary condition.

Thermal boundary conditions are applied to nodes or surfaces to represent the initial thermal conditions or external temperature influences [84]. Heat flux boundary conditions are set to simulate the rate of heat transfer through certain surfaces per unit of time [85]. Convection or radiation boundary conditions provide the method for heat exchange with surroundings [86]. Convection is a heat transfer between a surface and surrounding fluid, gas or air. Radiation is a heat transfer emitted from a surface in the form of electromagnetic waves due to temperature of a surface.

For structural analysis, boundary conditions define the mechanical constraints and external forces that act on the system [87]. Displacement constraints are imposed on nodes or surfaces to represent fixed or constrained points that can simulate mechanical supports or constraints within the structure [88], [89]. Force or load conditions are applied to nodes to model external forces or loads that affect the system [90]. Symmetry boundary conditions can be employed to reduce the computational complexity and simulation time [91]. Suitable boundary conditions can capture the structural responses to external mechanical influences. Figure 2.9 shows 3 examples of applied boundary conditions used in this study.

© COPYRIGHT UPM

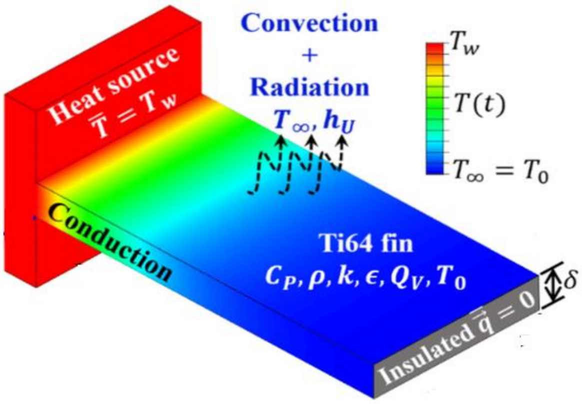

(a)

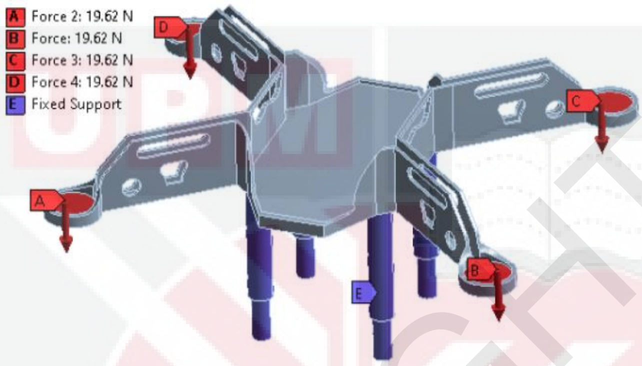

(b)

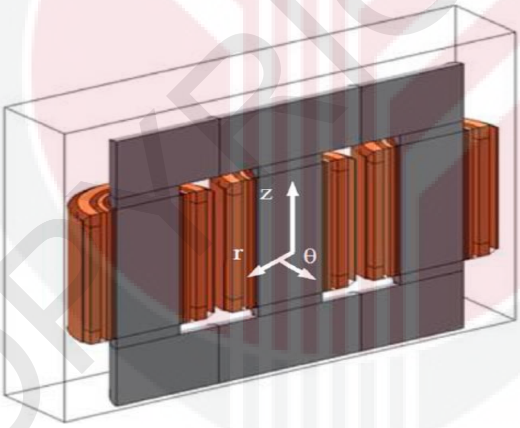

(c)

Figure 2.9: (a) Thermal, (b) structural and (c) symmetry boundary condition [92]–[94]**.**

For electric transient analysis, the loads involve the application of time-varying electrical conditions to simulate dynamic behaviours in electrical systems. The load could be voltages, currents, charges, volume charges and sinks. The electric transient analysis can analyse the voltage distribution, electromagnetic field distributions and power losses. For thermal analysis, the load can be temperatures, heat fluxes, heat flows and internal heat generations. The thermal analysis computes the temperature distributions and thermal stresses. The load for structural analysis can be forces, pressures, moments and thermal strains applied to the structural elements [95]. It could measure the stress and strain, deformations and displacements of a structure.

2.4.2.2 The computation of disc winding RLC parameters

The RLCG parameters of the HV disc winding were extracted through the quasi-state Ansys Q3D platform [96]. These parameters were used in the RLC equivalent circuit of the disc winding. The R refers to the series resistance of the winding conductor, R_s. The L comprises self and mutual inductances, L_s and L_m of the disc winding. The C comprises series capacitance, C_s and winding conductor to the ground capacitance, C_g. The G is made up of conductance parallel to the C_s, G_{cs} and conductance parallel to C_g and G_{cg}. The inductances and resistance were extracted through the Method of Moment (MoM). The self-inductance, L_s was computed based on Equation (2.1) [96].

$$L_s = \frac{0.002l\left[ln\left(\frac{2l}{w+h}\right)+0.5+0.2235\left(\frac{w+h}{l}\right)\right]}{10^6}H \qquad (2.1)$$

where l, h and w are the length, height and width of the winding conductor. The mutual inductance, L_m exists within 2 winding conductors whereby one of the conductors is considered as the source that reacts with the neighbouring conductors upon a time-varying magnetic field via quasi-magnetostatic

© COPYRIGHT UPM

interaction [97]. The impedance matrix was presented as $Z = R + j\omega L$. The magnitude of the L_m was computed by Equation (2.2) [98].

$$L_m = \frac{0.002l\left[ln\left(\frac{2l}{d}\right)-1+\left(\frac{d}{l}\right)\right]}{10^6}H \qquad (2.2)$$

where l is the length of the conductor and d is the space between the neighbouring conductors. Due to the consideration of skin and proximity effects, the R_s were in frequency-dependent and computed using Equation (2.3) [99].

$$R_s = \frac{l}{2\sigma\delta(h+w)}\ \Omega \qquad (2.3)$$

where l is the length of the conductor, σ is the conductor's conductivity and δ represents the conductor skin depth. The capacitance was established through MoM via quasi-electrostatic solver [96]. The C_s was measured based on Equation (2.4) [76].

$$C_s = \frac{2\pi\varepsilon_0\varepsilon_r h}{ln\left(\frac{d_i}{d_0}\right)}F \qquad (2.4)$$

where ε_0 and ε_r are the air and relative permittivities of the insulation paper between the conductor. h is the height of the winding, d_i and d_0 are the inner and outer radiuses of the conductor. The mutual capacitance, C_m or inter-disc capacitance was calculated based on Equation (2.5) [97].

$$C_m = \frac{27.6\times1\times\varepsilon_r}{10^{12}ln\left(\frac{d}{w}+\sqrt{1-\left(\frac{2w}{d}\right)^2}\right)}F \qquad (2.5)$$

© COPYRIGHT UPM

where *d* is the distance between each of the discs and *w* is the width of the conductor. ε_r is the relative permittivity of the insulation between each of the turns. The admittance matrix, [*Y*] = [*G*] + *jω*[*C*] which consisted of conductance [*G*] and capacitance [*C*] matrices was computed based on the quasi-electrostatic solver [100]. The Ansys Q3D parameter extractor computed the impedance into matrices form. The ground capacitance, C_g for a disc winding can be calculated based on the equation for capacitance between a disc and an infinite plane as Equation (2.6).

$$C_g = \frac{\varepsilon \times A}{d} \tag{2.6}$$

where *ε* is the permittivity of the surrounding medium, *A* is the effective area of disc winding facing the ground and *d* is the distance between winding and ground.

2.4.2.3 Model validation

According to IEEE 1597.1-2022, model validation can be performed by comparing the results of various computational models against a set of references, which includes benchmarks, standards and self-validations [101]. The 3 levels of model validations are mathematical, implementation and model level. The first level determines if the underlying computational technique is consistent with fundamental theory. The second level of validation is based on a specific software code implementation to verify the creation of simulation

© COPYRIGHT UPM

results within an acceptable tolerance. The specific model validation is by confirming that the model adequately represents the physical structure or system it intends to simulate and analyse.

For example, the simulation results in [46], [102] were compared with experimental data for validation of the methodology. Some compared simulated results to experimental results [50], [103], [104]. The validation of the 3-phase transformer model in [76] was carried out by comparing the calculated and simulated initial voltage distribution. Similarly, the validation [13], [78] is done by comparing simulated and calculated values of its parameters. The validation in [78] is performed by running a full factorial design of experiments where losses from the analytical model were compared to FEM as shown in Figure 2.10. Another validation of the model is health index validation as done in [105]. Numerical scoring and weighting techniques are applied for the condition diagnostic test results in the form of multi-criterion analysis to calculate the health index of the power transformer.

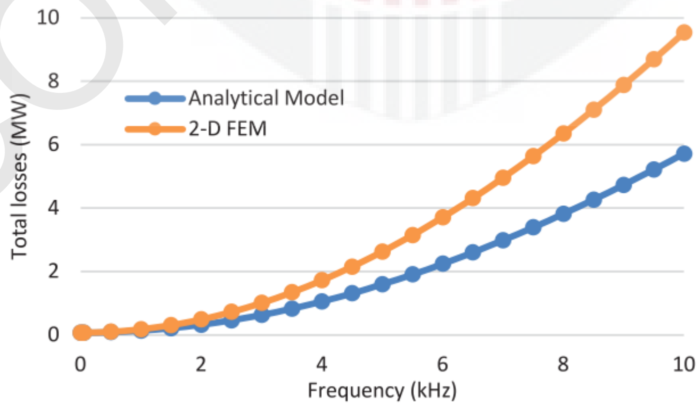

Figure 2.10: Total power losses comparison between analytical and FEM [78]**.**

2.4.2.4 Switching transient analysis through FEM

It is found that the FEM is capable to derive the transformer parameters without any physical verification [106]. The work shows the effectiveness of FEM to determine the parameters of transformers to analyse and detect the internal faults for both oil-cooled as well as dry-type transformers. One of the important analyses is the electromagnetic forces in the winding. According to Lorenz's law, the electromagnetic forces depend on the axial and radial leakage flux [107], [108]. The axial and radial forces arise from the interaction between the radial and axial leakage flux with current density passing through a conductor.

Several studies have been conducted to examine the magnetic fields, stresses and electromagnetic forces during transient conditions through the FEM. The electromagnetic forces on the transformer windings based on FEM are carried out in [109]–[112]. As shown in Figure 2.11, the axial and radial forces are found to be the highest at the end and middle sections of the windings, respectively. Studies on the stress concentration factors found that the irregularities in the stress distributions cause abnormal stress concentration on the winding [113], [114]. The magnetic fields within transformers of different geometrical dimensions and magnetic parameters are also examined in the previous study [115]. It has been discovered that different winding configurations can affect the distribution of magnetic field and electromagnetic force. The leakage flux induced by different types of faults can affect the structural deformation and displacement of the windings [116], [117].

© COPYRIGHT UPM

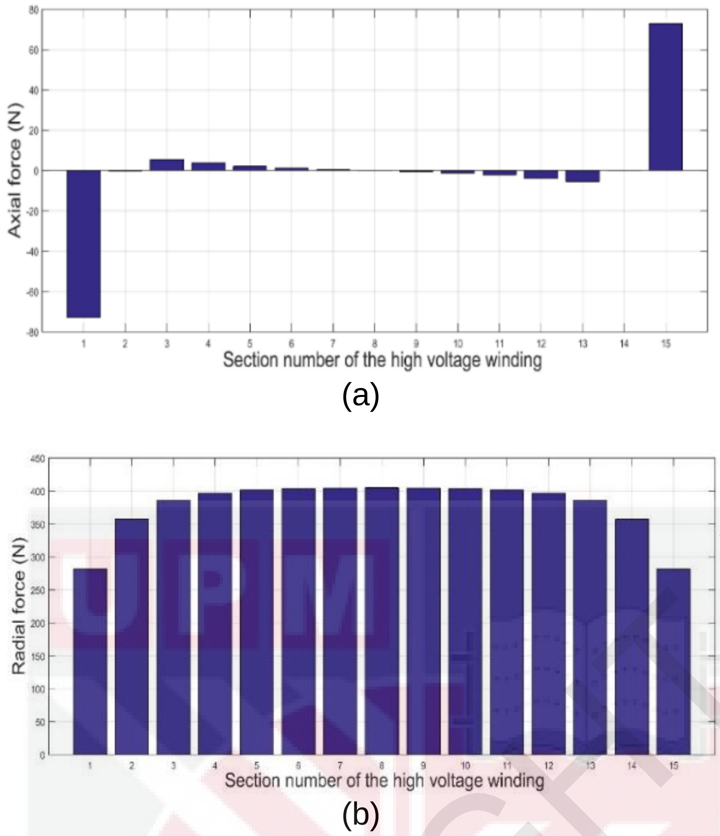

Figure 2.11: (a) Axial and (b) radial distributed force based on FEM [111]**.**

Another factor contributing to winding faults during switching transient is thermal stress. The transient overvoltages were found to increase the tendency of thermal stress in the windings since it creates undesirable additional losses and temperature rise [118]. It is difficult to predict and locate the hot spot in the transformer winding. One solution is to measure the temperature rise in transformer windings with distributed optical fibre sensors embedded along the windings [119]. However, it is costly, has issues with electromagnetic compatibility, and has limited application to large transformer ratings. The transformer temperature can be obtained intuitively through FEM through thermal analysis and the results obtained are close to the actual condition [102], [120], [121].

2.4.2.5 Coupling analysis through FEM

Due to complex phenomena within the transformers, coupling between several physical phenomena was suggested in [110], [122], [123] to obtain results closer to physical reality. Wang et al. [81] proposed the electromagnetic-structural coupling analysis using FEM and validated it through experimental measurements. The analysis computes the cumulative strain–stress characteristics of transformer windings under short circuit conditions. It was found that an initial and slight deformation in windings may influence the magnetic flux distribution. The flux distribution can increase the electromagnetic force in the windings. Similarly, papers [87], [124] coupled electromagnetic-structural analysis to investigate the electromagnetic forces, stresses, structural deformation and safety factors of transformer winding under inrush current and short circuit conditions.

The study highlighted the significance of considering the nonlinear behaviour of winding properties and identified critical areas prone to mechanical failures. The cumulative stress-strain characteristics of transformer windings were analysed based on electromagnetic-structural coupling analysis of a two-windings 110 kV transformer [81]. The results show that the material characteristics of a transformer winding and the state of tension determine the shape of the winding deformation, type and the extent of the deformations [46].

The coupling analysis continues to evolve by coupling more physical phenomena to study its interactions and relationships. The three-way coupling

© COPYRIGHT UPM

of magneto-fluid-thermal analysis was employed in [85], [125]. The analysis computes the temperature rise and hotspots of a simplified power transformer rated 2500 kVA and 180 MVA. The influence of the insulation barrier is considered to reshape the airflow path and radiative effect between the HV and LV windings. Another consideration is the oil changes, boundary changes and loss variation with temperature. This study provides insight into dynamic heat transfers and identifies optimal cooling strategies. Figure 2.12 shows that the velocity distribution of oil in the transformer influenced the temperature distribution of the core.

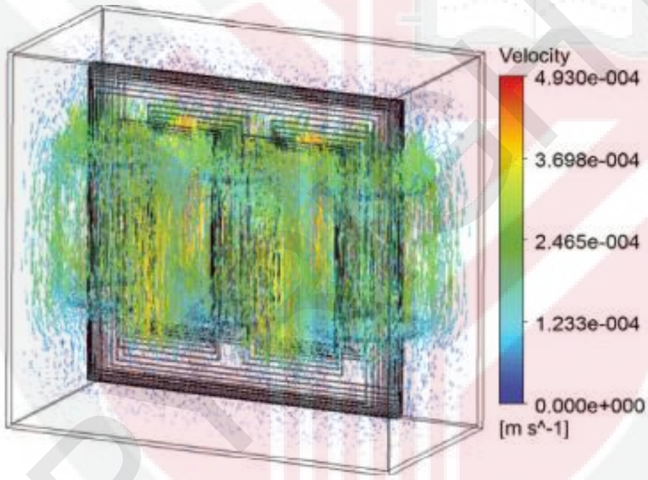

(a)

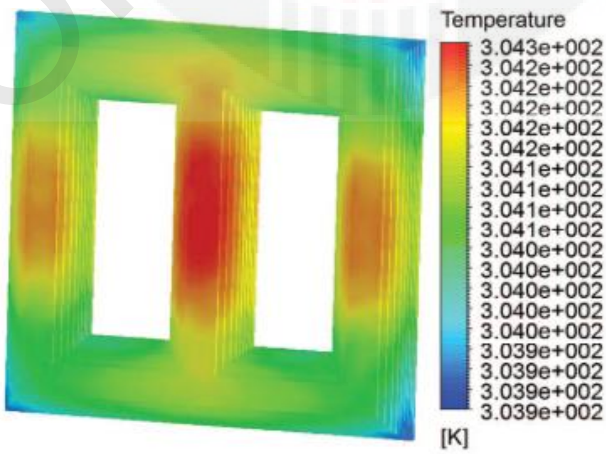

(b)

Figure 2.12: (a) Velocity distribution of oil in the transformer and (b) temperature distribution of core [85].

The relationship between temperature and yield strength, temperature rise and ultimate instability load of transformer windings was analysed in [126]. The analysis was based on the electromagnetic-thermal-structural coupling method with experimental validation. The results show that the temperature changes cause the plastic deformation to increase and reduce the yield strength of the winding. Similarly, reference [46] performs an analysis on a 50 MVA single-phase transformer based on electromagnetic-thermal-structural coupling in nominal, inrush and short circuit current conditions. The analysis shows that different operating conditions influence the performance and behaviour of transformer windings. Figure 2.13 shows the main physical phenomena involved in electromagnetic devices, including transformers.

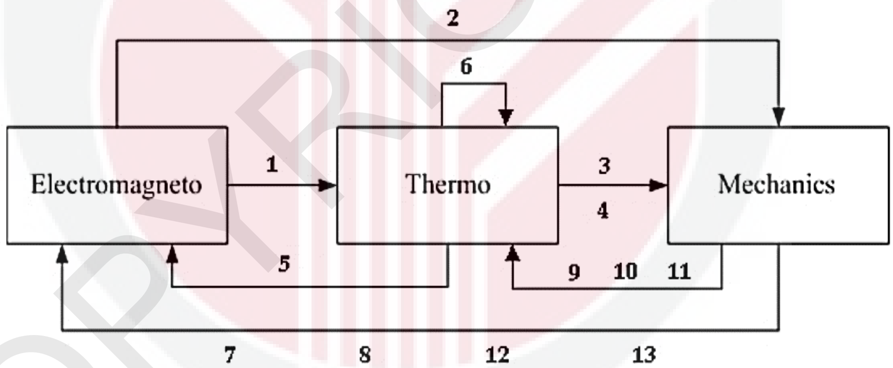

Figure 2.13: Main physical phenomena in electromagnetic devices [127]**.**

The arrows display the input and output parameters that show the relationships of coupled phenomena. The arrow labelled 1 is the Joule losses, 2 is electromagnetic forces and torque, 3 and 4 is the temperature distribution which alters the mechanical state of the structure dependence on thermal properties. Arrows 5 and 6 represent the electromagnetic and temperature based on the material's thermal properties. Arrow 7 is the new geometry of the

© COPYRIGHT UPM

structure that influences the distribution of the electromagnetic field. Arrows 8, 12 and 13 are the velocity of movement or deformations, contact electrical resistance and coercive force dependence on the state of mechanical stress. The 9, 10 and 11 are the heat generation due to mechanical deformations of material, heat generation due to friction and contact thermal resistance.

2.5 Transformer winding reliability assessment

The transformer reliability survey was formed in 2008 with the objectives to review existing surveys and study different practices [7]. The reliability of transformer winding can be diagnosed through the assessment and estimation of structures, elements and causes of the state conditions. Several works used integral transformer lifetime models [88], [128]–[130]. Another method that can assess the reliability of transformer windings is the winding resistance test [131]. The winding resistance test measures the resistance of the transformer windings to determine if there are any defects or connectivity issues.

The Fault Tree Analysis (FTA) is a visual representation of the direction of failure from the smallest component [132]. In FTA, the Boolean logic is used to review the undesired state of a system. The logic data includes using instructions such as "OR", "AND", "NOR", “EXCLUSIVE-OR” and “EXCLUSIVE-NOR” on low-level events. In most cases, FTA is used in reliability and safety engineering to help formulate a risk management plan or mitigate the effects of a science problem.

© COPYRIGHT UPM

The buckling strength analysis can be used for the reliability assessment of transformer windings. It is conducted based on empirical formulas and analytical methods [133]. These methods use equations based on historical data and observed trends to estimate the buckling strength of the transformer winding. Buckling strength analysis through FEM is a non-destructive reliability assessment method [133]. The structural integrity of transformer windings is modelled and analysed by determining their ability to resist buckling. Figure 2.14 shows an example of a load-displacement curve obtained from a buckling strength analysis. It shows that as the temperature and plastic deformation of the winding increase, the buckling strength is reduced.

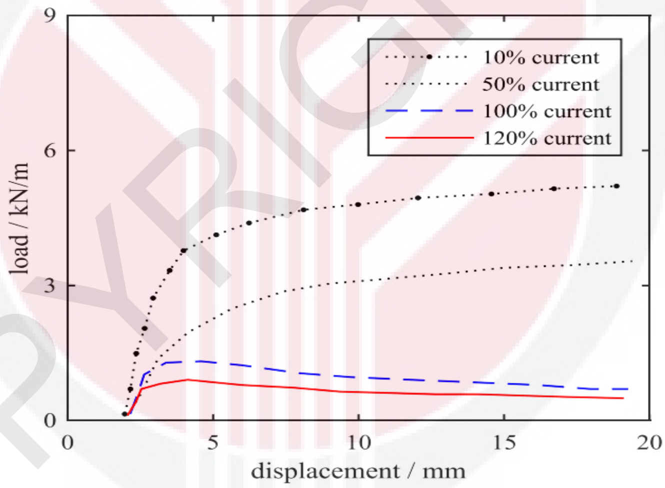

Figure 2.14: Load-displacement curve of a transformer winding [126].

Buckling is a form of structural failure where a structure is subjected to compressive loads and becomes unstable, resulting in deformation or collapse. This condition happens when the structure is compressed beyond its elastic limit. The buckling strength of transformer windings can be affected by the material properties of the winding, winding geometry, dimensions and level of loading applied to the winding [126]. The analysis involves calculating the compressive load the winding structure can withstand and analysing the physical properties of the winding structure. The physical properties may include winding dimensions, material properties and load distribution within the winding structure.

Buckling strength analysis involves breaking down the winding into a large number of small elements and solve the equations to compute the behaviour of the winding under applied loads and boundary conditions [134]–[136]. Through simulation of the transformer winding structure and application of the compressive loads, the FEM can calculate the maximum compressive load before buckling occurs. The results of this analysis can be used to determine the safety factor of the transformer winding structure. It is the ratio of the maximum compressive load before buckling occurs to the actual operating load. As shown in Figure 2.15, safety factor greater than one indicates safe operation, while a safety factor of less than one indicates that the transformer winding structure may be at risk of failure. The safety factor obtained from this analysis could be considered as one of the parameters used to evaluate the transformer winding reliability.

© COPYRIGHT UPM

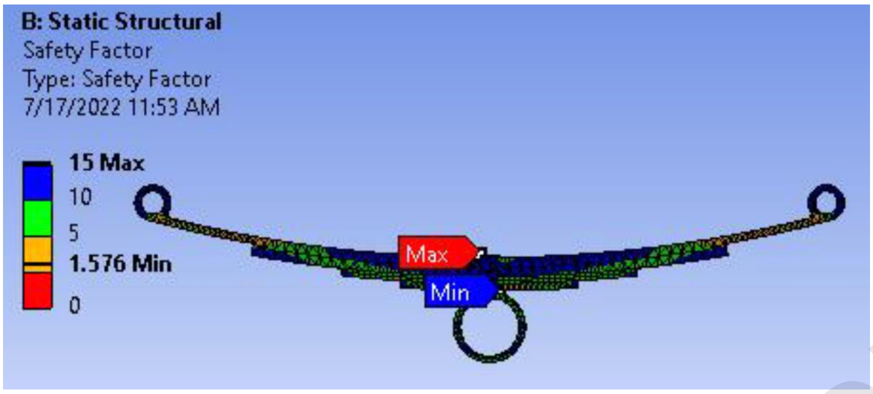

Figure 2.15: Safety factor result [137].

2.6 Summary

Despite assumptions that current impulse standards have adequately solved transient voltage issues, there remain unknown failures that may link to frequent transient phenomena that necessitate attention. Computerised testing methods are found to be very effective. The most common approach for this method is based on the equivalent circuit analysis. Another approach is the modelling of the system behaviour based on electromagnetic field theory through FEM. The derivation of these models fundamentally relies on the finite element equations. While there are various theoretical frameworks for transformer modelling under different conditions, the acquisition of data for computing model parameters is still challenging. Internal construction details are necessary to estimate these parameters, but some cannot be obtained from measurements.

In most cases, the faults within the transformer winding are considered static faults. In many practical cases, the faults are not static and typically vary during impulse voltage wave propagation along the winding. It is termed a dynamic

© COPYRIGHT UPM

fault. Identification of dynamic faults is more complex than static faults due to the simultaneous occurrence of different topologies. Therefore, there is growing interest among researchers in the identification of dynamic faults based on various conditions including transient conditions. There is ample scope for the researchers to contribute in this direction.

It has been found that transient overvoltage caused by switching transients can be detrimental to the transformer over time. The main reason is the cumulative high resonant transient subjected to the transformer. The power systems involve various switching operations and the switching transient waveform can propagate into the transformers through electromagnetic induction. As transformers are involved in complex structures and phenomena, it is found that coupling analysis based on FEM can obtain results close to the real conditions. There is a strong relationship between the electric, electromagnetic, thermal and structural parameters of the transformer that requires further analysis.

The buckling strength analysis is found to be the most suitable reliability assessment method to analyse the structural integrity of transformer windings under switching transient conditions. Although several methods have been proposed to determine the reliability of transformers under different faults, reliable identification of reliability characteristics is still an open issue due to the complex structure of the transformers

© COPYRIGHT UPM

CHAPTER 3

RESEARCH METHODOLOGY

3.1 Overview

This chapter is divided into 4 main sections. The first section discusses the disc winding model specification and verification. The following 3 consecutive sections discuss the methodology for each of the objectives. The overall research process to achieve the objectives of the study can be seen in Figure 3.1.

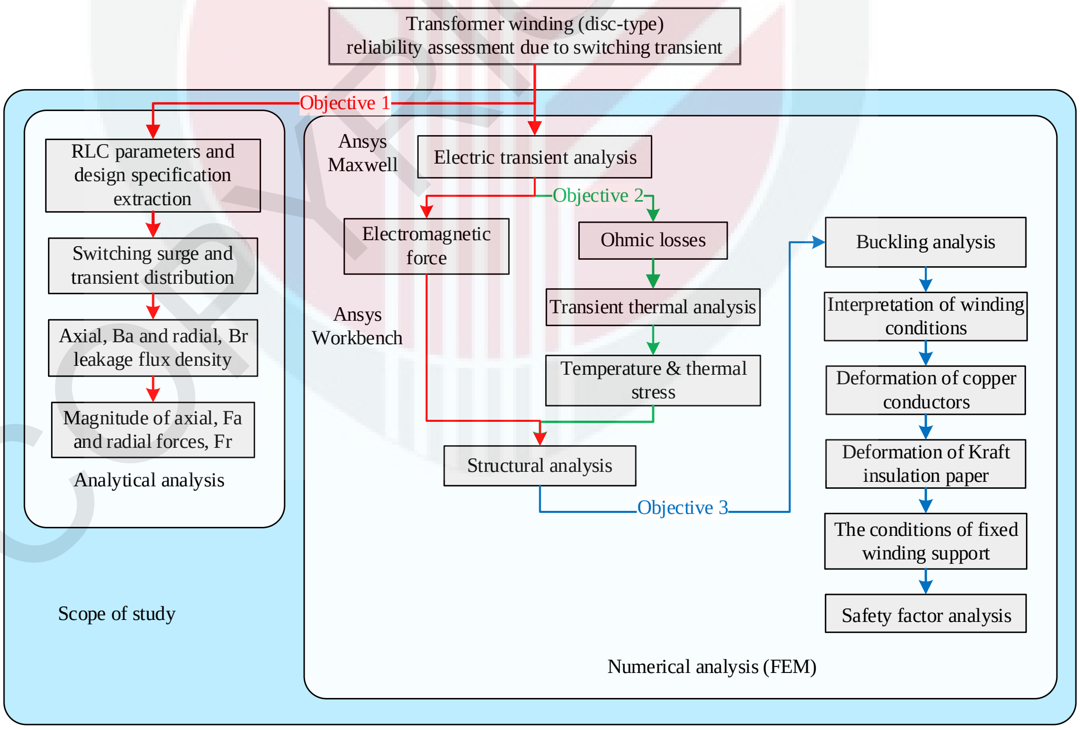

Figure 3.1: The overall research processes

The second section of this chapter illustrates the procedure for the first objective and focuses on the examination of switching transient impact on the electromagnetic force within a disc-type transformer winding. This section employs both analytical and numerical methods. The analytical approach involves calculation through mathematical formulations, while the numerical method utilises Finite Element Method (FEM).

The third section illustrates the procedures used to determine the interrelated responses of switching transients in a transformer disc winding, taking into consideration electrical, thermal and mechanical properties. The procedure involves coupling 3 sub-models, the electrical, thermal and structural transient model through the Ansys Workbench. The setup and coupling for each of the sub-models are methodically explained.

The fourth section demonstrates the methodology to compute the corresponding structural response characteristics of the disc windings based on the electrical-thermal-structural coupling analysis. The disc winding mechanical response due to electromagnetic force and thermal stress through buckling analysis is discussed in this section. Safety factor analysis is determined at the end of this section.

3.2 Modelling of disc winding for switching transient analysis

3.2.1 Disc winding model specification

© COPYRIGHT UPM

A Dyn11, 33/11 kV, 30 MVA disc-type transformer was modelled in this study. The single-phase winding consists of 96 HV discs with 25 LV layered helical windings. The actual and front cross-sectional views of the single-phase winding of the transformer can be seen in Figure 3.2 (a) and Figure 3.2 (b) respectively. The geometrical properties of the HV disc winding are shown in Table 3.1.

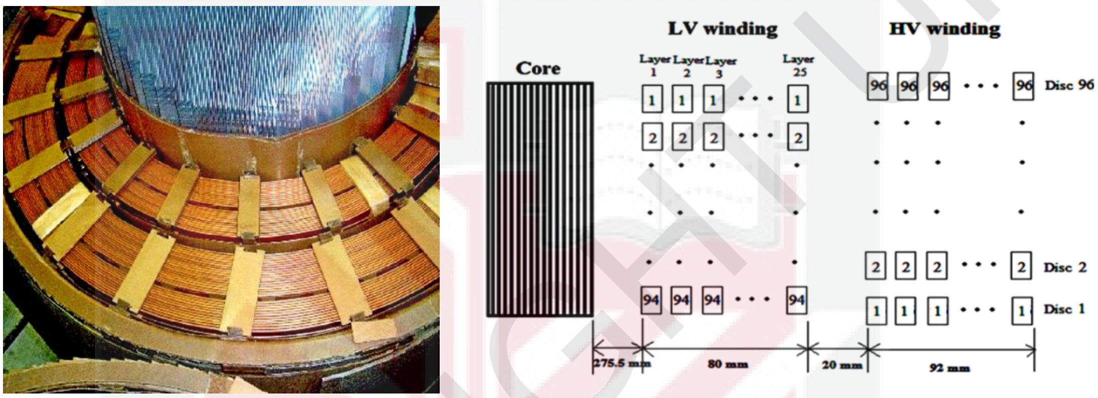

(a) (b)

Figure 3.2: (a) Actual and (b) front cross-section view of the single-phase 33/11 kV windings

Table 3.1: The HV winding geometrical properties.

Parameters	Values
Number of discs in one phase	96
Number of turns per disc	30
Height of conductor	11.5 mm
Width of the conductor	2.4 mm
The thickness of the insulation (double-sided)	0.5 mm
Distance between each disc	3 mm
Cooling duct between layers 12 and 13	5 mm
Inner radius of the HV winding	374.5 mm
Outer radius of the HV winding	466.5 mm
Total circumference of the HV winding	79.17 mm
Height of HV winding	1437 mm
Insulation between HV – LV windings (9 mm of oil + 1 mm of pressboard)	20 mm

© COPYRIGHT UPM

In this study, only HV winding was modelled and analysed since the electromagnetic forces and stresses by the excitation inrush during switching mainly affect the HV winding side [116]. The modelling of the disc winding was simplified and considered an ideal winding model. Only the 8 topmost disc windings were modelled and examined due to the limitation of the high-speed computation capabilities. Since switching transient primarily affects the uppermost discs, the localised 8 disc model effectively captures the most critical voltage stress regions. The selected section ensures that transient overvoltages and resonance effects are still accurately represented without modelling the entire winding. The 8 disc model provides valuable insight into localised switching impulse effect which can be extrapolated to estimate the full winding's mechanical response. This winding proportion was found sufficient to emulate the switching transient phenomenon [96].

The 3D model was constructed in Ansys Maxwell based on the actual geometrical design and material properties of the HV disc winding. The model construction mainly focuses on the disc winding arrangement, conductor shapes, insulation layers and winding support structures. It consists of 8 discs proportioned with 5 symmetric turns and a continuous arrangement of 6 conductors insulated with the insulation papers. The connection at the end of each disc layer was left open due to simplification of the complex specification of the interleaved connection. The fixed supports were placed vertically at the inner and outer layers of the winding to simulate clamping as seen in Figure 3.3.

© COPYRIGHT UPM

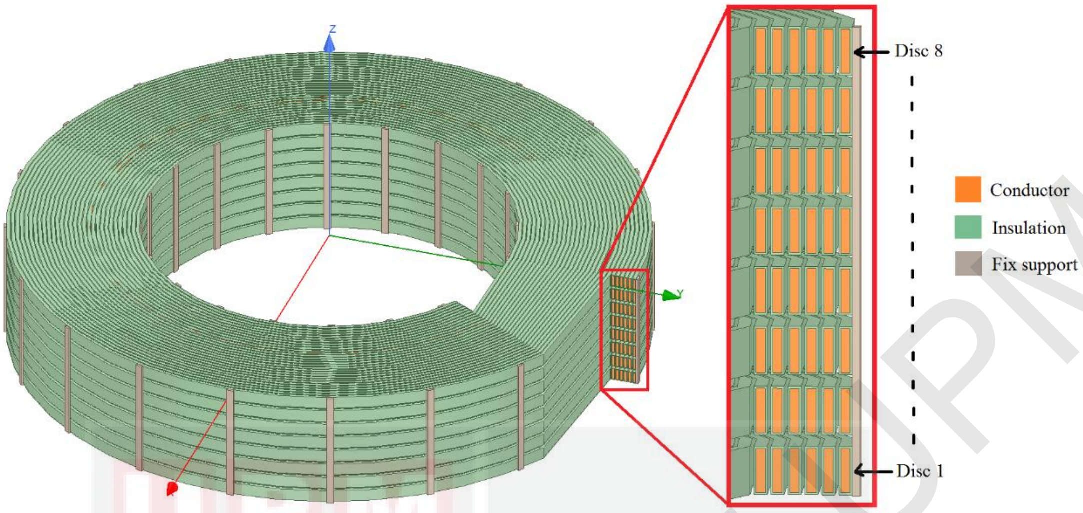

Figure 3.3: Details of HV disc winding model

The effect of the iron core was neglected in various inductance models used for voltage transient studies including this study, as explained in Section 2.4.2.1. The spacers were not considered in the transient modelling since it was not electrically active and did not significantly impact the mechanical aspect of the transient response. In terms of the computational aspect, the spacers were omitted to reduce the disc winding complexity and balance the model accuracy and computational efficiency for this analysis. The test was assumed to be conducted under vacuum to represent dry conditions. The insulating oil was not considered in the study since the focus was on the performance of the internal winding conditions.

3.2.2 Validation of disc winding model

The 3D geometric model validation was performed based on a similar approach to [77], [138], whereby the comparison was carried out with the measured initial voltage distribution. The study showed good agreement between the simulated and measured initial voltage distribution, which indicates that the geometric model was adequate and applicable to this analysis. The electric field based on Maxwell's equations was calculated based on Equation (3.1) [139].

$$E = -\frac{\partial A}{\partial t} - \nabla V \tag{3.1}$$

Taking the integral of both sides of Equation (3.1) with respect to length in the cylindrical coordinates and the relation of $J=\sigma E$, the voltage drops on the *j* conductor due to the current on the conductor *i* can be calculated based on Equation (3.2).

$$V_j = 2\pi r\left(\frac{J_{rj}}{\sigma} + j\omega A_{rj}\right) \tag{3.2}$$

where J_{rj} and A_{rj} are the current density and vector potential point on the conductor *j* with the radius of *r.* σ is the conductivity of the *j* conductor. Each of the HV discs is in series thus, the total voltage drop is equal to the sum of the voltage drops on all of the discs. The voltage distribution based on the analytical method can be calculated based on Equation (3.3) [140].

$$V_{dist} = \frac{V_p(\alpha/l)x}{\alpha} \tag{3.3}$$

$$\alpha = \sqrt{\frac{c_g}{c_s}}$$

© COPYRIGHT UPM

where *l* is the height of the winding, *x* is the layer distance from the neutral point, V_p is the voltage peak of input impulse and V_{dist} is the voltage distribution for each disc layer. α is the capacitive characteristic coefficient, C_g is ground capacitance and C_s is the series capacitance of the winding. The calculation to get the C_g and C_s can be seen in section 3.3.2.

A statistical indicator, the Correlation Coefficient Factor (CCF) was applied to measure the differences between the measured and calculated initial voltage distribution curves. This method provides a single value on the extent of the variation between the curves. The CCF index is expressed as Equation (3.4) [141].

$$CCF = \frac{\sum_{i=1}^{N}\left(\left((x_i-\bar{x})\times(y_i-\bar{y})\right)\right)}{\sqrt{\sum_{i=1}^{N}(x_i-\bar{x})^2\times\sum_{i=1}^{N}(y_i-\bar{y})^2}} \quad (3.4)$$

From the equation, x_i and y_i are the *i*-th values in p.u from the data set of *x* and *y*. $\bar{x}$ and $\bar{y}$ are the mean values of the data set of *x* and *y*. *N* is the size of the data set. Here, *x* and *y* are the measured and simulated initial voltage distribution respectively. The positive correlation indicates that the two variables react the same way, increasing or decreasing. Meanwhile, a negative correlation indicates a condition that is vice versa. The CCF can decrease from 1 to 0 as the correlation between the 2 curves decreases.

© COPYRIGHT UPM

3.3 Methods to analyse switching transient's impact on electromagnetic force of disc-type winding

This study considers analytical and numerical methods to analyse the impact of switching transients on the electromagnetic force in a disc-type winding. The analytical method was carried out based on the mathematical calculation from the formula derivation of electromagnetic force with respect to the disc winding geometric design through MATLAB. The numerical method was performed based on the 3D disc winding model simulation via electric transient analysis through the Ansys Maxwell. The overall procedure to obtain the resultant electromagnetic forces in axial and radial directions during the switching transient can be seen in Figure 3.4.

© COPYRIGHT UPM

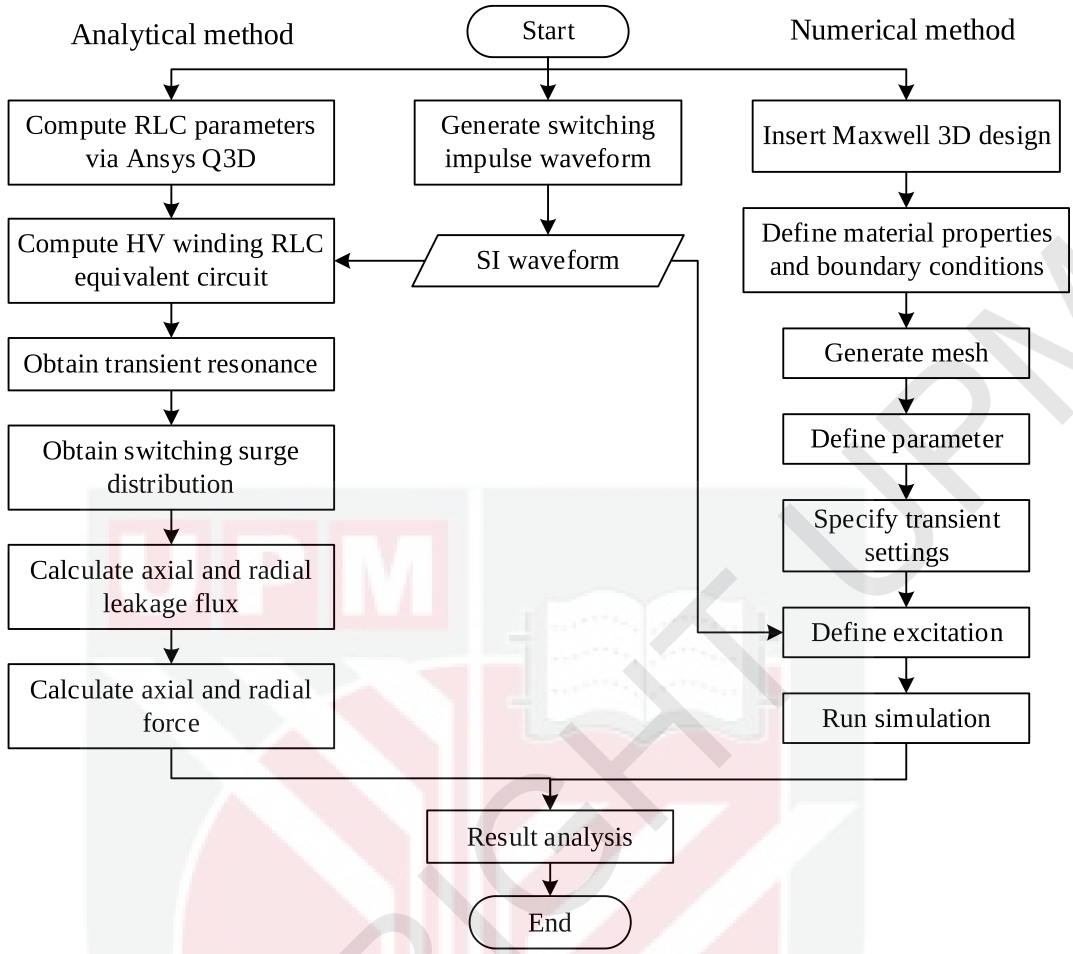

Figure 3.4: Overall methodology for objective 1

For the analytical analysis, the RLC elements of the disc winding were first computed through the quasi-state Ansys Q3D platform. The computed RLC elements were used to develop the disc winding RLC equivalent circuit. Next, the switching impulse waveform was subjected to the RLC equivalent circuit to obtain the transient resonance and surge distribution in the disc windings. Lastly, the electromagnetic force was calculated based on the axial and radial electromagnetic force equations.

For the numerical analysis, the simulation started with the setup of the electric transient, including the material property, boundary condition of the winding geometry, excitation, mesh operation, and electromagnetic force under the switching transient. The solve setup defined the times taken for the transient simulation, stop time, initial and maximum time steps. Finally, the electromagnetic force in the winding was simulated.

3.3.1 Generation of standard and non-standard switching impulse waveform

The nominal voltage of the primary winding is 33 kV under normal operating conditions. During switching transient, the primary disc winding experiences a SI overvoltage. The voltage in p.u is defined as the ratio of actual voltage to the base voltage, $V_{p.u} = V_{actual}/V_{base}$. For this case, the actual voltage is the switching impulse voltage and the base voltage is the peak phase-to-earth voltage of the transformer winding, 33 kV. This analysis considered the highest magnitude of a switching surge which is 5 p.u and equivalent to 165 kV. The SSI voltage waveform of 250/2500 µs was generated by the impulse generator circuit as demonstrated in Figure A.1, Appendix A. The 165 kV magnitude SSI voltage waveform can be seen in Figure 3.5.

© COPYRIGHT UPM

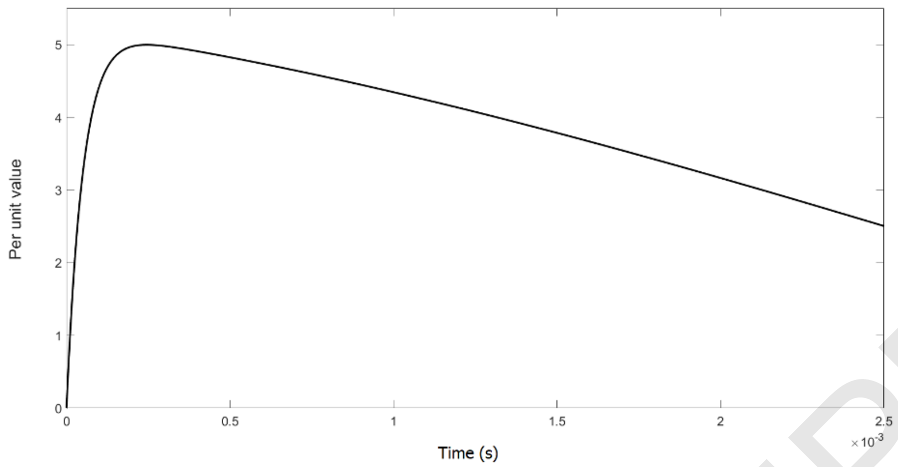

Figure 3.5: 165 kV SSI voltage waveform

In this case study, the non-standard switching impulse waveform is due to the energisation of a transmission line during power system restoration generated in the actual field. This analysis considered the highest impulse magnitude of 3.3 p.u which was equivalent to 108.9 kV [30]. The NSSI voltage waveform was obtained through data extraction, where key voltage points were obtained from actual field measurements. These extracted data points were then used to generate the NSSI voltage waveform through curve fitting techniques and can be seen in Figure 3.6.

© COPYRIGHT UPM

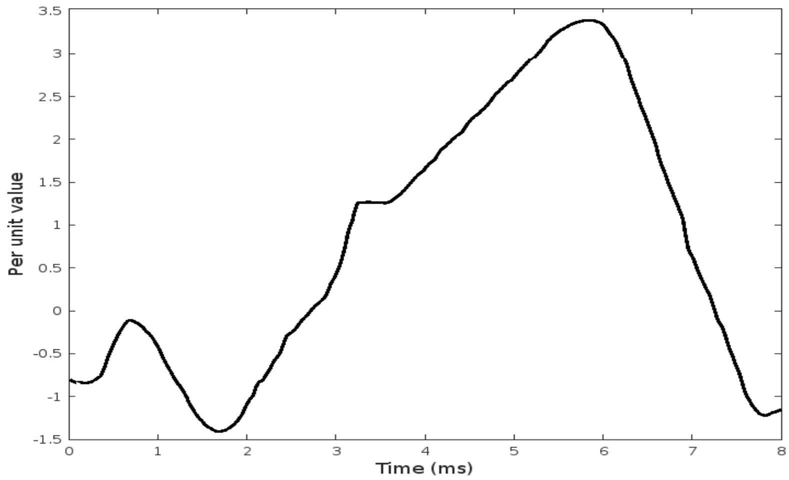

Figure 3.6: Switching impulse voltage waveform due to energisation of transmission line [30]

3.3.2 The transient resonance on disc winding due to the switching impulses

The analysis of transient resonance on a disc winding subjected to the switching impulse was carried out through the RLC equivalent circuit. The RLC equivalent circuit of the 96 HV discs winding is shown in Figure 3.7.

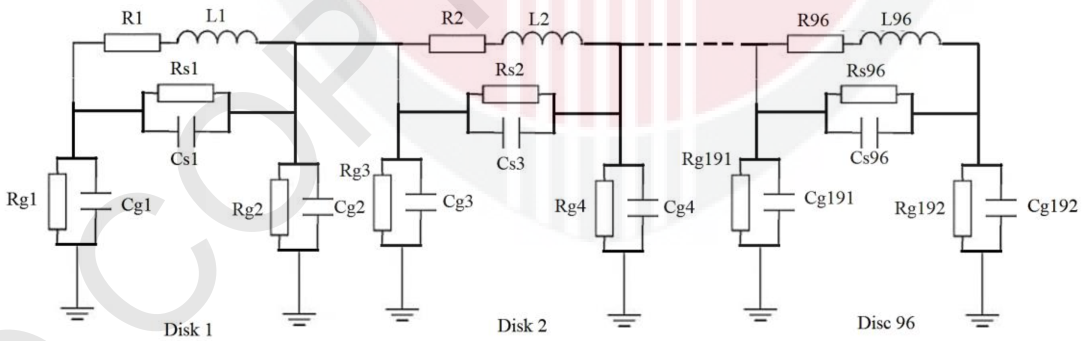

Figure 3.7: Disc winding RLC equivalent circuit

The RLC equivalent circuit of the 96 HV disc winding is structured in a series-parallel configuration, representing the electrical behavior of transformer windings under switching impulses. Each disc winding consists of series

© COPYRIGHT UPM

resistance (Rs), capacitance to ground (Cg), conductance (Gs), self and mutual inductance (M_L). The series connection of R and L elements simulates the longitudinal current flow, while the parallel capacitors represent insulation effects and voltage distribution. The mutual inductance between discs influences transient voltage propagation, causing reflections and resonances. This interconnected network determines how switching impulses travel through the winding. The SSI waveform is applied to the RLC equivalent circuit of the disc winding through inductive coupling with the impulse generator circuit. Voltage measurement probes capture the impulse response and analyse resonance effects. For the NSSI voltage, the impulse generator circuit is replaced with a controlled voltage source using a waveform source block.

The natural frequency, f_0 of the RLC circuit was determined based on the L and C according to the formula, $f_0 = \frac{1}{2\pi\sqrt{LC}}$. This frequency represents the inherent oscillation tendency of the circuit once subjected to external excitation. Once the switching impulse waveform was applied, its frequency components interacted with the natural frequency of the RLC circuit. The frequency of the switching impulse was set close to the natural frequency. The resonance would occur and accelerate energy exchange between the inductive and capacitive elements of the RLC circuit. The energy in the inductor was transferred to the capacitor and vice versa, which led to sustained oscillations in the waveforms.

© COPYRIGHT UPM

3.3.3 The axial and radial forces based on analytical method

The HV winding's nominal and Basic Impulse Level (BIL) voltages are 34.5 kV and 200 kV respectively. An assumption was made whereby the HV winding was solidly grounded. The crest voltage for the switching impulses was set below the rated BIL of the HV winding with a protection margin of 21%. This switching impulse voltage was applied superimposed on each disc windings to determine the total electromagnetic force. For this case study, 1 cycle of switching impulse voltage waveform obtained from the switching impulse voltage generator circuit was applied as the input data for the electromagnetic force analysis. Figure 3.8 shows the overall scheme of the switching impulse voltage application on the disc winding.

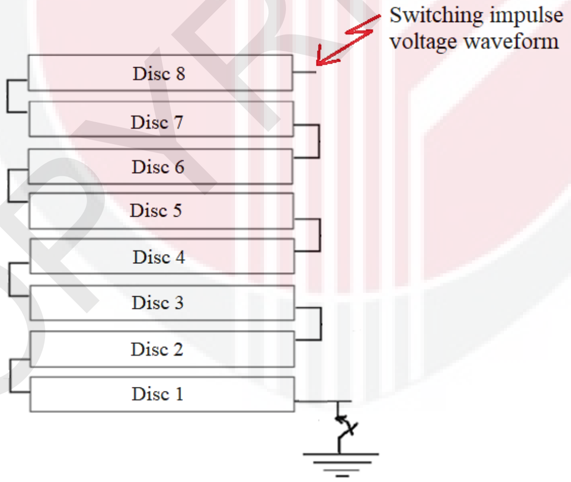

Figure 3.8: Schematic representation of switching impulse voltage application on the disc winding

The analytical method was employed to compute the forces subjected to each disc layer. The radial F_r and axial F_a directed forces were calculated based on the winding geometrical design based on Equations (3.5) and (3.6) [142].

$$F_r = \frac{2\times\pi^2\times(NI)^2\times D_m\times 10^{-7}}{h} \quad (3.5)$$

$$F_a = \frac{2\times\pi^2\times A\times(NI)^2\times D_m\times 10^{-7}}{h_{eff}} \quad (3.6)$$

where h is the length of the winding and h_{eff} is the effective length of the radial flux path, where it is calculated as 0.222 x h. D_m is the mean winding diameter, ampere-turn (NI) is the ampere turn of the winding and A is the winding's total length. The F_r was calculated based on the free distance between 2 windings as the axial flux density (B_a) between the windings. F_r was assumed to be constant along the length of the winding. It was generated by the integration of the instantaneous NI in each of the windings as well as the leakage flux was derived as Equation (2.1). The F_a was calculated based on the Residual NI Method [143]. It is the relationship between the radial flux density (B_r), the average of NI at the total length of winding and the effective length of radial flux path (h_{eff}).

3.3.4 The electromagnetic force analysis based on numerical method

The electromagnetic force solution was carried out using the electric transient analysis setup. The boundary condition was set as natural and switching impulse waveform was applied as the excitation on the winding to establish the transient phenomena. The electromagnetic force of the winding was computed based on the Lorentz force equations. The meshes were constructed using adaptive length and skin depth-based refinement

© COPYRIGHT UPM

techniques to increase the accuracy of force analysis in the winding. The winding model is composed of 926,167 nodes and 369,168 elements.

The transient setup was set from 1 µs to 2500 µs with the minimum and maximum time steps of 0.01 µs and 5 µs respectively. For the 3D modelling, the calculation of the magnetic plane was defined as (*x,y,z*) since the current was normal to the plane [144]. The component of leakage flux density was expressed as vector potential as in Equation (3.7) [108].

$$B_x = -\frac{\partial A_\phi}{\partial_z}, \qquad B_y = 0, \qquad B_z = \frac{1}{x}\frac{\partial\ (xA_\phi)}{\partial_x} \tag{3.7}$$

where B_x, B_y and B_z are directional components of leakage flux density and A_ϕ is the magnetic vector potential. Lorentz force was employed to express the electromagnetic force on the winding as seen in Equations (3.8) and (3.9) [107].

$$F = \int_V J_y \hat{y} \times (B_x \hat{x} + B_z \hat{z}) dv = F_x \hat{x} + F_z \hat{z} \tag{3.8}$$

$$F_x = B_z \times J_y, \quad F_z = B_x \times J_y \tag{3.9}$$

where, J_y is the y-directional current density, $\hat{x}, \hat{y}$ and $\hat{z}$ are the unit vectors in the winding plane. The F_x and F_z represent the radial and axial force, respectively.

© COPYRIGHT UPM

3.4 Electrical, thermal and mechanical solver analyses

In order to achieve the second objective of study, 3 sub-models known as electric, thermal and structural transients were developed and coupled via Ansys Workbench. The electric transient model was used to compute ohmic losses in the disc winding. The transient thermal model was used to compute the winding temperature and total heat flux from the ohmic losses. The transient structural model evaluates the displacement and deformation of the disc winding due to thermal stress. Figure 3.9 shows the schematic of the electric-thermal-structural transient coupling analysis.

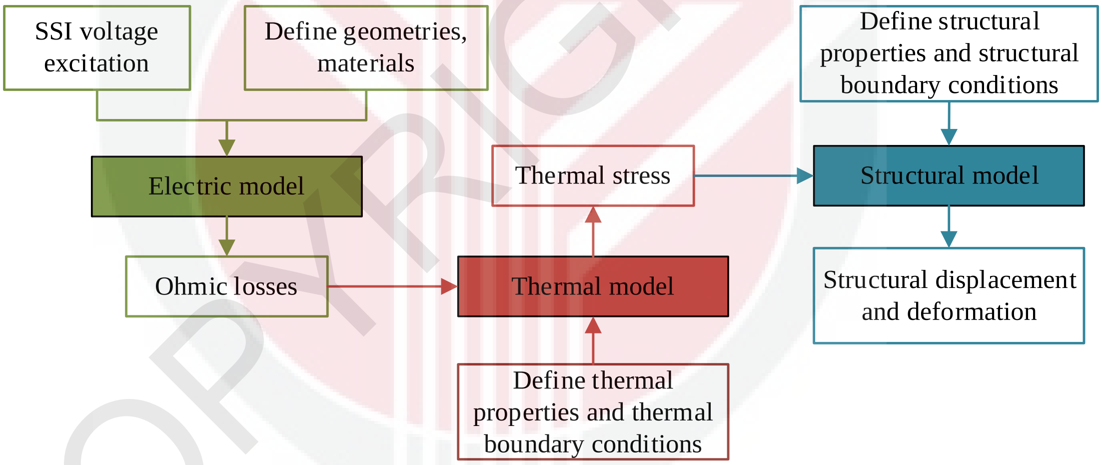

Figure 3.9: Schematic of electric-thermal-structural transient coupling analysis

The electric model was analysed in the Maxwell 3D Design toolbox based on electric transient solver. This step defines the 3D geometry of the transformer disc winding. This includes creating the physical structure that will be analysed in the subsequent step. The main input excitation was the SSI voltage waveform. The thermal model was analysed in the transient thermal toolbox.

The input excitation was the ohmic losses from the electric transient analysis. The structural model was analysed in the transient structural toolbox. The input excitation is thermal stress from the transient thermal analysis. The geometry defined in the Maxwell 3D is used in the transient thermal and structural analysis. This ensures that both analyses are performed on the same physical structure used for the electric transient analysis. The time-dependent coupling analysis was used to foresee the ohmic losses, temperature distribution, thermal stress and force concentration profile across the disc winding under the switching transient.

Due to the nature of the faulty transformer symmetrical structure, the 3D geometric model was split into 4 symmetrical parts. The setting of symmetry boundary conditions leads to efficient computational tasks in terms of space and run times. The 3D geometric model of the disc winding can be seen in Figure 3.10. Figure 3.10 (a) shows the top view and Figure 3.10 (b) shows the trimetric view of the ¼ symmetrical model. The disc model material was set into 3 elements which were 2 deformable parts and 1 fixed rigid barrier. Conductor and insulation paper are the deformable parts, while fixed support is the rigid barrier. The model was subjected to a mesh of free tetrahedrons network as shown in Figure 3.11. It was composed of 492 active bodies, 2,678,899 nodes and 1,271,896 elements.

© COPYRIGHT UPM

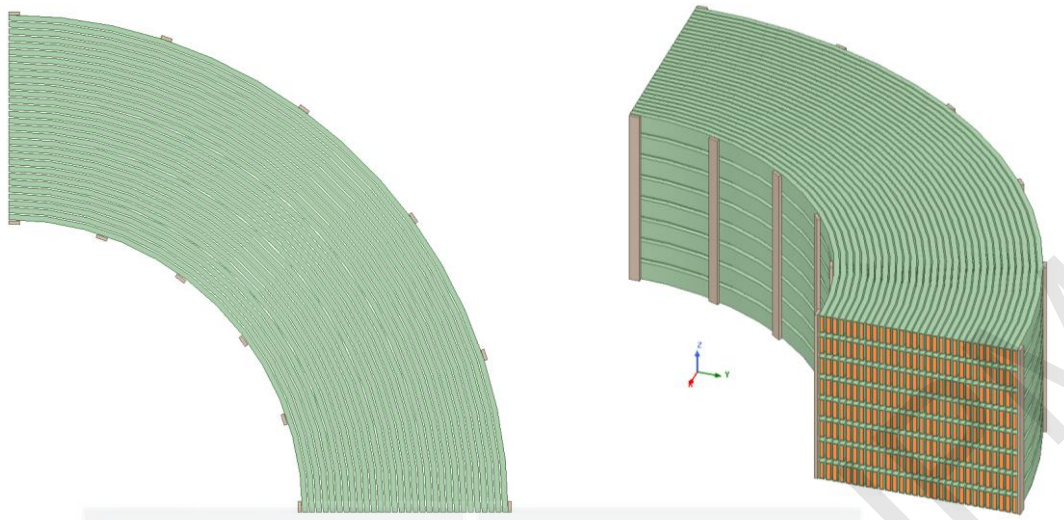

(a) (b)

Figure 3.10: (a) Top and (b) trimetric view of the ¼ symmetrical disc winding model

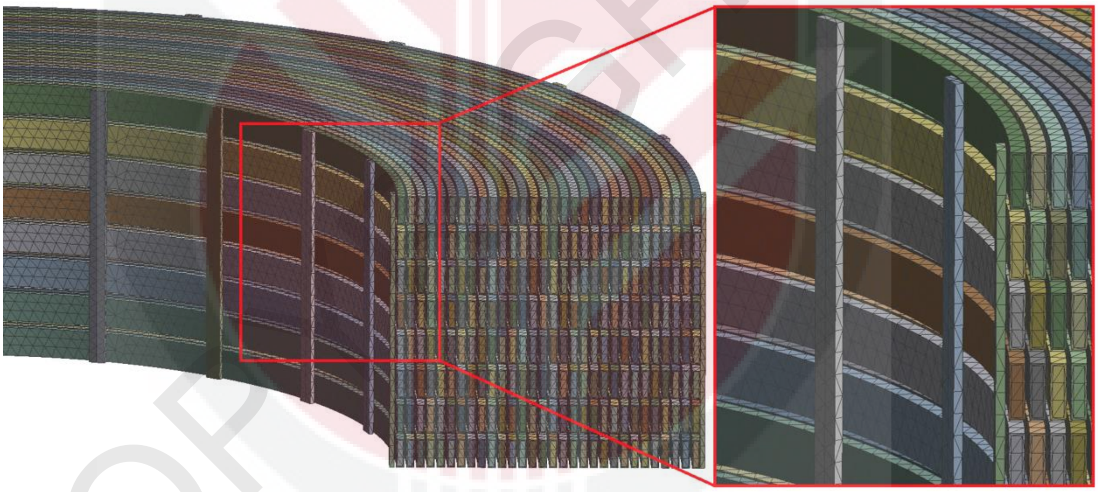

Figure 3.11: Meshing of the disc winding model

3.4.1 Electric Transient Analysis

The electric transient solver computes the time-varying electric fields within the lossy conductors and insulators. The material properties were set to vary with the temperature. The temperature-dependent material properties ensured that the winding properties responded to thermal conditions. The model considered

© COPYRIGHT UPM

conductivity and mass transfer characteristics mainly along the transverse direction of the winding and the electrical loss reactions in its perpendicular direction. It describes the time-dependent behaviour of the electric potential in the winding conductors and it can be expressed by Equation (3.10) [58].

$$-\nabla\left(\epsilon\nabla\frac{\partial\Phi}{\partial t}\right)-\nabla\left(\sigma\nabla\Phi\right)=0 \tag{3.10}$$

where ϵ is the permittivity of the material, Φ is the electric potential in the conductor, σ is the material conductivity and *t* is time. The main transformer losses that contribute to temperature rise are copper and core losses [145]. Core losses were omitted since the air core was considered in this case. The copper losses are caused by the resistance of the winding conductor and are known as the ohmic losses. The resistance *R* of a conductor was calculated using Equation (3.11).

$$R=\rho\frac{l}{A} \tag{3.11}$$

where ρ is the resistivity of the copper conductor material with a temperature-dependent relation. The *l* and *A* are the length and cross-sectional area of the conductor. Due to the skin effect, the effective cross-sectional area of the conductor, A_{eff} decreased due to the reduction of the penetration depth. The penetration depth ς in a highly conductive medium was excited at an angular frequency of $\omega=2\pi f$. The A_{eff} and ς can be expressed using Equations (3.12) and (3.13) [146].

© COPYRIGHT UPM

$$\zeta = \sqrt{\frac{2}{\omega\mu\sigma}} \tag{3.12}$$

$$A_{eff} = Ae^{-\frac{d}{\delta}} \tag{3.13}$$

where μ is the relative permeability and σ is the conductivity of the copper conductor. *A* is the original cross-sectional area and *d* is the distance from the surface. The total ohmic losses, P_{OL} during the switching transient is related to the finite resistivity of the copper material and can be obtained by Equation (3.14) [147].

$$P_{OL} = \int_V \rho \ J^2 \, dV \tag{3.14}$$

where ρ is the resistivity of the conductor material and *J* is the current density vector. The P_{OL} is obtained from the integration of ρ and *J* over the volume of the copper conductor. The ohmic losses refer to the regions for losses output correspond to the winding conductor due to its resistance. The winding electrical properties are shown in Table 3.2.

Table 3.2: Electrical properties for electric transient analysis

Part	Materials	Density, ρ (Kg/m^3)	Conductivity, σ (S/m)	Permittivity, ϵ (F/m)
Conductor	Copper	8700	58.5×10^6	1×10^{-11}
Insulation	Kraft paper	930	0	3
Fixed support	Steel	7850	1×10^6	1×10^{-11}

© COPYRIGHT UPM

3.4.2 Electric-Thermal Transient Analysis

The transient thermal modelling process begins by setting the winding thermal properties such as the specific heat capacity, thermal conductivity and initial temperatures in the simulation. The initial temperature was set to ambient temperature which is 30 °C. The thermal properties of the winding material are defined in Table 3.3.

Table 3.3: Thermal properties used for thermal analysis

Materials	Thermal conductivity, K (W/m˚C)	Coefficient of Thermal Expansion (K^{-1})	Specific heat, C (J/kg˚C)
Copper	398	1.7×10^{-5}	385
Kraft paper	0.19	10×10^{-5}	2093.5
Steel	45	1.2×10^{-5}	3.34×10^{5}

In this analysis, the ohmic losses from the electric transient analysis were transferred to the thermal transient setup as an input excitation in the form of a volumetric heat source. The volumetric heat source refers to the region for temperature inputs corresponding to winding conductors with the temperature dependent properties. In system coupling analyses, data transfers were achieved via mesh mapping. Mapping quality depends on the proportion of the target mesh locations that receive data directly from source mesh locations and the proportion of source mesh locations that are used in those target data calculations. The temperature distribution in the winding was obtained by the heat transfer mechanisms in the thermal transient analysis as shown in Figure 3.12.

© COPYRIGHT UPM

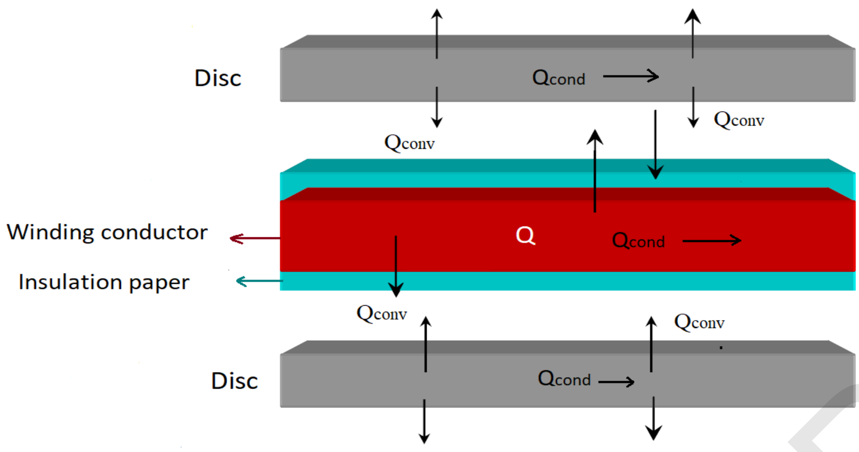

Figure 3.12: Heat source and transfer mechanisms

The heat source and transfer mechanisms determine the thermal boundary conditions set up for the thermal analysis. There were 3 main thermal boundary conditions considered in this analysis. The Q is the internal heat generation rate per unit volume by ohmic losses set in the copper conductor. The Q_{cond} is the conduction heat flux set between the conductor and insulation paper. The Q_{conv} is the convection heat transfer set at the surfaces between each disc. The transient heat conduction in 3D Cartesian coordinate system is governed by Equations (3.15) and (3.16) [125].

$$-\left(\frac{\partial q_x}{\partial x}+\frac{\partial q_y}{\partial y}+\frac{\partial q_z}{\partial z}\right)+q_v=\rho C_p\frac{\partial T}{\partial t} \tag{3.15}$$

$$-\left(\frac{\partial}{\partial x}\left(k_x\frac{\partial T}{\partial x}\right)+\frac{\partial}{\partial y}\left(k_y\frac{\partial T}{\partial y}\right)+\frac{\partial}{\partial z}\left(k_z\frac{\partial T}{\partial z}\right)\right)+q_v=\rho C_p\frac{\partial T}{\partial t} \tag{3.16}$$

where q_x, q_y and q_z are the conduction heat fluxes, k_x, k_y and k_z are the winding material thermal conductivities in x-, y- and z-directions. q_v is the rate of internal heat generation per unit volume, ρ is mass density of the winding material, C_p is the specific heat capacity of the winding material and T is the temperature

© COPYRIGHT UPM

that varies with the coordinated as well as the time, *t*. The equivalent thermal conductivity of copper conductor insulated with kraft paper can be obtained as Equation (3.17) [125].

$$\lambda_x = \frac{\lambda_{1x}\lambda_{2x}(d_1 + d_2)}{d_1\lambda_{1x} + d_2\lambda_{2x}}$$
$$\lambda_y = \frac{\lambda_{1y}\lambda_{2y}(d_1 + d_2)}{d_1\lambda_{1y} + d_2\lambda_{2y}} \quad (3.17)$$
$$\lambda_z = \frac{\lambda_{1z}\lambda_{2z}(d_1 + d_2)}{d_1 + d_2}$$

where λ_{1x}, λ_{1y}, λ_{1z} and λ_{2x}, λ_{2y}, λ_{2z} are the thermal conductivities of copper conductor and kraft paper insulation in x, y and z directions, respectively. d_1 and d_2 are the thickness of the copper conductor and kraft paper insulation. The winding was assumed to be in the condition of surrounding air without external cooling therefore natural convection heat transfer was considered in this analysis. The natural convection heat transfer between each of the disc winding surfaces can be calculated by Equations (3.18) – (3.20) [85], [102].

$$T = T_1(x, y, z, t) \quad (3.18)$$

$$Q_{conv} = h(T - T_a) \quad (3.19)$$

$$h = \frac{k}{l}Nu \quad (3.20)$$

where, T_1 is the specified surface temperature, *h* is the convection heat transfer coefficient, *T* is the winding surface temperature and T_a is the ambient temperature. ε is the thermal emissivity of the material, *k* is the thermal conductivity of air, *l* is the surface length, Nu is the Nusselt number. The

© COPYRIGHT UPM

temperature distribution within the disc winding can be expressed by Equations (3.21) and (3.22) [85].

$$\rho C_p\left(\frac{\partial T}{\partial t} + u\,\nabla T\right) + \nabla(k\nabla T) = -(\sigma{:}\,D) + Q \tag{3.21}$$

$$\rho C_p\left(\frac{\partial T}{\partial t} + u\,\nabla T\right) + \nabla\,(q + q_{conv} + q_{cond}) = -\alpha T{:}\frac{dS}{dt} + Q \tag{3.22}$$

where T is the absolute temperature, t is time, u represents the velocity vector of translational motion, k is the material thermal conductivity, q is the heat generation in the winding conductor, q_{cond} is the heat transfer in the winding conductor by conduction, q_{conv} is the heat transfer between disc to disc surface structure by convection, α is the coefficient of thermal expansion, S is the second Piola-Khirchoff stress tensor, Q is additional heat sources, σ is the Cauchy stress tensor, and D represents the strain rate tensor. The operator ":" represents the contraction operator.

3.4.3 Thermal-Structural Transient Analysis

The temperature distribution from the thermal analysis was transferred to the structural analysis. The thermal-structural coupling was established by mapping the temperature field onto the structural model with consideration of the thermal expansion coefficient of the winding materials. This process ensures that the mechanical response of the windings can be accurately simulated based on the thermal stresses which can be expressed by Equation (3.23) [54].

© COPYRIGHT UPM

$$\rho A \frac{\partial^2 u}{\partial t^2} + \nabla \sigma_{thermal} = F \quad (3.23)$$

where ρ is the density, A is the cross-sectional area, u is the displacement, t is the time, σ is the thermal stress and F is the applied force. The boundary condition to simulate the structural analysis was fixed support. The support refers to the physical constraints applied to the winding structure to replicate real world conditions in the structural analysis that restrict displacement and rotation in all directions. Its primary purpose is to represent the effect of the clamping mechanism that holds the winding in place within the transformer. It was placed at the inner and outer structural steel fix supports of the disc winding to simulate clamping and physical constraints on the disc winding structure as shown in Figure 3.13.

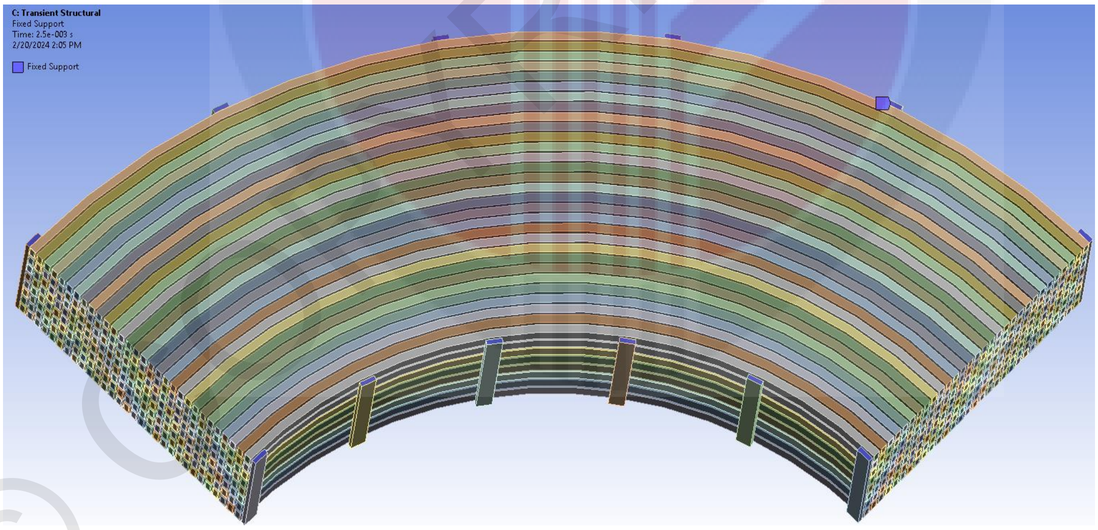

Figure 3.13: Positions of fixed support boundary condition

© COPYRIGHT UPM

3.5 Structural behaviours analysis of disc winding due to thermal effect.

In order to achieve the third objective of study, the total stress in the disc winding computed through the three-way coupling of electric-thermal-structural analysis was further investigated. The buckling analysis considers electromagnetic force and thermal stress as primary influencing factors. The electromagnetic force and thermal stress contribute to structural instability that leads to buckling analysis. The windings experience either compressive strain or tensile strain. The extent of these deformations is analysed to assess the mechanical integrity of the windings. Then, stress-strain curves are plotted to visualise the material's responses. Finally, a safety factor evaluation is conducted. The flow chart for this objective is presented in Figure 3.14.

© COPYRIGHT UPM

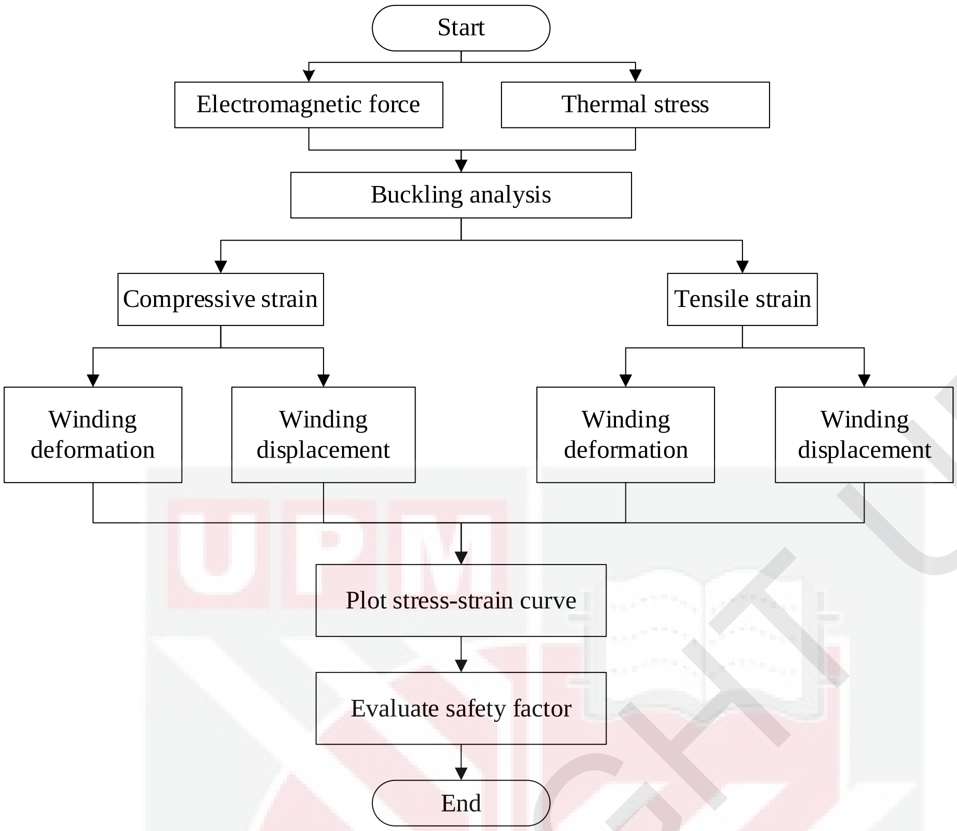

Figure 3.14: Methodology flow chart to achieve objective 3

3.5.1 Behaviours of disc winding deformation and displacement

The thermal stress, $\sigma_{thermal}$ from the constraint thermal expansion or contraction related to the thermal strain can be expressed by Hooke's law, Equation (3.24) [148].

$$\sigma_{thermal} = \alpha \times \Delta T \times E \tag{3.24}$$

where α is the coefficient of thermal expansion of the winding material, ΔT refers to the change in temperature and E is the modulus of elasticity or Young's modulus of the winding material. Once there is stress, the elastic strain and deformation or displacement can be initiated. The deformation can be defined by elastic-plastic deformation, stress and strain control. The relation between stress and mass force in space can be described based on Equation (3.25) [149].

$$\begin{cases} \frac{\partial \sigma_r}{\partial r} + \frac{\partial \tau_{zr}}{\partial z} + \frac{\sigma_r - \sigma_\theta}{r} + f_r = 0 \\ \frac{\partial \sigma_z}{\partial z} + \frac{\partial \tau_{rz}}{\partial r} + \frac{\tau_{rz}}{r} + f_z = 0 \end{cases} \tag{3.25}$$

where f_r and f_z are the radial and axial forces exerted on the winding. σ_r, σ_θ and σ_z are the radial, tangential and axial stresses. The displacement is described by the relationship between strain and displacement. The strain displacement describes how the applied forces on the winding cause it to deform and result in displacement of the winding. The strain displacement can be expressed by Equation (3.26).

$$\begin{matrix} \varepsilon_r = \frac{\partial u_r}{\partial r} & \varepsilon_\theta = \frac{u_r}{r} \\ \varepsilon_z = \frac{\partial u_z}{\partial z} & \gamma_{rz} = \frac{\partial u_r}{\partial z} + \frac{\partial u_z}{\partial r} \end{matrix} \tag{3.26}$$

where ε_r, ε_θ, and ε_z are the radial strain, tangential and axial strain, γ_{zr} is the shear strain, u_r and u_z are the radial and axial displacements. The relationship between stress and strain in space can be expressed by Equation (3.27).

$$\begin{cases} \varepsilon_r = \frac{1}{E}[\sigma_r - \mu(\sigma_\theta + \sigma_z)] & \varepsilon_\theta = \frac{1}{E}[\sigma_\theta - \mu(\sigma_z + \sigma_r)] \\ \varepsilon_z = \frac{1}{E}[\sigma_z - \mu(\sigma_r + \sigma_\theta)] & \gamma_{zr} = \frac{2(1+\mu)}{E}\mathcal{T}_{zr} \end{cases} \tag{3.27}$$

© COPYRIGHT UPM

where T_{zr} is the shear stress, μ is the Poisson ratio of the winding material and E is the Young's Modulus. The mechanical properties of the winding material for structural analysis are presented in Table 3.4.

Table 3.4: Mechanical properties for structural analysis

Material	Young's modulus (GPa)	Tensile yield strength (MPa)	Shear modulus (GPa)	Poisson Ratio
Copper	113	50	43.69	0.3
Kraft paper	1.1	10.9	0.55	0.001
Steel	200	250	76.92	0.3

3.5.2 Stress-strain and load-displacement curve

The deformation state and cumulative effect of the disc winding caused by the switching transient can be analysed by the internal state of the winding. The general relationship between stress and strain is given by Hooke's Law in the elastic region as shown in Equation (3.28) [150].

$$\sigma = E \times \varepsilon \tag{3.28}$$

where E is the elastic modulus. Based on elastic mechanic theory, the stress-strain field can be obtained by Equation (3.29) [150].

$$\begin{cases} \sigma_{xy,y} + f_x = 0 \\ \varepsilon_{xy} = \frac{1}{2}(u_{x,y} + u_{y,x}) \\ \varepsilon_{xy} = \frac{1+v}{E}\sigma_{xy} - \frac{v}{E}\sigma_{zz}\delta_{xy} \end{cases} \tag{3.29}$$

© COPYRIGHT UPM

where $\sigma_{xy,y}$ is the stress tensor, f_x is the transient volume force density of the electromagnetic force during the switching transient. ε_{xy} is the strain tensor, $u_{x,y}$ is the displacement tensor. E and v are Young's modulus and Poisson's ratio of winding material, respectively. This study only focuses on the stress-strain relationship of copper conductor material.

The load-displacement curve plots show how much load is required to deform the material by a certain amount and how much energy is absorbed by the material during the deformation. The general relationship between load and displacement can be done by relating the load to the force and the displacement to the strain. The substitution of Hooke's Law into force equation is shown in Equation 3.30 [150].

$$F = E \times \varepsilon \times A \tag{3.30}$$

where F is the applied force, A is the cross-sectional area over which the force is applied. Strain is defined in Equation 3.37. Substitution of strain into force gives the load-displacement curve relationship as Equation 3.31.

$$\varepsilon = \frac{\Delta L}{L_0} \tag{3.31}$$

$$\Delta L = \frac{F \times L_0}{E \times A} \tag{3.32}$$

where *ΔL* represents the deformation or change in length of the winding and L_0 is the original length of the disc winding. *E* is the Young's Modulus of

© COPYRIGHT UPM

material property that defines how much a material will deform under stress. *A* is the cross-sectional area of the winding.

3.5.3 Safety factor analysis

Based on the material proportional limit, it is possible to restrict the material tension to a safe level. In this case, it is common to use a safety factor. The Von-Mises yield criteria are used when deciding safety factors. The maximum von Mises stress, σ_{vm} for the HV winding can be calculated using Equation (3.33) [151].

$$\sigma_{vm} = \frac{1}{\sqrt{2}}\sqrt{(\sigma_r - \sigma_{\emptyset})^2 + (\sigma_{\emptyset} - \sigma_z)^2 + (\sigma_z - \sigma_r)^2 + 6{\tau_{r\emptyset}}^2 + 6{\tau_{zr}}^2 + 6{\tau_{\emptyset z}}^2} \quad (3.33)$$

where, σ_r, $\sigma_{\emptyset}, \sigma_z$ are the normal stress components and $\tau_{r\emptyset}, \tau_{\emptyset z}, \tau_{zr}$ are the shear stress component. The safety factor is the ratio between the yield strength of the winding material and the maximum von Mises stress achieved during the switching transient as given by Equation (3.34) [54].

$$SF = \frac{\sigma_{yield}}{\sigma_{vm}} \quad (3.34)$$

where SF is safety factor and σ_{yield} is the yield strength of the winding material. A safety factor greater than 1 indicates that the structure is considered safe and vice versa.

© COPYRIGHT UPM

3.6 Summary

The first section discusses the modelling of a disc winding for switching impulse transient analysis. This section involves a detailed representation of the disc winding geometry, material properties and electrical conditions to study the behaviour of the winding under switching impulse transients. Several simplifications are carried out to ensure the analysis is computationally efficient. The simplifications include only 8 proportions of HV disc winding from 96 discs with the omission of the core and insulating oil. The verification method of the disc winding model is also presented based on a comparison of the simulated and calculated initial voltage distribution.

The second section discusses the procedure to obtain the electromagnetic forces of a disc-type winding during the switching transient based on 2 methods known as analytical and numerical methods. The analytical method is performed based on the calculation from the formula derivation of force with respect to the winding geometrical design through the MATLAB platform. The numerical method is carried out based on simulation of the electric transient analysis through the Ansys Maxwell.

The third section described the process for the three-way coupling of electrical-thermal-structural analysis of the disc winding under switching transient conditions. The data transfers between electrical, thermal and structural simulations are specified. The material properties, boundary conditions, input load and output of the three domains are also specified.

© COPYRIGHT UPM

Lastly, the fourth section discussed the structural behaviours of the disc winding due to the thermal effect as a result of the recurrence of switching transients. It is performed through the winding plastic deformation analysis. There are 3 important factors that are considered for this analysis which are the characteristics of the winding deformations and displacement, stress-strain curve and safety factor assessment.

© COPYRIGHT UPM

CHAPTER 4

RESULTS AND DISCUSSION

4.1 Overview

This chapter is divided into 4 main sections. The first section shows the verification of the transformer disc winding model. The second section addresses the impact of the electromagnetic force of a disc winding due to switching impulses based on analytical and numerical methods. The following section discusses the interrelated switching impulse response in terms of electrical, thermal and mechanical properties through the electric-thermal-structural coupling analysis. The last section discusses the disc winding structural stability in response to the electromagnetic force and thermal effect induced by the recurrence switching impulse through the buckling analysis. This section includes the disc winding mechanical response assessment through stress-strain, load-displacement and safety factor analysis.

4.2 Disc winding model validation

The comparison between the calculated and simulated initial surge voltage distribution of the Standard Switching Impulse (SSI) voltage on the disc winding reveals a significant level of agreement as shown in Figure 4.1. Both distributions display similar trends, which indicates that the disc winding model adequately captures the essential aspects of its electrical behaviours.

© COPYRIGHT UPM

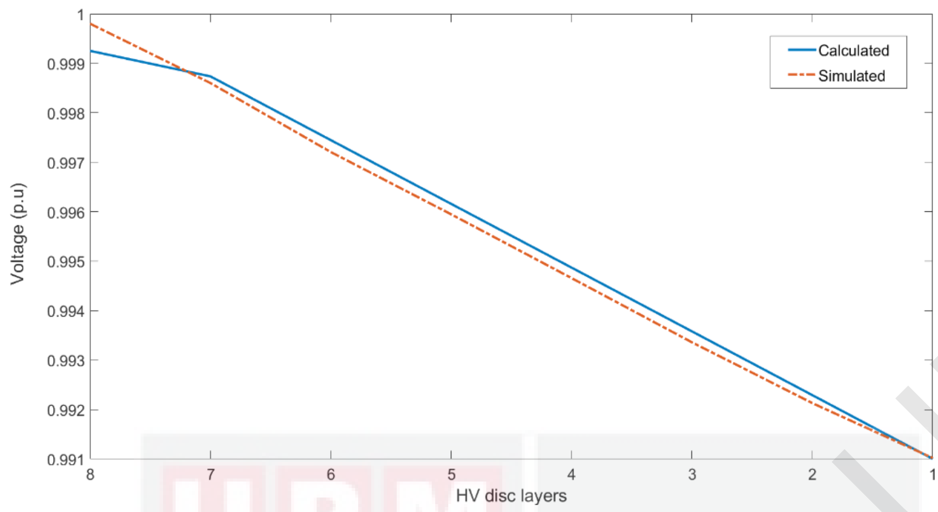

Figure 4.1: Calculated versus simulated initial surge voltage distributions on disc winding

The voltage drops between the disc layers of both calculated and initial surge voltage distributions are quite small and decrease from disc layers 8 to 1. This is because the continuous disc layer arrangement of disc winding used in this study can reduce the voltage drops. For the calculated initial surge voltage distribution, the voltage drops between disc layers 8 and 7 are unevenly distributed compared to for disc layers 7 to 1. This is due to the top disc layer effect which is similar to finding in [152]. For disc winding, the capacitance among the turns tends to increase towards the outer layers of the winding. This is because the outer disc layers are closer to the conductive structure, which is the tank as compared to the inner layers. This phenomenon is due to the presence of C_g between the HV winding's topmost disc layer 8 and the tank.

For the simulated initial surge voltage distribution, the voltage drops between each of the disc layers are not apparent due to the close variation of winding capacitance. This finding is consistent with the analysis in [153]. The voltage distribution coefficient, α between each disc layer is not equal to 0 with very small discrepancies. This indicates that the voltage does not distribute uniformly throughout the windings. Another reason is due to the assumptions and simplifications made during simulation that influence the voltage distribution.

The simulated initial voltage distribution relies on the Maxwell equations which take into account the electromagnetic interactions within the disc winding structure including current density, vector potential and conductor conductivity. The simulation considers practical aspects and parameters, such as the distance between discs, which enhances the relative permittivity and increases variation in inter-disc capacitances. The small distance between discs increases field intensity, enhance dielectric polarisation and increase relative permittivity. While the equations primarily represent current density, J_{rj} and vector potential, A_{rj}, the effect of distance between discs is inherently included through its influence on electric field intensity, charge distribution and capacitance variations, which impact the overall voltage distribution.

The calculation method uses a simplified approach based on the capacitive characteristic of the winding. It incorporates the height of the winding and layer distance from the neutral point. It assumes a uniform distribution of capacitance along the disc winding layers and neglects some of the complexities associated with the electromagnetic interactions within the winding. This approach neglects some detailed electromagnetic and non-linear effects in the dielectric materials that are considered in the simulation method.

© COPYRIGHT UPM

The Correlation Coefficient Factor (CCF) of the calculated and simulated initial surge voltage distribution is approximately 0.9995, which signifies a high level of positive correlation. The proposed disc winding model is validated and capable to represent the through-thickness properties of the transformer disc winding.

4.3 The impact of switching transient on the electromagnetic force of a disc-type winding.

4.3.1 The disc winding RLC parameters

In this study, the switching transient resonance is analysed once the switching impulse voltage is applied to the disc winding. The current required to charge the capacitive elements in the disc winding equivalent circuit is calculated to ensure no magnetising current is generated in the circuit model. The transformer is assumed to operate based on standard tapping conditions for all cases. The taps range from + 5 % to – 15 % in 8 equal steps of 2.5 % each on HV winding, 9 tap positions and tap no 3 will be the principal tap position. The RLC parameters for each disc layer are shown in Figure 4.2 and Table 4.1.

© COPYRIGHT UPM

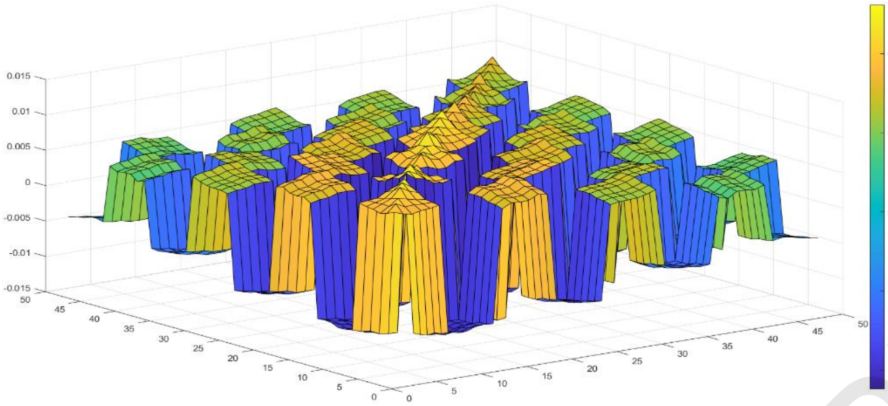

(a)

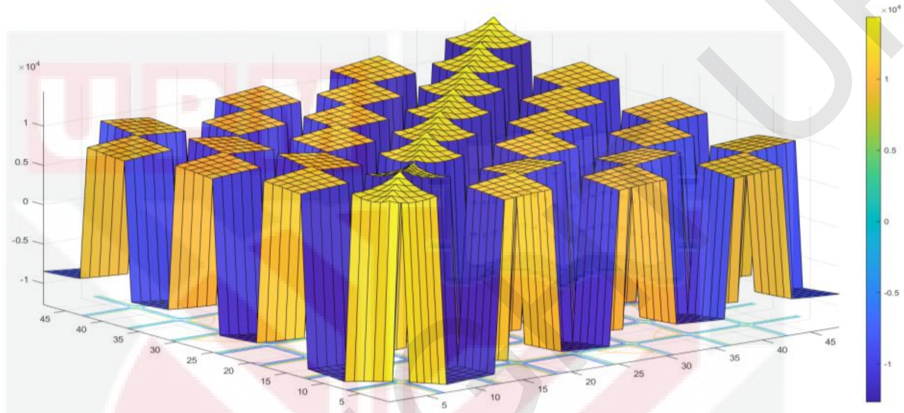

(b)

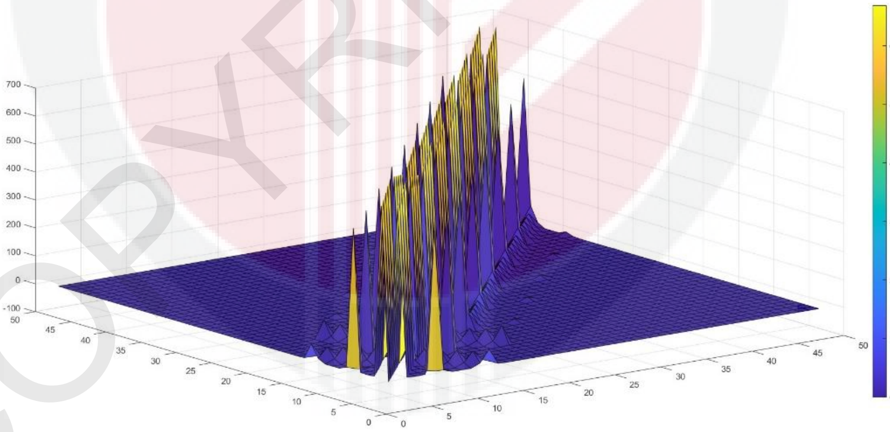

(c)

© COPYRIGHT UPM

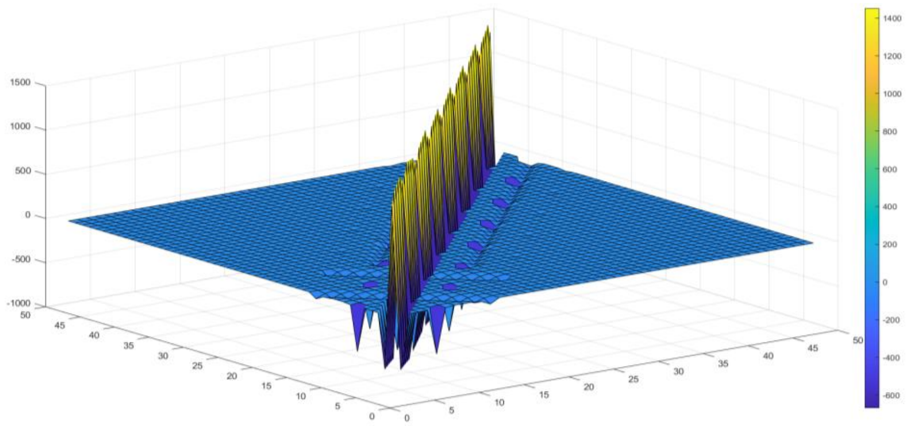

(d)

Figure 4.2: (a)R_s, (b)L_s, (c) C_s and (d) C_g matrix of HV disc winding

Table 4.1: RLC parameters of the 8 topmost HV disc winding

Disc	R_s (mΩ)	L_s (μH)	C_s (pF)	C_g (pF)
8	16.448	125.904	8.127	211.725
7	19.564	62.032	8.281	202.664
6	19.647	66.438	8.280	202.610
5	19.699	42.641	8.280	202.608
4	22.312	72.702	8.280	202.612
3	17.449	39.693	8.280	202.614
2	24.427	83.315	8.280	202.664
1	19.618	66.359	8.127	211.726

The total C_s in the full 96 disc winding is distributed along the entire winding height, forming a capacitive voltage divider that influences transient voltage distribution. In the 8 disc model, the total capacitance is lower than in the full winding, but the local capacitance effects remain similar because the distances between discs and insulation properties remain unchanged. The 8 disc model still captures these high voltage stress regions accurately. The full 96 disc winding has a more complex inductance matrix, affecting longitudinal resonant frequencies. The 8 disc model retains the primary localised resonance effects,

© COPYRIGHT UPM

ensuring accurate high-frequency transient response at the top disc winding section. The exclusion of lower discs results in minor shifts in overall resonance behaviour, but this does not significantly impact the accuracy of localised transient force analysis on the 8 disc winding.

4.3.2 Transient resonance due to the switching impulses

The transient resonance in the HV disc layers under the 165 kV of SSI and 108.9 kV of Non-Standard Switching Impulse (NSSI) can be seen in Figure 4.3 and Figure 4.4, respectively. The percentage deviations, % Δ of the switching transient resonances of the disc layers are presented in Figure 4.3 and Table 4.2. The V8top is the applied impulse voltages while the V8end, V7end, V6end, V5end, V4end and V3end are the measured resonance waveforms at the end of disc layers 8 to 3.

Figure 4.3 shows that the SSI waveform initially increases to 1.0 p.u. and it starts to oscillate at the tail time between 350 µs and 2500 µs, which indicates the presence of resonance. The resonance oscillations at the end of the disc layers have a lower peak and show signs of attenuation from the top to bottom disc layers, from V8end to V3end. This pattern suggests that the energy is gradually attenuated as it propagates to the bottom of the disc layers. The topmost disc layer voltage, V8end experiences the highest amplitude resonance oscillations because it is closest to the point of applied SSI voltage, V8top. The percentage deviations of resonance oscillations are between 13.14% and 0.41% as shown in Table 4.2. The percentage deviations of

© COPYRIGHT UPM

resonance oscillations decrease from V8end to V3end, which indicates a decrement in the resonance oscillations as it reaches the bottom of the disc layer.

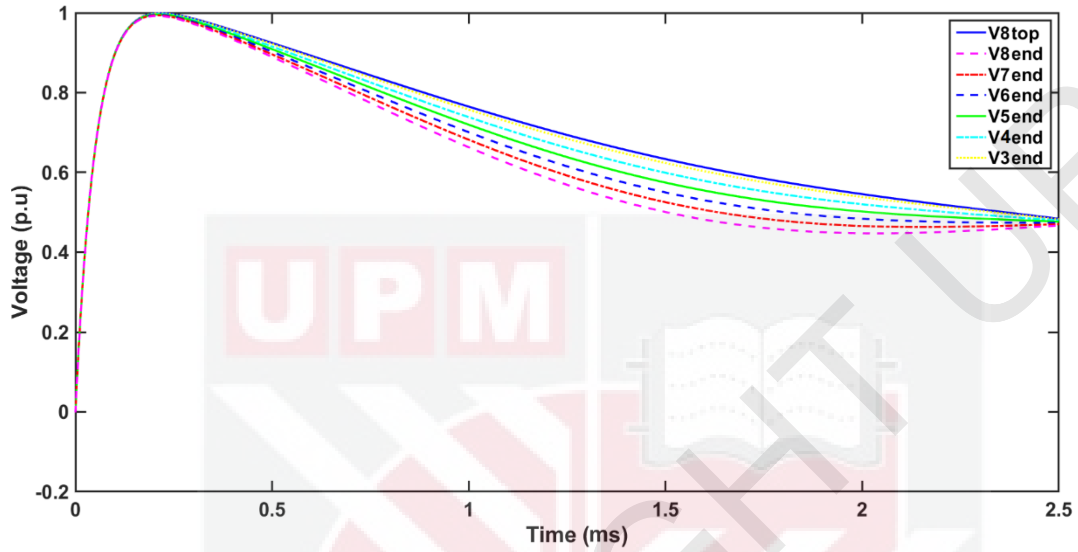

Figure 4.3: Transient resonance distribution under SSI voltage

Table 4.2: Percentage deviation of transient resonance under SSI voltage

Vend	8	7	6	5	4	3	2	1
% Δ	13.14	11.08	9.04	6.98	4.94	2.87	0.82	0.41

All disc layers exhibit initial switching transient resonance oscillations at the onset of the applied NSSI voltage between 0 and 1 ms as shown in Figure 4.4. The transient resonance of V8end shows significant oscillation as early as between 1 and 3 ms. The oscillations continued to amplify and reached its highest level between 3 and 7 ms. Disc layer 8 experiences high amplitudes and multiple cycles of oscillations due to its proximity to the point of applied NSSI voltage, V8top. The V7end and V6end also show strong resonance

© COPYRIGHT UPM

oscillations but are less intense than the resonance oscillations of V8end. The resonance oscillations of V5end and V4end show similar increment patterns but moderate and slightly damped. The V3end shows the lowest resonance oscillation.

There is a phase shift between the resonance oscillations of different disc layers. This shift indicates that the energy from the NSSI voltage propagates through the disc layers with a delay, which affects its resonance oscillations. The damp effect is observed among all disc layers with a decrement of resonance oscillations over time. The NSSI voltage causes disc layers to experience complex resonance oscillations, with the most substantial response occur once the NSSI voltage reaches its peaks which is between 3 and 7 ms. The percentage deviations of resonance oscillations are between 107.26 % and 91.46 % as shown in Table 4.3. Similar to the SSI voltage, the percentage deviations of resonance oscillations for NSSI voltage show a decrement trend from Vend8 to Vend3, which indicates a reduction in the resonance oscillations.

© COPYRIGHT UPM

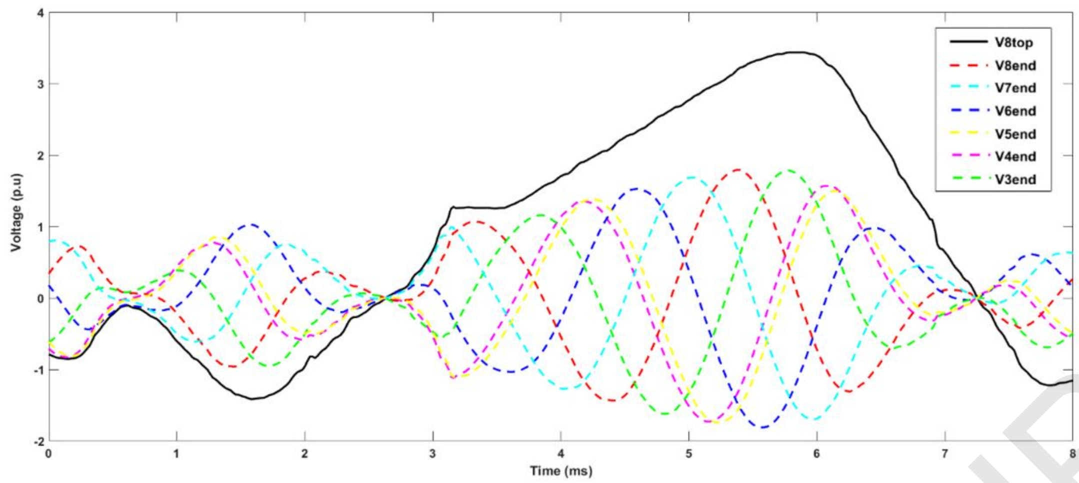

Figure 4.4: Transient resonance distribution under NSSI voltage.

Table 4.3: Percentage deviation of transient resonance under NSSI voltage

Vend	8	7	6	5	4	3	2	1
% ∆	107.26	107.01	106.01	99.13	97.21	97.01	91.47	91.26

The switching transient resonances under SSI voltage oscillate more uniformly as compared to under NSSI voltage, which exhibits more pronounced with high amplitudes and complex oscillations. This difference can be attributed to the characteristics of the impulse waveforms. The SSI voltage has a gradual voltage rise that minimises the abrupt charge redistributions within the winding. Its smooth and gradual transition towards decay phase allows the winding to naturally dissipate the transient energy. This prevents significant voltage differentials between adjacent disc layers which ensures uniform and consistent resonance oscillations. NSSI voltage exhibits a more irregular waveform with steeper rise and fall times. The abrupt waveform transitions cause stronger interactions between discs, amplify local resonances and complex oscillation patterns. As the transient propagates through the winding,

© COPYRIGHT UPM

variations in inter-disc capacitance and inductance further modulate the oscillation amplitudes which results in irregular and high amplitude resonances.

It is also observed that the resonance oscillations can be influenced by the position of the disc layers, with pronounced resonance oscillations at the top disc layers. This finding is consistent with [154] that highlights the resonance effect is most pronounced at the beginning of the impulse injection. This is when the impulse voltage first hits the transformer winding and is the most susceptible to resonance oscillations due to the initial surge of energy.

4.3.3 Electromagnetic forces based on analytical method

The axial and radial forces under SSI and NSSI voltages computed based on the analytical method via Equation 3.5 and Equation 3.6 in Chapter 3 can be seen in Figure 4.5 and Figure 4.6, respectively. A similar pattern of electromagnetic force distributions is found based on the same calculated parameter of the HV disc winding with different magnitudes. The axial and radial forces vary across the HV disc layers. Both axial and radial forces under SSI and NSSI voltages show initial decrement trends as the disc layer decreases to the middle section. Slight increments of axial and radial forces are found as the disc layer further decreases to the bottom disc layers.

© COPYRIGHT UPM

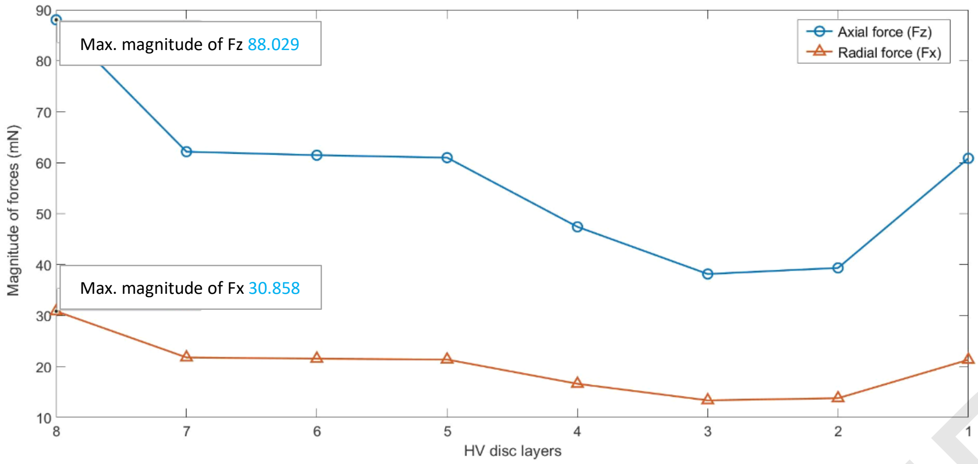

Figure 4.5: Calculated axial and radial force distribution under SSI voltage

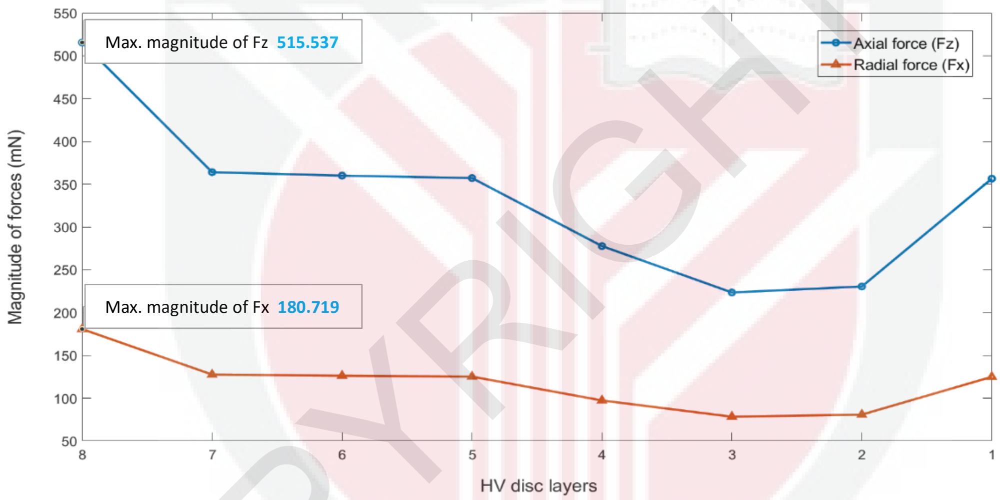

Figure 4.6: Calculated axial and radial force distribution under NSSI voltage

Generally, the axial force exerted on the disc winding under SSI and NSSI voltages is higher than the radial force. This is expected due to the geometrical design of the disc winding. Equation 3.6 in Chapter 3 shows that axial force is associated with the total length of the disc winding and radial disc winding arrangement that affects the effective length of the radial flux path. A significant radial flux component can be presented in a disc winding with a radial

© COPYRIGHT UPM

component, particularly towards its ends. The radial flux can lead to the increment of the axial force as found in [107].

In addition, the electromagnetic forces pattern exerted on each disc layer is estimated to be almost similar to the impulse voltage distribution slope, where the highest impulse voltage is exerted on the topmost disc layer 8. Therefore, the topmost disc layer is also anticipated to experience the highest electromagnetic force. Electromagnetic forces on other disc layers should be linearly distributed at lower magnitudes than the topmost disc layer. However, there are reductions in the magnitudes of forces for disc layers 4, 3 and 2 due to the RLC parameters in the ampere-turn component of the disc layers. The RLC parameters modulate the current and voltage distributions during the switching transient which results in the non-linear distribution of electromagnetic forces across the disc layers similar to the discussion in [155].

It is observed that NSSI voltage induces higher axial and radial forces compared to SSI voltage despite lower impulse voltage magnitude. A faster rise time of the NSSI results in a higher rate of voltage change, which leads to a higher induced current flow in the winding. Mathematically, the induced voltage in a transformer winding is given by $V = L(dI/dt)$ where a steep voltage changes results in a high rate of current change that leads to a higher peak current as inductances remain constant. This, in turn, increases the ampere-turns (NI) and consequently results in high electromagnetic forces. This finding aligns with the results presented in [156] which also demonstrates

© COPYRIGHT UPM

that faster impulse rise times and longer durations contribute to increased electromagnetic forces.

4.3.4 Electromagnetic forces distribution based on numerical method

The axial and radial components of the electromagnetic forces under SSI and NSSI voltages based on the numerical method through electric transient analysis are presented in the time domain as seen in Figure 4.7 and Figure 4.8. It is found that the magnitude of axial force under SSI voltage is higher and displays higher increments as compared to the radial force as shown in Figure 4.7. The radial force shows a gradual decrement pattern whereby the amplitude reaches -2.2 mN at the end of the simulation time. The negatively directed force toward the HV winding indicates that it is an inwardly compressive force. The radial force remains relatively low and constant compared to the axial force. The increment of axial force is quite apparent whereby the maximum amplitude reaches up to 35 mN at the end of simulation time. The exponential increment indicates a substantial build-up of axial force under the SSI voltage.

© COPYRIGHT UPM

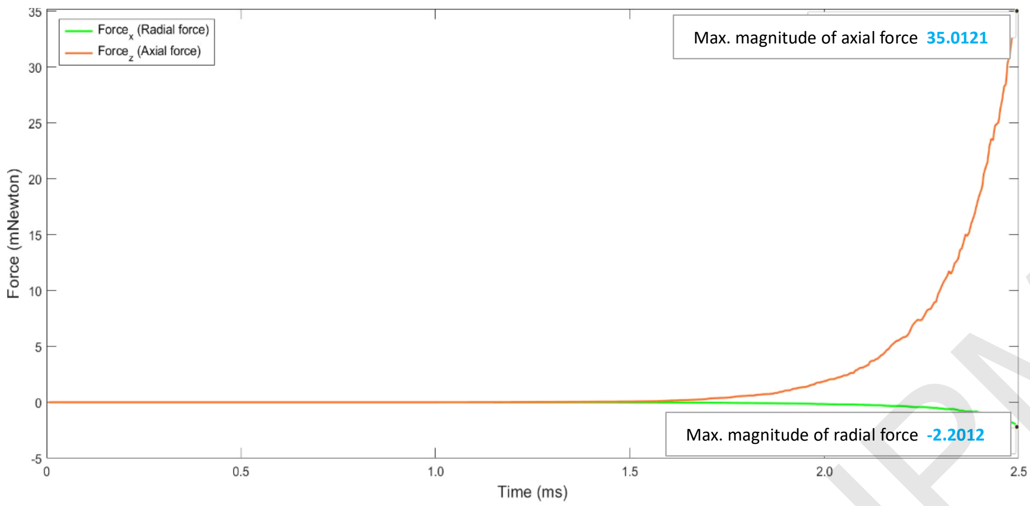

Figure 4.7: The radial and axial force distribution based on FEM under SSI voltage

The radial force experienced by the disc winding under NSSI voltage gradually increases over time, reaching around 30 mN at the end of the simulation time as shown in Figure 4.8. The axial force exhibits a complex pattern as it initially decreases before exponentially increases after 4 ms. Initially, the axial force amplitude decreases close to -40 mN and subsequently increases to approximately 207 mN at the end of the 8 ms. Similar to axial force under SSI voltage, NSSI voltage causes a substantial build-up of axial force. The radial force remains significantly lower in magnitude than the axial force till the end of the simulation time.

© COPYRIGHT UPM

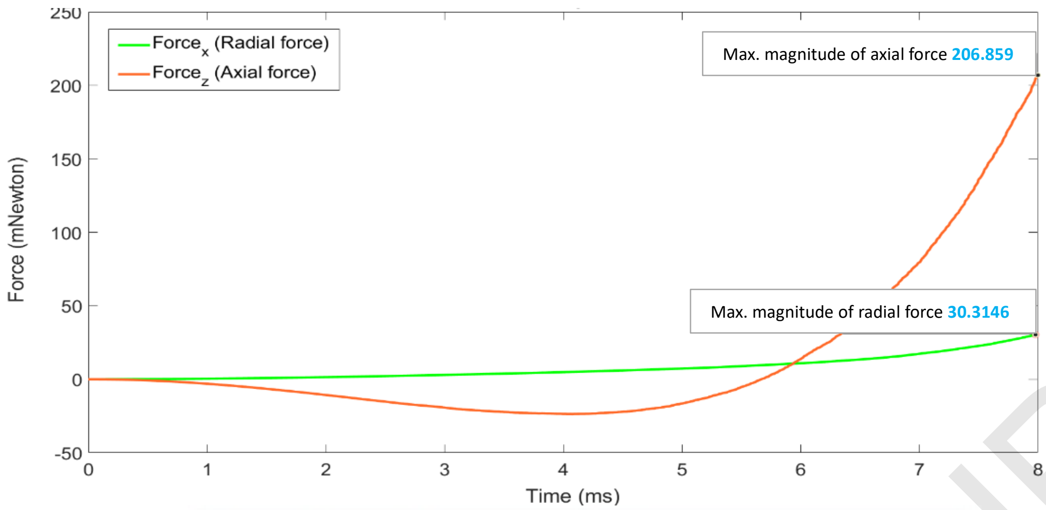

Figure 4.8: The radial and axial force distribution based on FEM under NSSI voltage

The trends of radial and axial forces under NSSI voltage are more complex and exhibit a greater range of magnitudes as compared to those under SSI voltage. The high magnitude and complex trend of forces can lead to severe disc winding structural conditions as it involves high mechanical stresses. The current finding is in line with the previous findings in [89], [157] where the electromagnetic forces of a disc-type transformer winding are likely to oscillate in the axial direction compared to the radial direction.

4.3.5 Structural deformations

In this section, the structural deformations due to SSI and NSSI voltages are classified into 2 modes which are directional and total deformations. Directional deformation refers to the deformation of the disc winding structure in specific defined directions known as the *x*-, *y*- and *z*-directions. These defined directions are correlated to the vector directions of the expressed electromagnetic forces. The total deformation is the vector sum of all the

© COPYRIGHT UPM

directional deformations. It should be noted that the forces that are generated from 1 cycle of injected switching impulse would not cause the winding to deform/displace. In this study, the scale of structural deformations is increased to analyse the possible deformation and displacement on the disc winding.

4.3.5.1 Directional Deformations

The variations of winding structural behaviours along the *x*-, *y*- and *z*-directions under 1 cycle of SSI and NSSI voltages are observed in 3 structural deformation scale factors known as true scale, 0.5x auto and auto-scale. The true scale displays the exact visual representation of structural deformation proportional to the actual calculated deformation values. The 0.5x auto-scale shows structural deformation multiplied by a factor of 0.5 times the auto-scale. Auto-scale is computed using the ratio of the maximum structural deformation to the size of the structure. It displays the most significant deformation/displacement of the disc winding model under the SSI and NSSI voltages. The average *x*-, *y*- and *z*- directional deformations are concentrated at $x = 0$, $y = 0$ and $z = 0$ plane [107]. The directional deformations due to the SSI and NSSI voltages are shown with the element triads to show the directions of the deformation moments, which can be seen in Figure 4.9 and Figure 4.10.

The *x*- and *y*- directional deformations are shown together since it represents the radial deformations. The *z*-directional deformation, which is orthogonal to the *x*- and *y*- planes represents the axial deformation and is shown separately.

© COPYRIGHT UPM

The minimum and maximum deformation values indicate how much each part of the disc winding deforms under the SSI and NSSI voltages. The increment of different deformation scale factors leads to the increment of the deformation values. The deformation patterns for the *x*-, *y*- and *z*- directions are supported by the details of directional deformations shown in Table 4.4 and Table 4.5.

Table 4.4: Directional deformations of disc winding under SSI voltage

Scale factor	Directional deformation	Minimum (mm)	Maximum (mm)	Average (mm)	Minimum Occurs On	Maximum Occurs On
True scale	*x*	-6.91×10^{-10}	1.71×10^{-9}	5.03×10^{-10}	Conductor 1 (Disc 5)	Conductor 1 (Disc 7)
	y	-1.89×10^{-10}	2.59×10^{-10}	-2.50×10^{-9}	Conductor 6 (Disc 8)	Conductor 1 (Disc 5)
	z	-4.88×10^{-9}	3.06×10^{-9}	1.61×10^{-9}	Conductor 1 (Disc 6)	Conductor 2 (Disc 8)
0.5x Auto-scale	*x*	-13.82×10^{-10}	3.42×10^{-9}	10.06×10^{-10}	Conductor 1 (Disc 5)	Conductor 1 (Disc 7)
	y	-3.78×10^{-10}	5.18×10^{-10}	-5.00×10^{-9}	Conductor 6 (Disc 8)	Conductor 1 (Disc 5)
	z	-9.76×10^{-9}	6.12×10^{-9}	3.22×10^{-9}	Conductor 1 (Disc 6)	Conductor 2 (Disc 8)
Auto-scale	x	-27.64×10^{-10}	13.68×10^{-9}	20.12×10^{-10}	Conductor 1 (Disc 5)	Conductor 1 (Disc 7)
	y	-7.56×10^{-10}	24.48×10^{-9}	6.44×10^{-9}	Conductor 6 (Disc 8)	Conductor 1 (Disc 5)
	z	-39.04×10^{-9}	20.72×10^{-10}	-40.24×10^{-10}	Conductor 1 (Disc 6)	Conductor 2 (Disc 8)

The second highest deformation under SSI voltage occurs at the outermost disc winding or circumference of the disc winding, which is in the *x*-direction with a peak magnitude of 1.71×10^{-9} mm based on the true scale. The *x*-directional deformation acts perpendicularly to the axis of the disc winding and causes hoop tension. This hoop tension refers to the tensile stress that occurs

© COPYRIGHT UPM

perpendicularly to the disc winding axis. This stress leads to the stretch of the copper conductors along the circumference of the disc winding, which results in changes in its dimension and shape. The copper conductors between the fixed supports bend outwardly as seen in Figure 4.9. This condition occurs since the structure of fixed support has a higher stiffness than the copper conductors. On the other hand, the *y*-directional deformation is smaller in magnitude as compared to the *x* and *z*-directional deformations with a peak magnitude of 2.59$\times 10^{-10}$ mm based on true scale and results in insignificant structural deformation. These findings match the previous studies in [158], [159] that found positive forces acted horizontally to cause hoop tension.

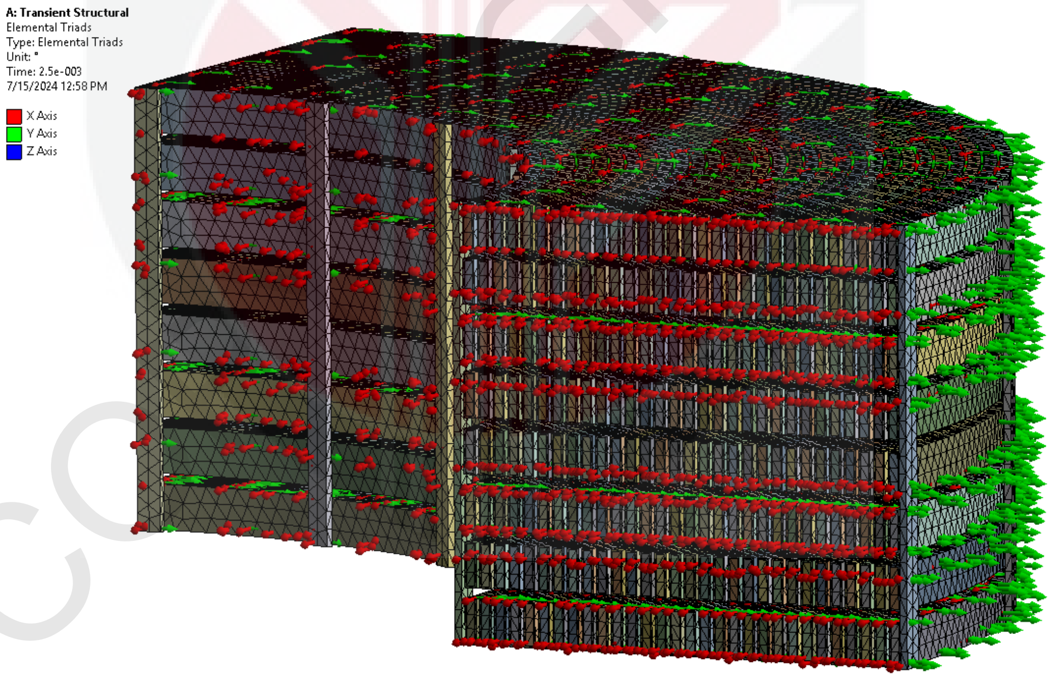

(a)

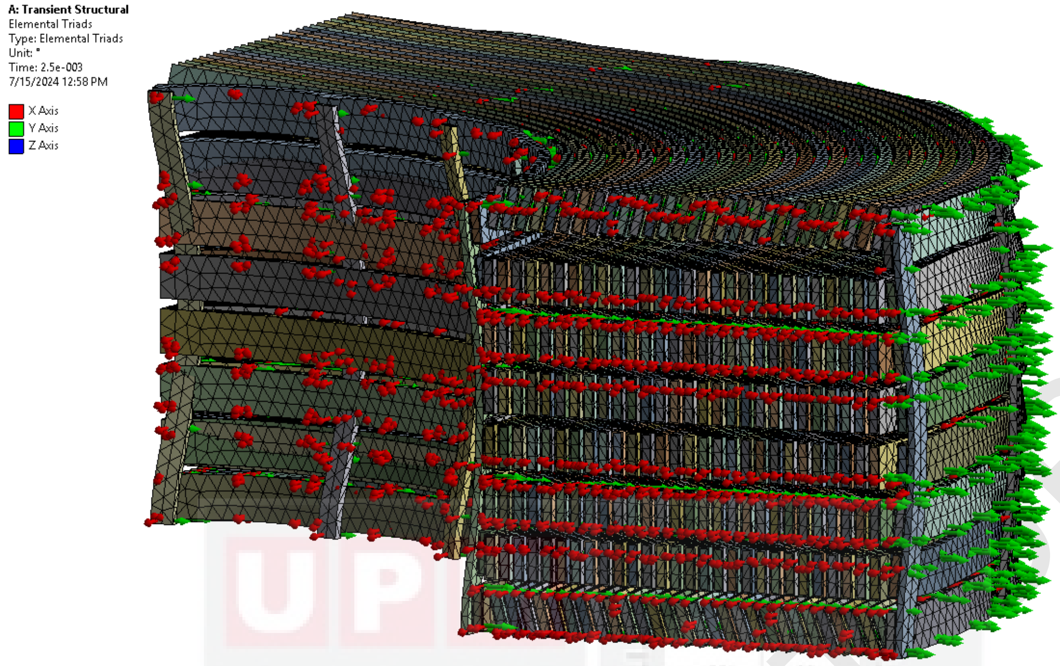

(b)

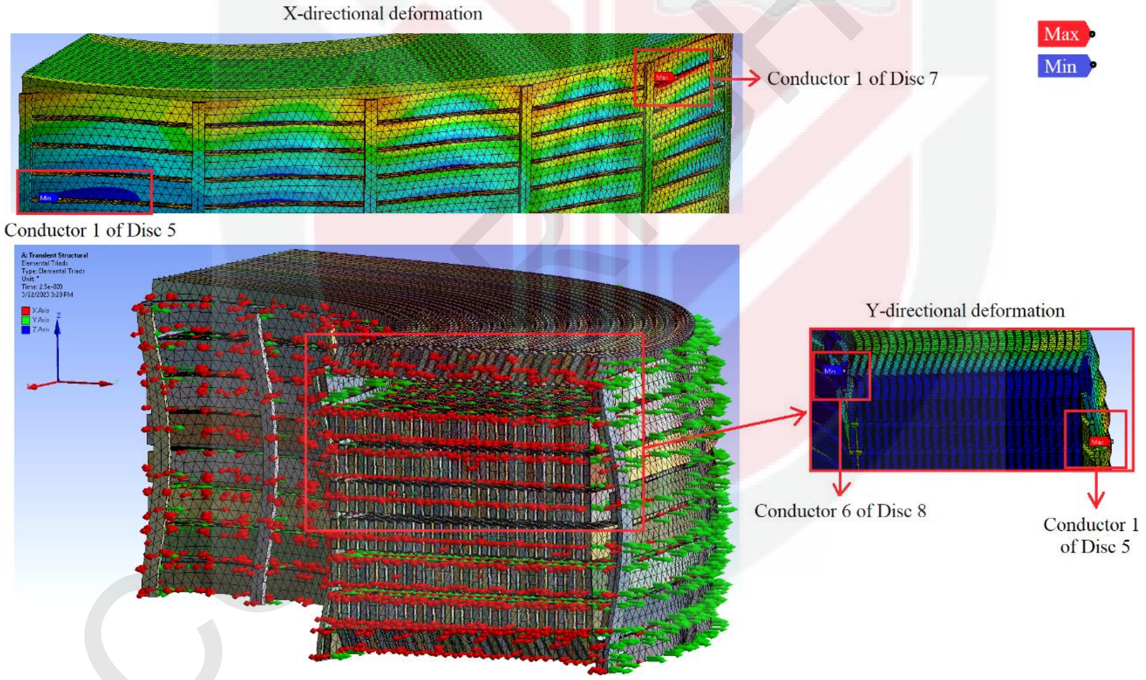

(c)

Figure 4.9: The *x*- and *y*- directional deformations of disc winding due to SSI voltage with (a) true scale, (b) 0.5x auto-scale and (c) auto-scale

The highest directional deformation of the disc winding under the SSI voltage occurs in the *z*-direction, which is along its axial height. The highest *z*-directional deformation is located at the topmost disc layer with a peak

© COPYRIGHT UPM

magnitude of 3.06×10^{-9} mm based on the true scale deformation factor. The axial displacements are apparent at the top and bottom layers of the disc winding as seen in Figure 4.10. The disc winding experiences axial displacement and tilting of copper conductors. The positive *z*-directional deformation causes the bottom and top disc layers to displace slightly upward from its original position. In addition, it is observed that the copper conductors at both disc layers tilt to the right and left directions at a small angle ranging between 5° and 10°. In this case, the fixed support tends to bend or not evenly align due to the deformations. This condition causes the axial force to be imposed unevenly on the disc winding, which leads to different degrees of tilting in different disc layers.

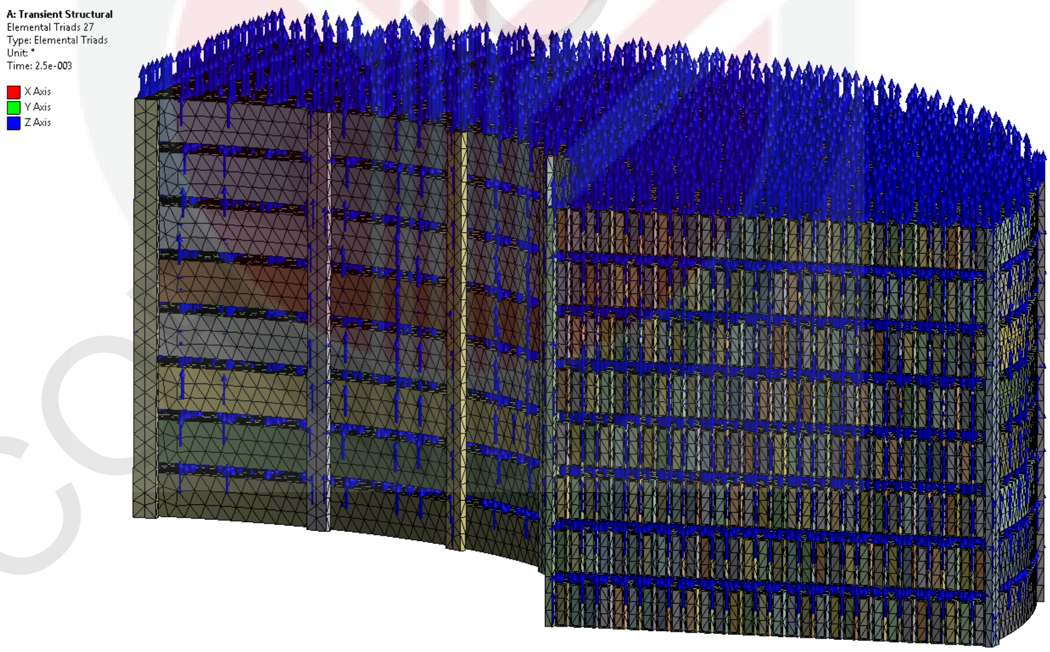

(a)

© COPYRIGHT UPM

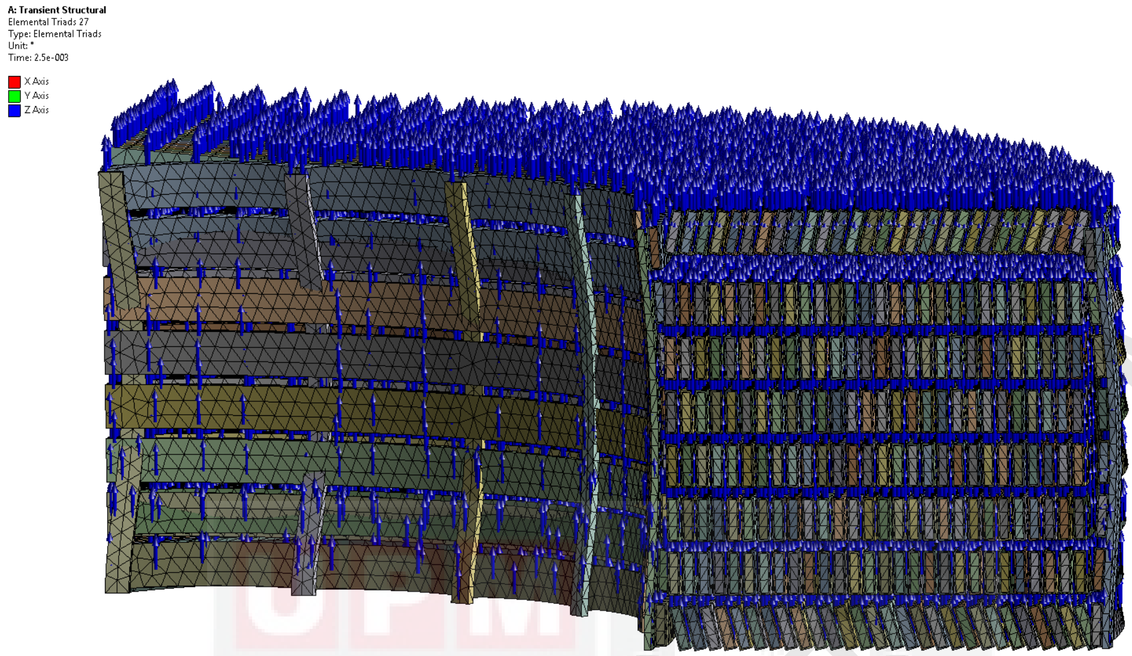

(b)

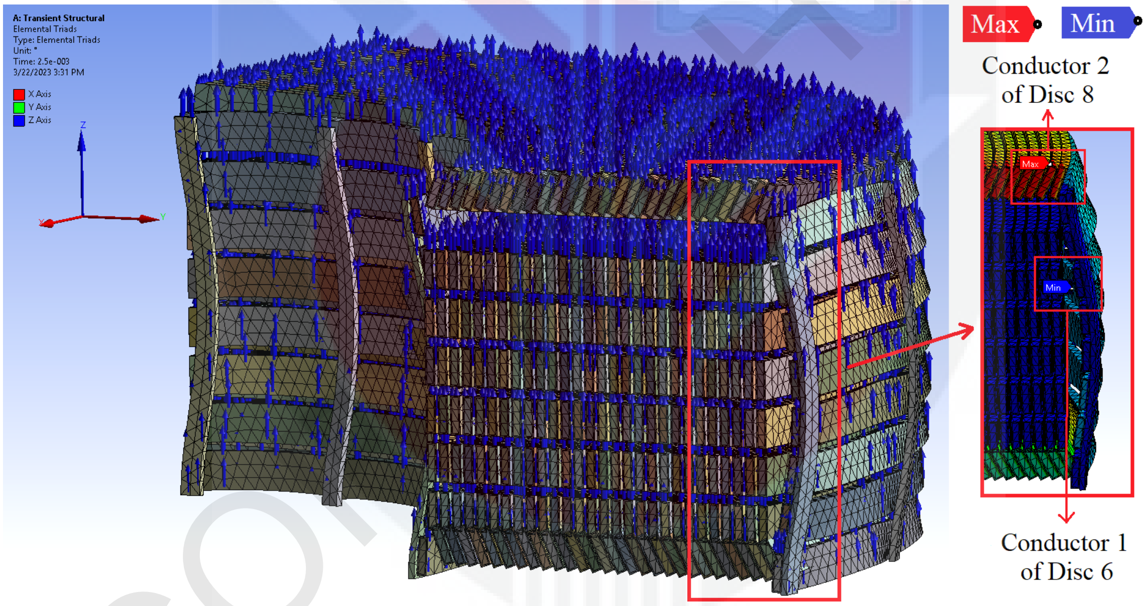

(c)

Figure 4.10: The *z*-directional deformations of disc winding due to SSI voltage with (a) true scale, (b) 0.5x auto-scale and (c) auto-scale

Table 4.5: Directional deformations of disc winding under NSSI voltage

Scale factor	Directional deformation	Minimum (mm)	Maximum (mm)	Average (mm)	Minimum Occurs On	Maximum Occurs On
True scale	*x*	-1.24×10^{-5}	2.97×10^{-6}	-7.22×10^{-7}	Conductor 3 (Disc 4)	Conductor 5 (Disc 8)
	y	-1.22×10^{-6}	3.51×10^{-5}	3.12×10^{-6}	Conductor 3 (Disc 8)	Conductor 4 (Disc 5)
	z	-2.56×10^{-6}	3.81×10^{-5}	6.11×10^{-6}	Conductor 3 (Disc 8)	Conductor 1 (Disc 1)
0.5x Auto-scale	*x*	-2.48×10^{-4}	5.94×10^{-5}	-14.4×10^{-6}	Conductor 3 (Disc 4)	Conductor 5 (Disc 8)
	y	-2.44×10^{-5}	7.02×10^{-4}	6.24×10^{-5}	Conductor 3 (Disc 8)	Conductor 4 (Disc 5)
	z	-5.12×10^{-5}	7.62×10^{-4}	12.2×10^{-5}	Conductor 3 (Disc 8)	Conductor 1 (Disc 1)
Auto-scale	x	-6.20×10^{-2}	14.9×10^{-3}	-36.1×10^{-4}	Conductor 3 (Disc 4)	Conductor 5 (Disc 8)
	y	-6.11×10^{-3}	17.6×10^{-2}	15.6×10^{-3}	Conductor 3 (Disc 8)	Conductor 4 (Disc 5)
	z	-12.8×10^{-3}	19.1×10^{-2}	30.6×10^{-3}	Conductor 3 (Disc 8)	Conductor 1 (Disc 1)

The radial deformation under the NSSI voltage is similar to that under the SSI voltage whereby the highest deformation occurs at the outermost disc winding or circumference of the winding. However, the *y*-directional deformation is higher than the *x*-directional deformation with a peak magnitude of 3.51×10^{-5} mm based on the true scale. The *y*-directional deformation acts perpendicularly to the axis of the disc winding and causes hoop tension as seen in Figure 4.11. The *x*-directional deformation magnitude is smaller than the *y* and *z*-directional deformation magnitudes with a peak magnitude of 2.97×10^{-6} mm, which is considered as insignificant structural deformation.

© COPYRIGHT UPM

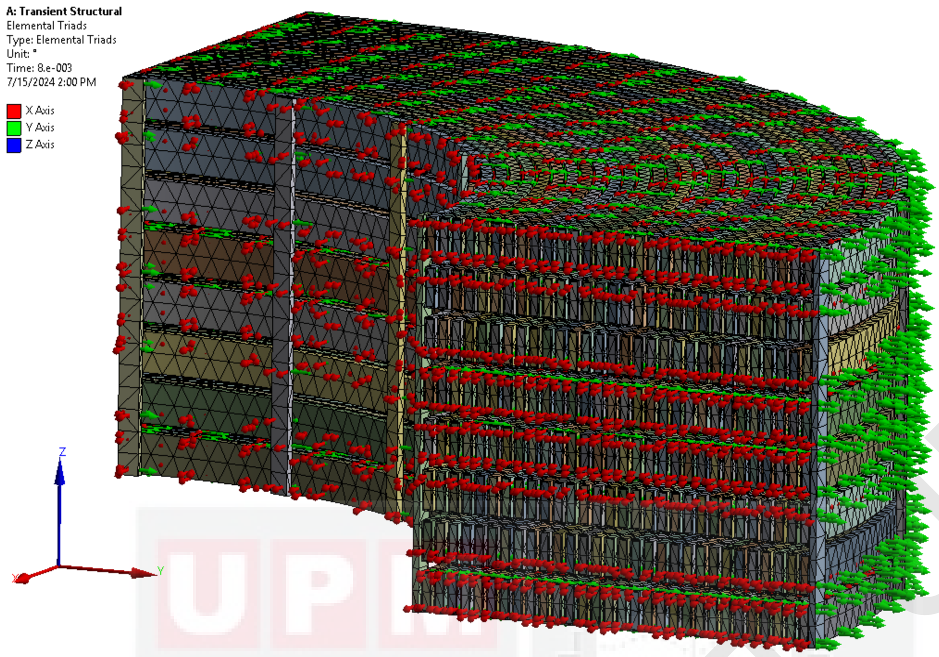
A: Transient Structural
Elemental Triads
Type: Elemental Triads
Unit: *
Time: 8.e-003
7/15/2024 2:00 PM
X Axis
Y Axis
Z Axis

(a)

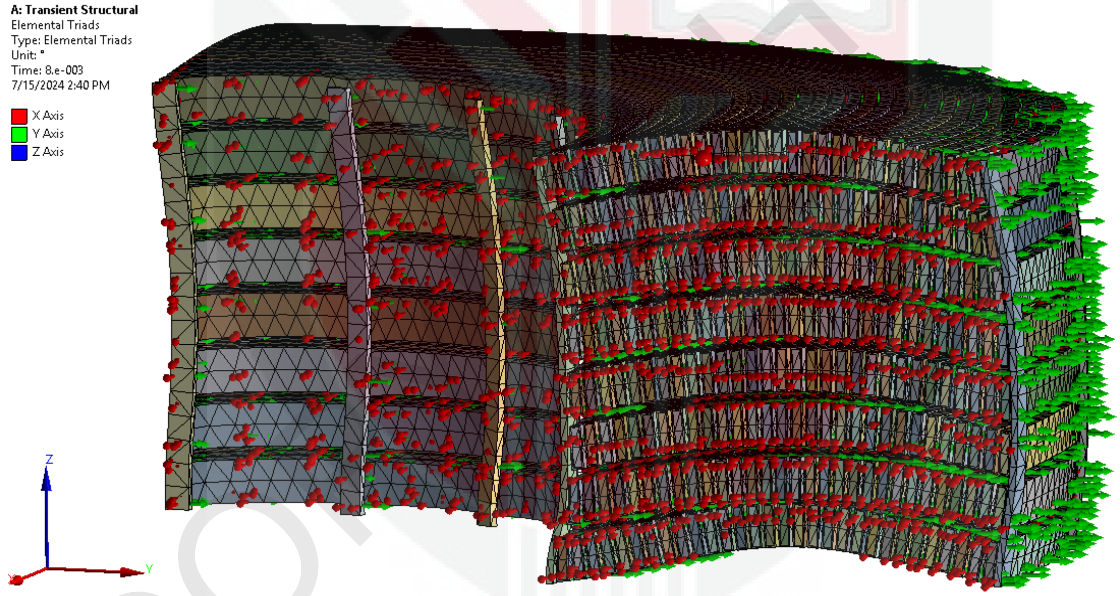
A: Transient Structural
Elemental Triads
Type: Elemental Triads
Unit: *
Time: 8.e-003
7/15/2024 2:40 PM
X Axis
Y Axis
Z Axis

(b)

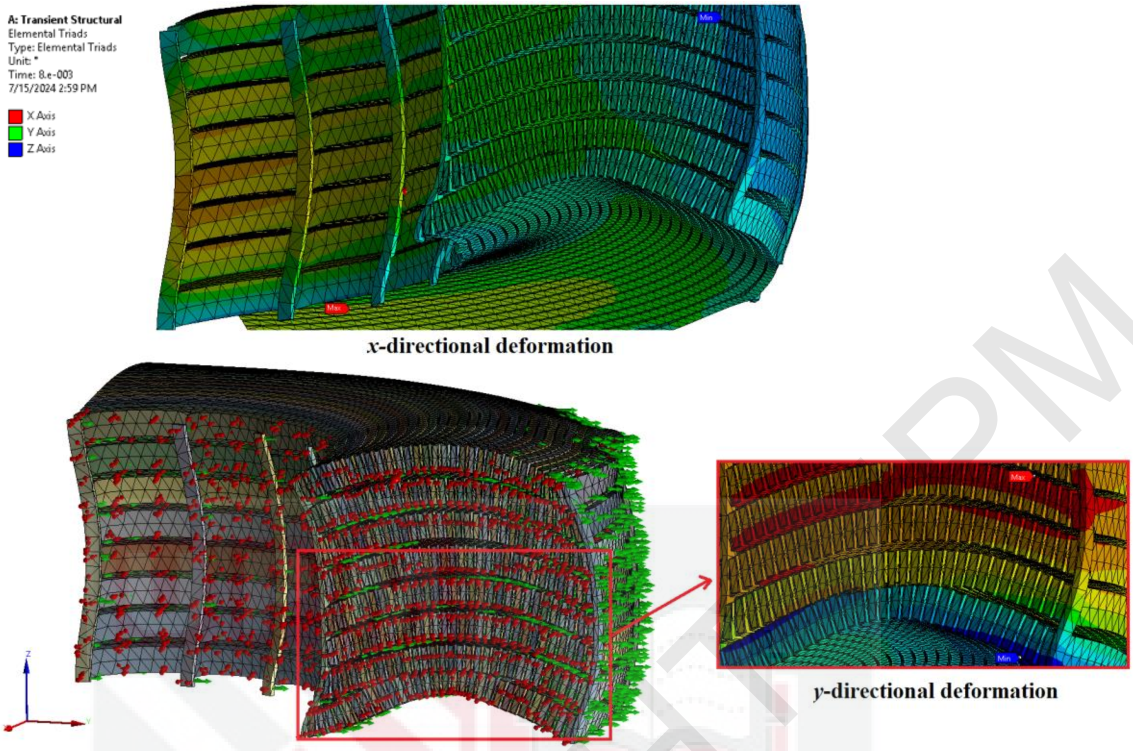

(c)

Figure 4.11: The *x*- and *y*- directional deformations of disc winding due to NSSI voltage with (a) true scale, (b) 0.5x auto-scale and (c) auto-scale

The highest directional deformation of the disc winding due to the NSSI voltage also occurs in the *z*-direction. It is located at the topmost disc layer and outer circumference of the disc winding with a peak magnitude of 3.81×10^{-5} mm based on the auto-scale deformation factor. Similar to under the SSI voltage, the axial displacements are apparent at the top and bottom layers of the disc winding as seen in Figure 4.12. However, under the NSSI voltage, the copper conductors experience more significant axial displacement and tilting as compared to when under SSI voltage. All copper conductors of all disc layers were displaced and tilted at different degrees as shown in Figure 4.12 (c).

© COPYRIGHT UPM

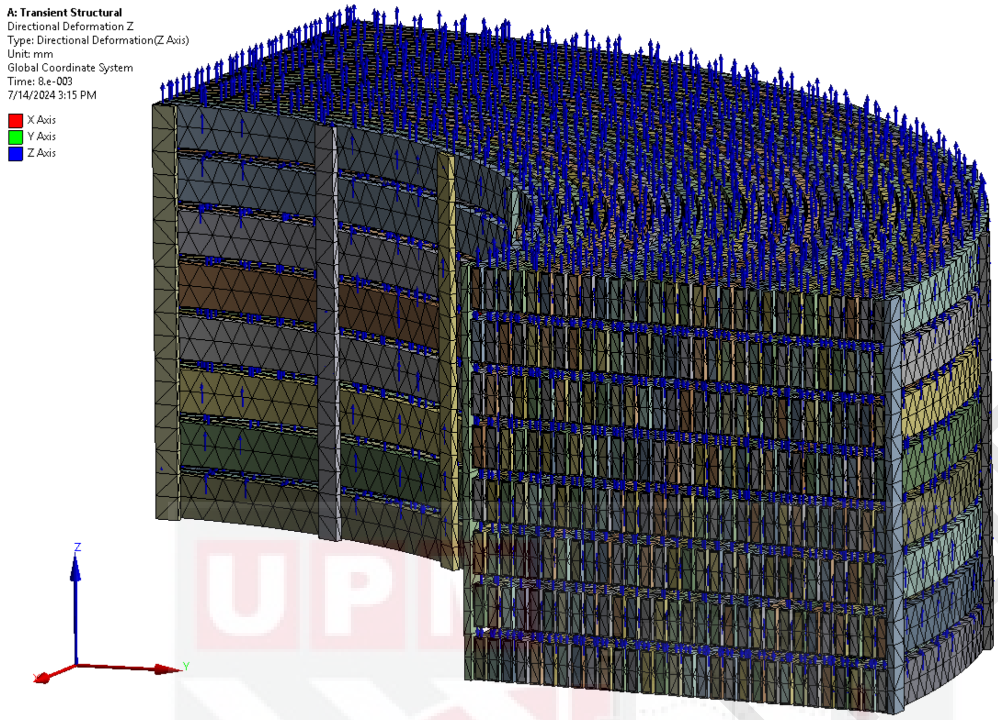

A: Transient Structural
Directional Deformation Z
Type: Directional Deformation(Z Axis)
Unit: mm
Global Coordinate System
Time: 8.e-003
7/14/2024 3:15 PM
X Axis
Y Axis
Z Axis
Z
Y

(a)

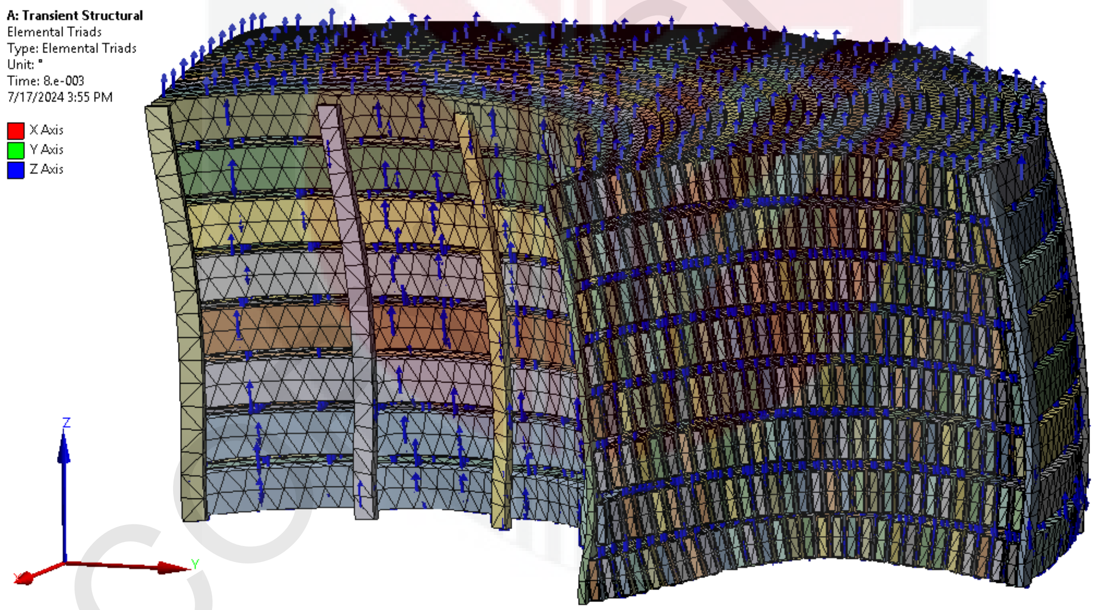

A: Transient Structural
Elemental Triads
Type: Elemental Triads
Unit: °
Time: 8.e-003
7/17/2024 3:55 PM
X Axis
Y Axis
Z Axis
Z
Y

(b)

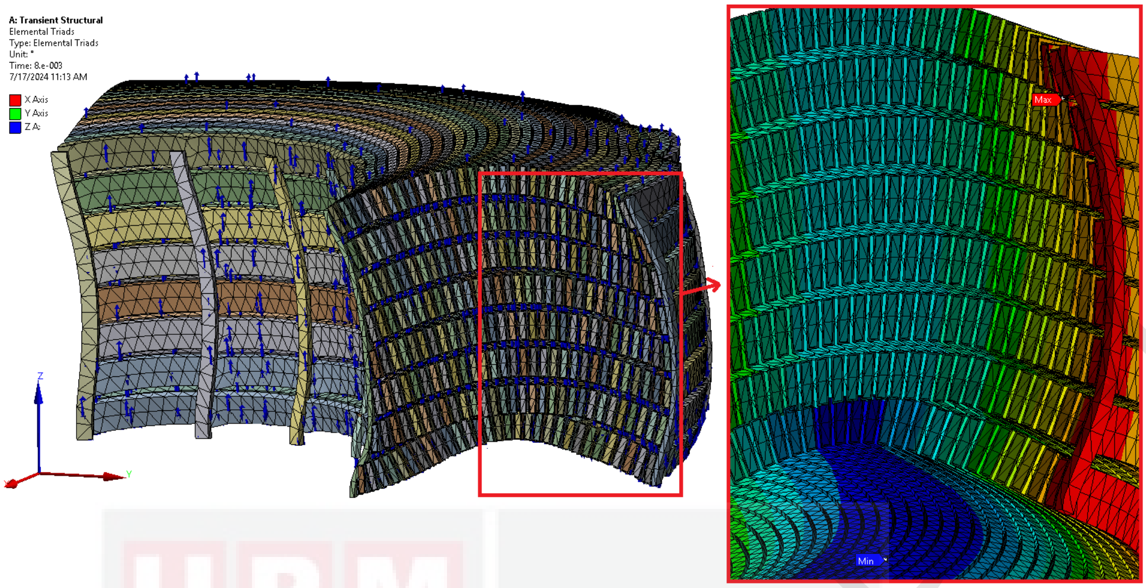

(c)

Figure 4.12: The *z*-directional deformations of disc winding due to NSSI voltage with (a) true scale, (b) 0.5x auto-scale and (c) auto-scale

The deformations and displacements that are caused by the SSI voltage are localised at the outermost disc layers in both axial and radial directions. The rest of the inner disc layers show relatively minimal deformation. The NSSI voltage causes widespread deformations and displacements throughout the entire disc winding structure. These conditions indicate global structural deformations as the stresses are distributed throughout the disc winding. This widespread deformation and displacement indicate that the entire disc winding is subjected to forces that compromise its overall stability.

4.3.5.2 Total Deformation

The total deformations show the total structural behaviours of the disc winding under 1 cycle of SSI and NSSI voltages with true scale, 0.5x auto-scale and auto-scale deformation scale factor are shown in Figure 4.13 and Figure 4.14.

© COPYRIGHT UPM

The total deformations are supported with the details of the total deformations as shown in Table 4.6 and Table 4.7.

The total deformation of disc winding under SSI voltage shows that the maximum deformation occurs on the copper conductor at the topmost disc layer, with a peak magnitude of 5.13×10^{-9} mm based on the true scale deformation factor. The minimum deformation occurs at the fixed supports, with 0 mm. The top view shows that radial deformation is significant at the circumferential, especially near the disc winding edges. The side view shows that axial displacement is significant at the top and bottom of the disc layers with different levels of displacement. Both top and side views show that the copper conductors at the outer circumference bent radially outward, while copper conductors in the inner disc winding remain stable with low deformation.

Table 4.6: The total deformation of disc winding under SSI voltage

Scale factor	Minimum (mm)	Maximum (mm)	Average (mm)	Minimum Occurs On	Maximum Occurs On
True scale	0	5.13×10^{-9}	3.29×10^{-9}	Fixed support 1	Conductor 2 (Disc 8)
0.5x Auto-scale	0	10.26×10^{-9}	6.58×10^{-9}	Fixed support 1	Conductor 2 (Disc 8)
Auto-scale	0	20.52×10^{-9}	13.16×10^{-9}	Fixed support 1	Conductor 2 (Disc 8)

© COPYRIGHT UPM

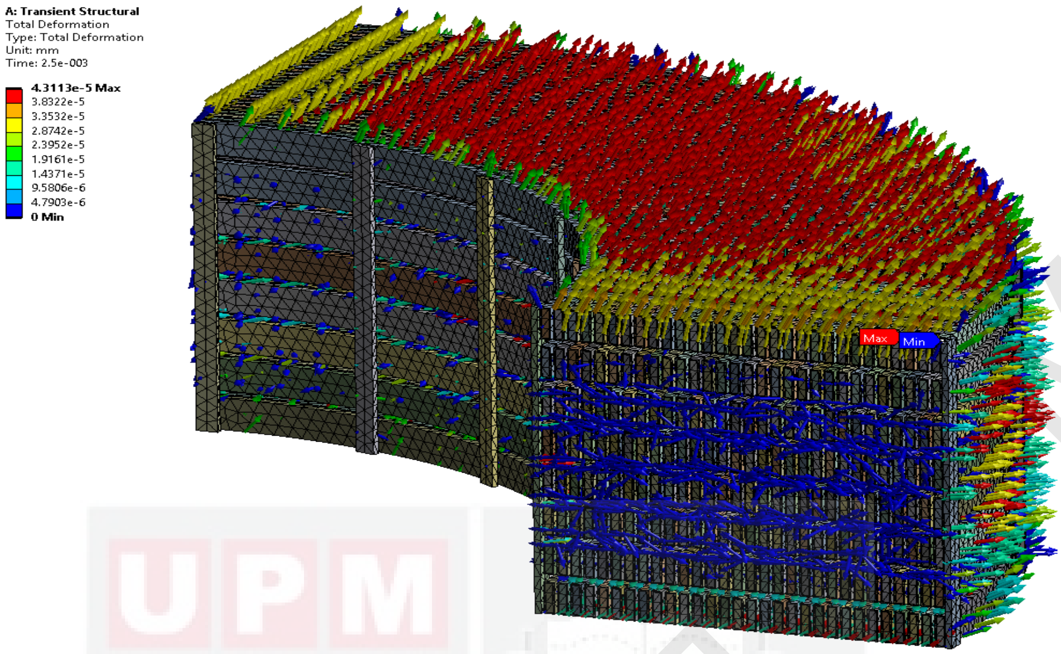
A: Transient Structural
Total Deformation
Type: Total Deformation
Unit: mm
Time: 2.5e-003
4.3113e-5 Max
3.8322e-5
3.3532e-5
2.8742e-5
2.3952e-5
1.9161e-5
1.4371e-5
9.5806e-6
4.7903e-6
0 Min
Max
Min

(a)

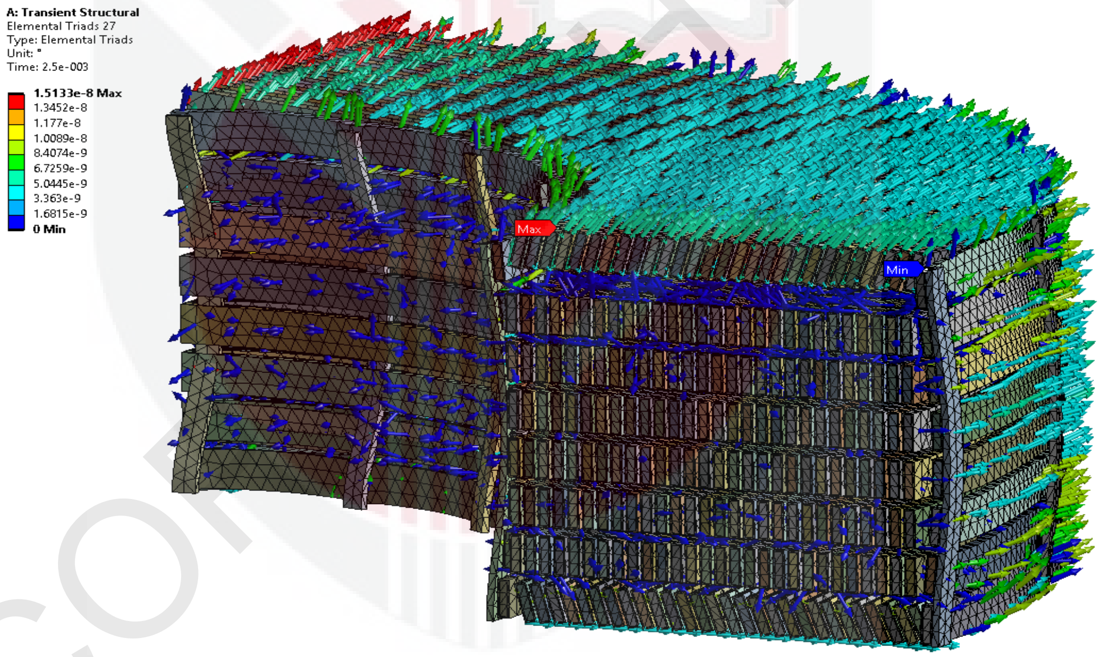
A: Transient Structural
Elemental Triads 27
Type: Elemental Triads
Unit: *
Time: 2.5e-003
1.5133e-8 Max
1.3452e-8
1.177e-8
1.0089e-8
8.4074e-9
6.7259e-9
5.0445e-9
3.363e-9
1.6815e-9
0 Min
Max
Min

(b)

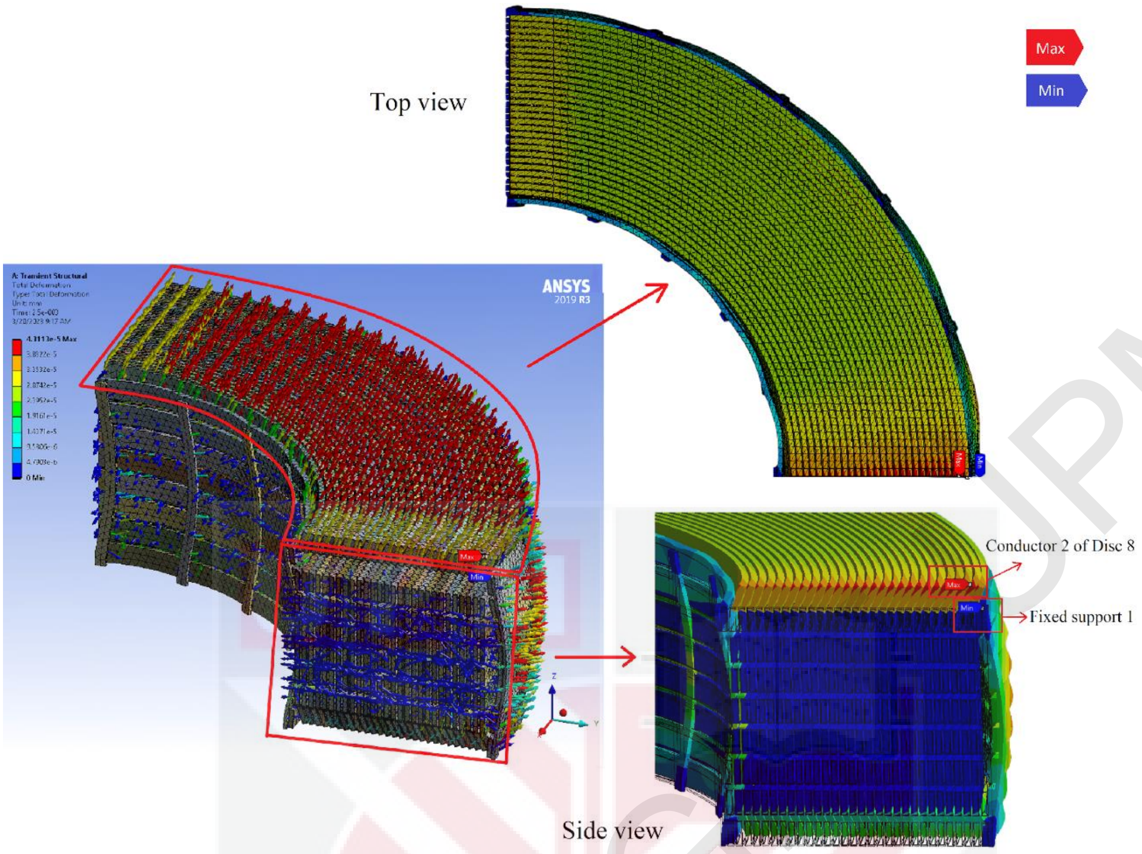

(c)

Figure 4.13: Total deformation of disc winding due to SSI voltage with (a) true scale, (b) 0.5x auto-scale and (c) auto-scale

The total deformation of disc winding under NSSI voltage shows that the maximum deformation occurs at the copper conductors within the middle section of the bottom disc layer with a peak magnitude of 4.31×10^{-5} mm based on the true scale deformation factor. The minimum deformation occurs at the fixed supports, with 0 mm. The side view shows that all disc layers experience displacement as the copper conductors displace towards the upper region. The top view shows that the radial deformation causes the copper conductors to bend outward. The magnitude of total deformation gradually decreases from the middle to the outer circumference of the disc winding.

Table 4.7: Total deformation of disc winding under NSSI

Scale factor	Minimum (mm)	Maximum (mm)	Average (mm)	Minimum Occurs On	Maximum Occurs On
True scale	0	4.31×10^{-5}	7.30×10^{-6}	Fixed support 1	Conductor 5 (Disc 8)
0.5x Auto-scale	0	8.62×10^{-4}	14.62×10^{-5}	Fixed support 1	Conductor 5 (Disc 8)
Auto-scale	0	21.55×10^{-2}	36.51×10^{-3}	Fixed support 1	Conductor 5 (Disc 8)

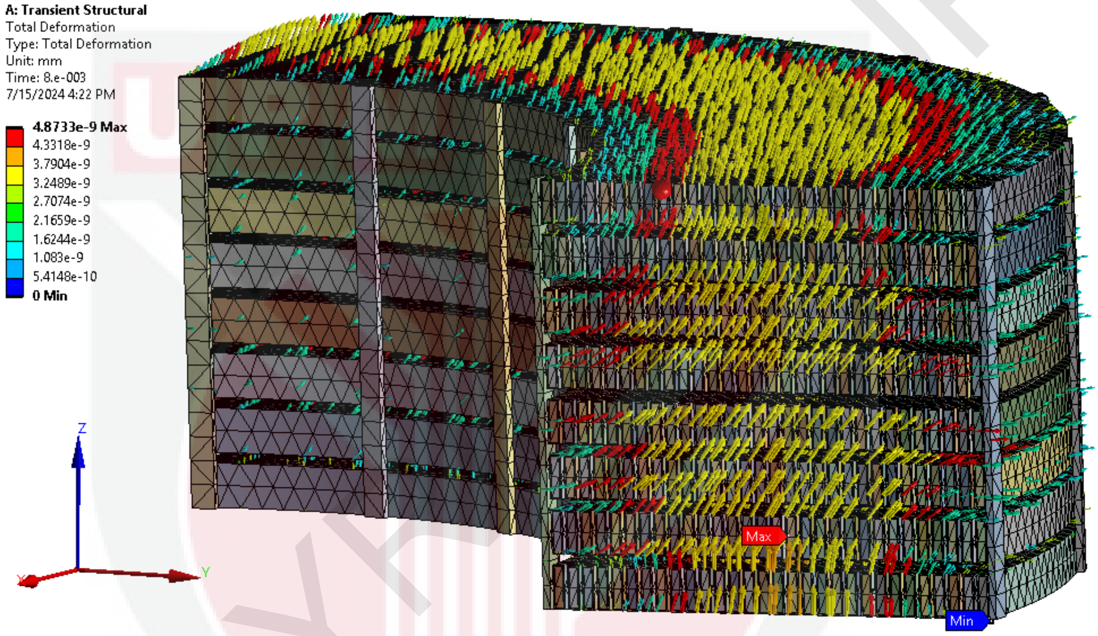

(a)

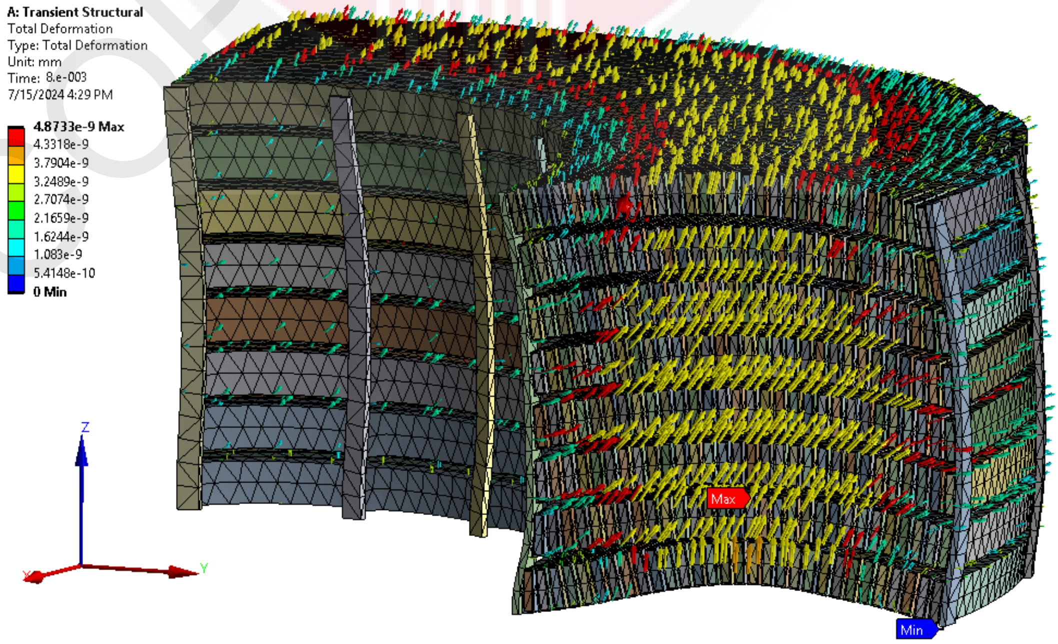

(b)

© COPYRIGHT UPM

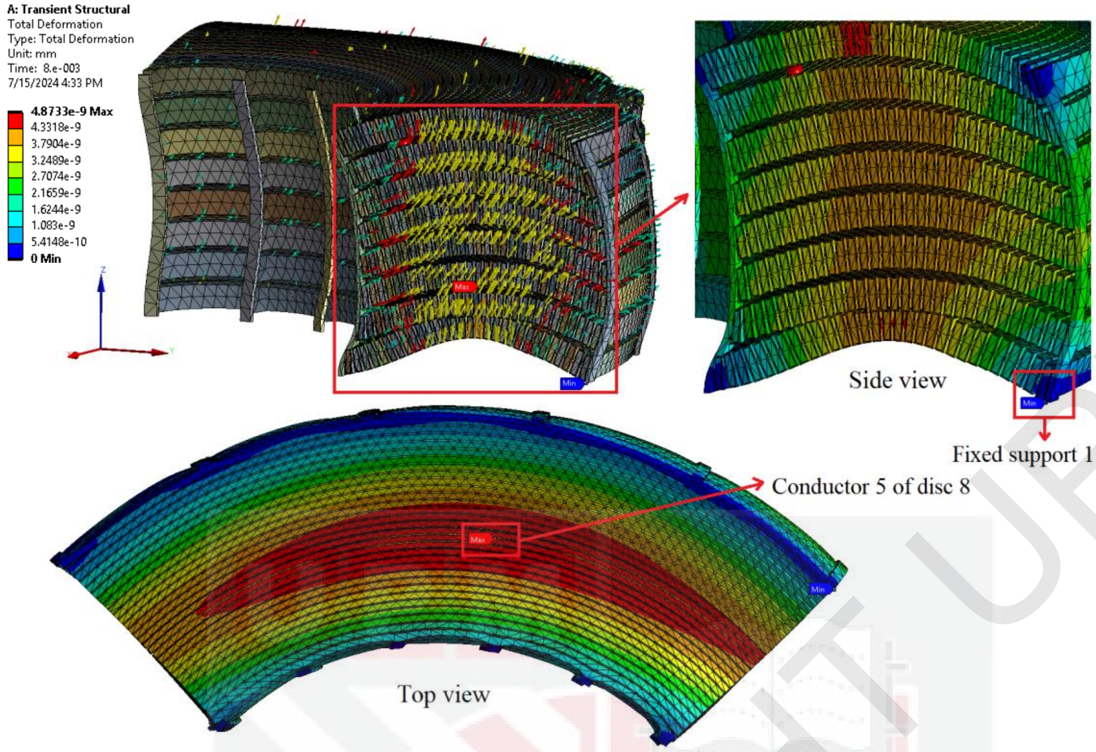

(c)

Figure 4.14: Total deformation of disc winding due to non-standard SI with (a) true scale, (b) 0.5x auto-scale and (c) auto-scale

The total deformation of disc winding under SSI voltage is concentrated and severe at the outer disc layers and circumference, which indicates a non-uniform distribution and localised structural deformation. The total deformation of disc winding under NSSI voltage is widespread non-uniformly throughout the entire disc winding and leads to global structural deformation. It is found in [160] that localised deformation tends to be more immediate and severe, while global deformation leads to gradual degradation in transformer winding mechanical stability.

4.4 Switching transient model analysis through three-way coupling

© COPYRIGHT UPM

4.4.1 Ohmic losses

Figure 4.15 illustrates the distribution of ohmic losses in the 8 disc layers under 1 cycle of SSI voltage. During the first 1 ms, the ohmic losses are relatively low and stable across all disc layers, which indicates minimal energy dissipation. As the time progresses beyond 1 ms, there are significant increments of ohmic losses whereby sharp peaks become frequent and prominent. Significant peaks of ohmic losses are observed between 2 ms and 2.5 ms, which indicate periods of high resistance and energy dissipation. The numbers of high peaks of the ohmic losses are apparent at disc layers 8 and 7 after 2 ms. It is due to the material properties of the copper conductors or its position in the disc winding [161]. Local resistivity changes in copper conductor due to temperature rise contribute to increased ohmic losses in the regions. The disc layers near the winding's outer circumference experience greater voltage differentials, which results in higher current densities and ohmic losses.

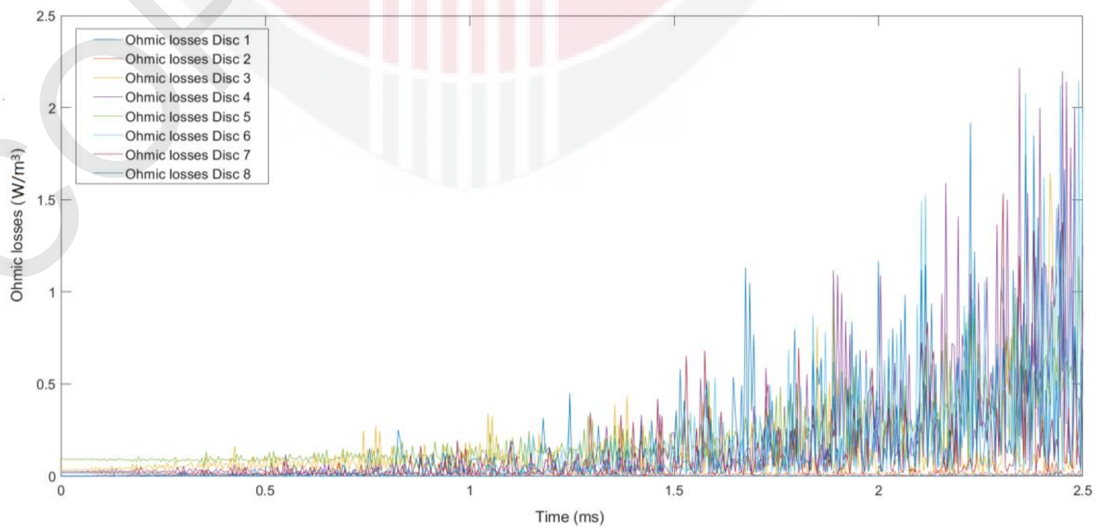

Figure 4.15: Ohmic losses in 8 discs under SSI voltage

4.4.1.1 Spatial distribution of ohmic losses in disc winding

The spatial distribution of ohmic losses within the disc winding is shown in Figure 4.16. It is found that the ohmic losses are not uniformly distributed across the disc winding. The ohmic losses appear concentrated at the outermost disc layers, particularly towards the outer edges and ends of the disc winding. The inner sections of the disc winding show comparatively low ohmic losses. The highest ohmic losses are observed at the copper conductor of the topmost disc layer 8. The non-uniform ohmic loss distribution might be due to microstructural variations within the disc winding that cause uneven resistivity, which leads to localised areas with higher ohmic losses.

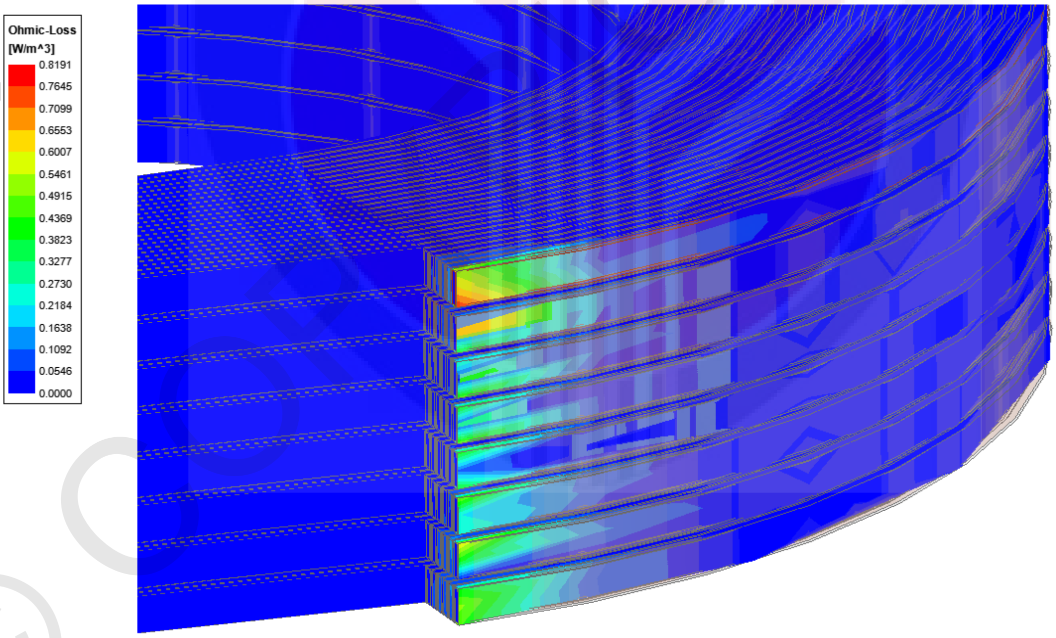

Figure 4.16: Spatial distribution of ohmic losses in a disc winding due to SSI voltage

© COPYRIGHT UPM

4.4.1.2 The relationship between SSI voltage distribution and average ohmic losses.

The relationship between SSI voltage distribution and ohmic losses is shown in Figure 4.17. It is found that the ohmic losses decreases with the decrement of the SSI voltage distribution within the disc layers. The resistances of disc layers are almost constant, which indicate that the variation in losses is predominantly due to changes in the current that is caused by the impulse voltage distribution. High SSI voltage results in high ohmic losses due to current surge through the disc layers. The topmost disc layer experiences high ohmic losses due to high SSI voltage, which lead to higher heat dissipation as compared to disc layers at the bottom of the disc winding.

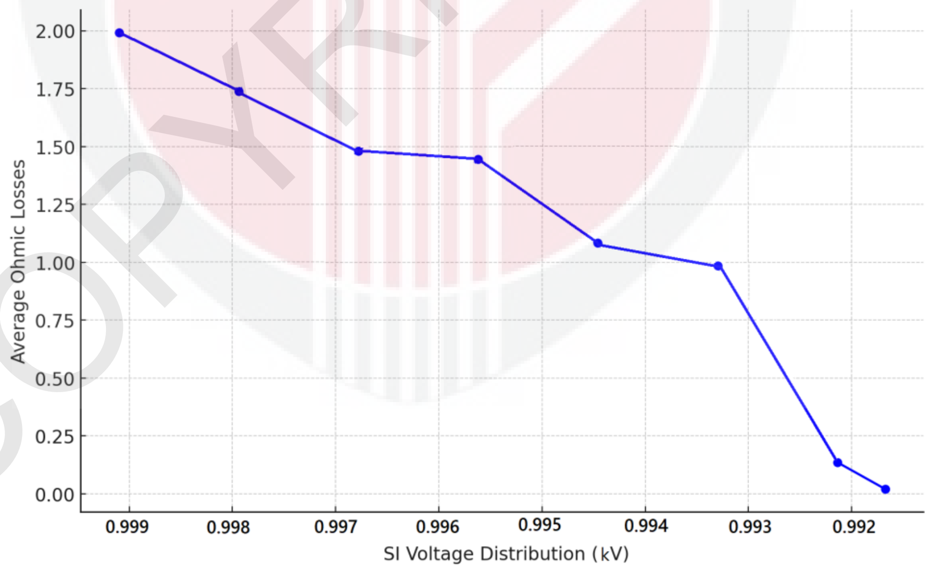

Figure 4.17: Relationship between SI voltage distribution and ohmic losses in 8 disc layers

4.4.2 Temperature distribution

The primary focus of this analysis is to evaluate the distribution of temperature rise and potential hot spot temperatures within the disc winding under the SSI voltage.

4.4.2.1 Total heat flux

The heat flux variation along the height of the disc winding indicates uneven heat distribution as shown in Figure 4.18. The maximum heat flux distribution appears stable with low fluctuation until 1 ms. The fluctuation is around 0.6 W/mm^2 with minor spikes that reach around 1.0 W/mm^2 and 1.2 W/mm^2. After 1 ms, the maximum heat flux shows significant fluctuations and frequent spikes, which can reach up to 2 W/mm^2. The average heat flux remains relatively stable and has low fluctuation around 0.05 W/mm^2. These patterns show that while localised regions experience high heat flux, the overall heat transfer across the winding is relatively low. The minimum heat flux remains close to zero which indicates that some areas of the winding experience very low heat transfer and remain at low temperature throughout the switching transient.

© COPYRIGHT UPM

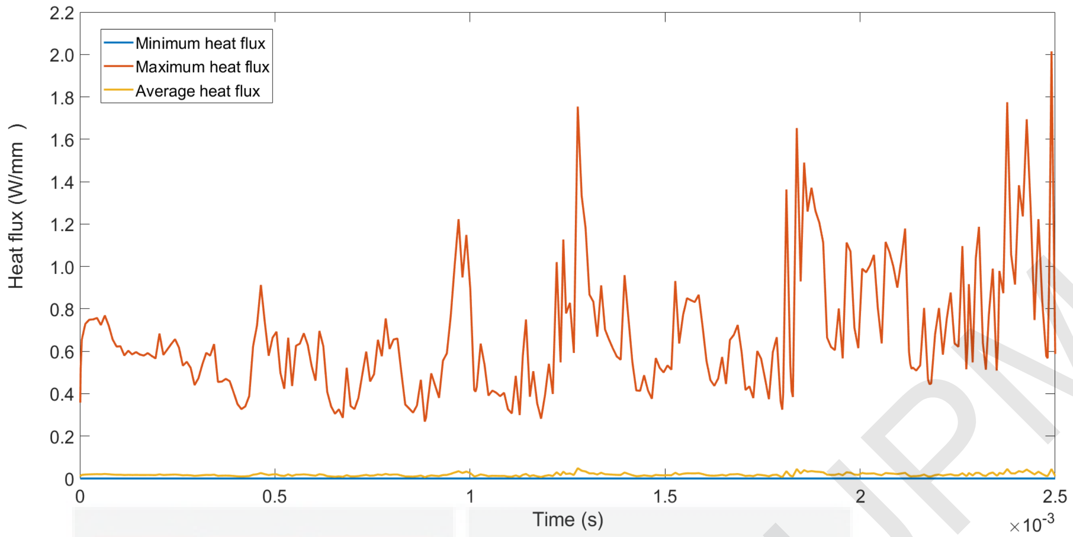

Figure 4.18: Total heat flux

Figure 4.19 shows heat flux distribution and profile along the height of the 8 disc layers. The topmost disc layer winding exhibits the highest heat flux and gradually decreases towards the bottom disc layers. It shows a stepped decrease in heat flux from the top of the winding to the bottom of the winding. The heat flux varies significantly across different layers of the disc winding. The heat flux distribution is uniformly distributed across the turns of the winding, therefore the flux at turns 1 to 5 are consistent for all disc layers. This condition implies consistent energy dissipation along the horizontal turns within a disc layer.

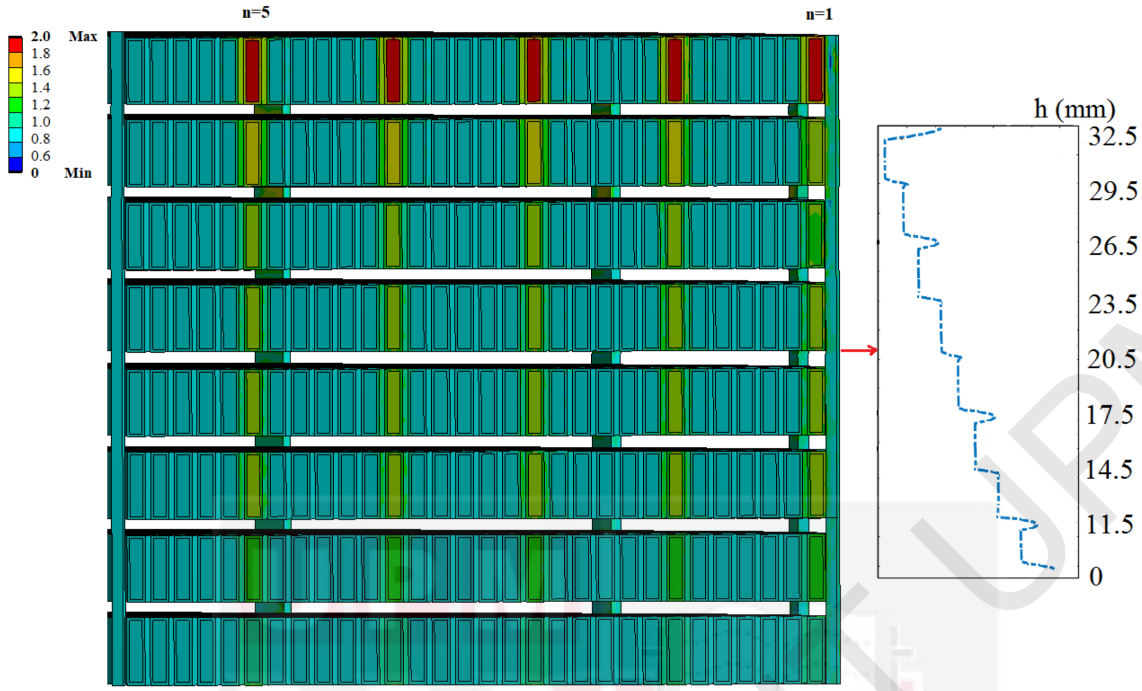

Figure 4.19: Heat flux in the 8 disc layers

4.4.2.2 Thermal gradient

Through iterative calculations, the disc winding model is updated based on the thermal field calculation until the maximum difference in the temperature between the 2 adjacent steps is less than 0.01 C°. The electric-thermal analysis is shown in Figure 4.20 and Figure 4.21. Figure 4.20 shows the temperature gradient within the disc winding under 1 cycle of SSI voltage. The maximum temperature steadily increases over time and can reach higher than 400 °C. The minimum temperature decreases linearly close to -400 °C. The average temperature remains relatively stable and stays close to 0 °C throughout the analysis. The extreme temperature difference between the maximum and minimum temperatures in the disc winding indicates a non-uniform temperature distribution across different parts of the disc winding. It is due to the effects of ohmic losses and heat dissipation. Ohmic losses generate heat within the conductors that leads to localised temperature rise, while the heat dissipation mechanisms, including conduction, convection and radiation, vary across different regions of the winding. This results in significant temperature variations which impact the overall thermal gradients of the winding.

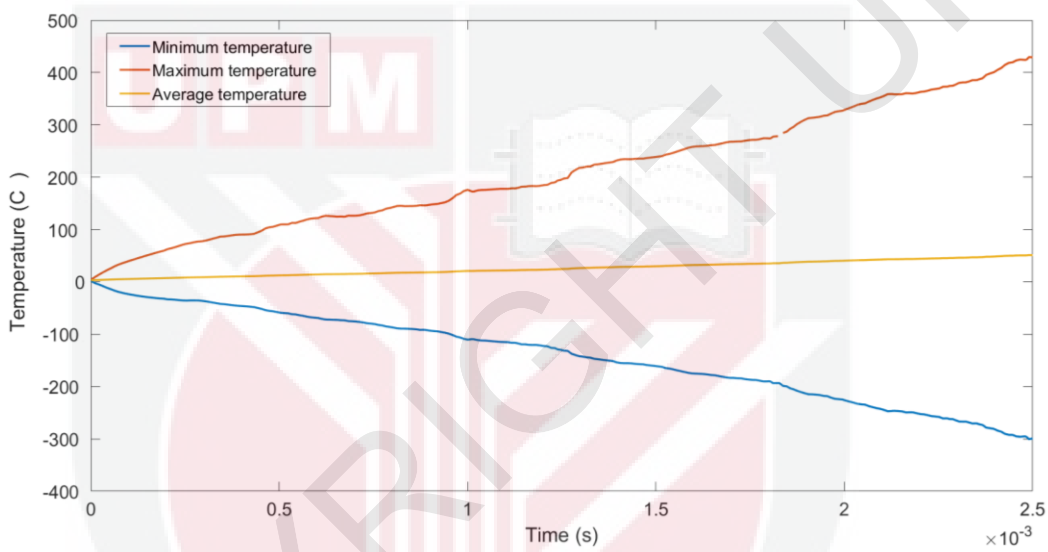

Figure 4.20: Temperature gradient within the disc winding

Figure 4.21 shows the temperature distribution in disc winding due to the SSI voltage. The temperature of the disc winding hot spot is 428.6 C°, which is located at the topmost disc layer. High temperatures are concentrated at the outer edges of the initial turns of the disc layers, particularly at the region of the SSI voltage injection point. The hotspot temperatures in the disc winding coincide with the disc layers of high ohmic losses. There is a clear gradient where the temperature decreases steadily towards the bottom of the disc winding. This is due to the attenuated effect of the SSI voltage and ohmic losses as it propagates to the bottom of the disc winding. The finding on temperature distributions is in line with the finding in [162] that shows the high temperature distribution is at the top of winding.

Figure 4.21: Temperature distribution in disc winding due to SSI voltage

4.4.3 Structural deformation and displacement due to thermal effect

The thermal-structural transient analysis examines the impact of transient thermal loads caused by the SSI voltage that leads to stresses and structural deformations within the disc winding. The critical areas where temperature-induced stresses that lead to material degradation or structural deformation are discussed

4.4.3.1 Effect of temperature on the structural behaviours of disc winding

The total deformation of disc winding due to thermal effect under 1 cycle of SSI voltage is shown in Figure 4.22. The maximum deformation starts at 2.5×10^{-13} mm and gradually increases reach up to 4.0×10^{-13} mm over 1 ms which indicates the presence of thermal expansion within the disc winding. The

© COPYRIGHT UPM

significant variations of the maximum deformation during the first 1 ms indicate that the winding experiences initial thermal expansion. After 1 ms, the maximum deformation slightly stabilises but continues to deform to 5.0 × 10^{-13} mm. The average deformation slightly increases during the first 1 ms, but remains within the range between 0.3 × 10^{-13} mm and 1.0 × 10^{-13} mm. The average deformation becomes more consistent after 1 ms, with peak deformation at 1.2 × 10^{-13} mm. The minimum deformation stays constant at zero throughout the 2.5 ms, which indicates that some parts of the winding are unaffected by the thermal expansion.

The rapid increase in maximum deformation during the first 1 ms is due to the initial thermal expansion experienced by the winding when exposed to transient temperature changes. This occurs because the thermal expansion coefficient of the conductor material causes elongation and structural displacement as the temperature rises. After 1 ms, the deformation stabilises, indicates that heat dissipation reduces the rate of expansion. The average deformation remains relatively stable as heat conduction within the winding occurs gradually, leading to more uniform expansion over time. In contrast, the minimum deformation remaining at zero suggests that certain areas of the winding, such as insulated regions or mechanically constrained sections, experience negligible thermal expansion due to structural constraint.

These findings align with previous studies in [46], which demonstrated that transformer windings undergo rapid expansion during the initial thermal transient phase. Research by [163] found that thermal expansion in disc

© COPYRIGHT UPM

windings is significantly influenced by structural constraints and insulation properties, explaining why minimum deformation remains constant in some sections. The study also highlighted that materials with higher thermal conductivity exhibit more gradual and uniform expansion, supporting the observed behaviours of average deformation in this study.

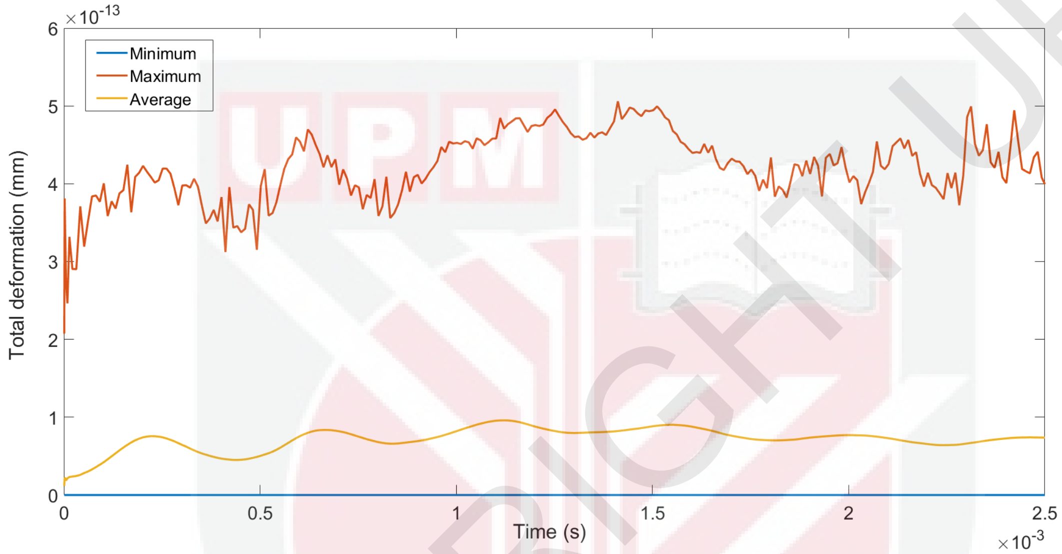

Figure 4.22: Total deformation of disc winding due to thermal effect

The structural deformation of the disc winding subjected to thermal effects due to the SSI voltage is shown in Figure 4.23. The deformation is shown in 3 deformation scale factors to show the escalation in the thermal stress experienced by the disc winding. The progressive deformation highlights the impact of thermal effects on the copper conductors, Kraft insulation paper and structural steel fixed support.

The copper conductors show extensive deformation, with noticeable deformations and shifts in its alignment. As the thermal effects intensify, the deformations become apparent, especially on the top disc layers and outer circumference of the disc winding. This deformation results from differential thermal expansion, where different parts of the copper conductors heat up and expand at different rates. It can be seen from the side view of the conductor disc winding that the deformation also occurs axially as slight axial displacement of conductors is observed.

At true scale, minor degradation or crinkling is observed, where the Kraft insulation paper remains intact. The Kraft insulation paper shows significant signs of crinkling, distortion and tears as the deformation scale factor increases. The expansion of the copper conductors forms wavy patterns cause the Kraft insulation paper to stretch radially in some regions and compress in others that leads to the tears and crinkles. Continuous exposure to high temperatures, especially near the hot spots accelerates the thermal aging of the Kraft insulation paper. The Kraft insulation paper becomes brittle over time loses its elasticity and is not able to withstand the expansion and contraction of the copper conductors.

The structural steel fixed supports exhibit signs of bending as the deformation scale factor increases. The thermal mismatch between the expanding copper conductors and vertical structural steel fixed support creates mechanical stress at the contact points. As the copper conductor expands, the structural steel fixed supports restrain it and cause compressive stress on the copper conductors. Concurrently, the structural steel fixed supports experience

© COPYRIGHT UPM

counteracting forces from the expanding copper conductors that lead to the bending especially at the contact points.

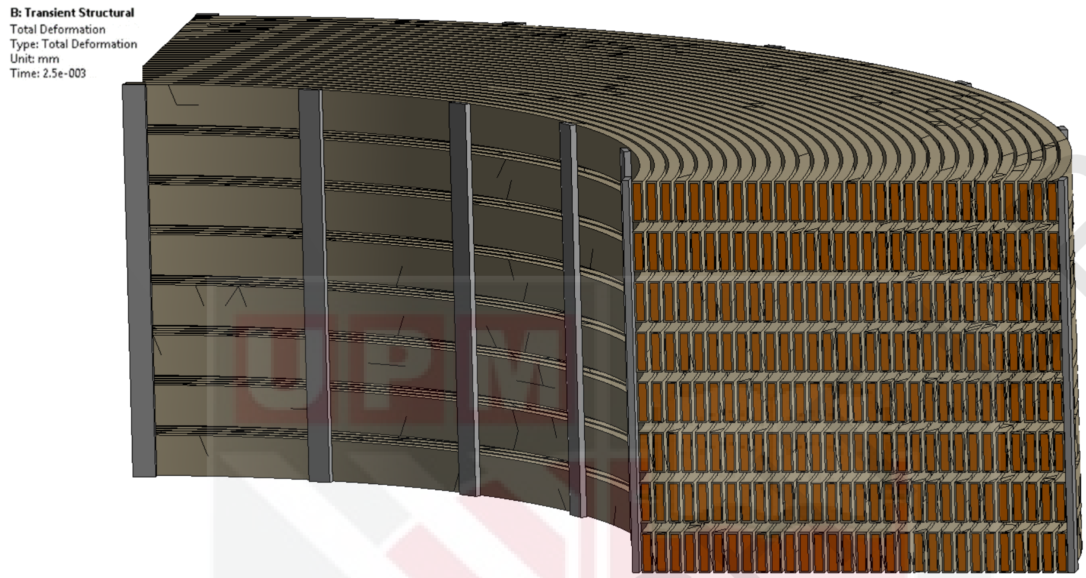

(a)

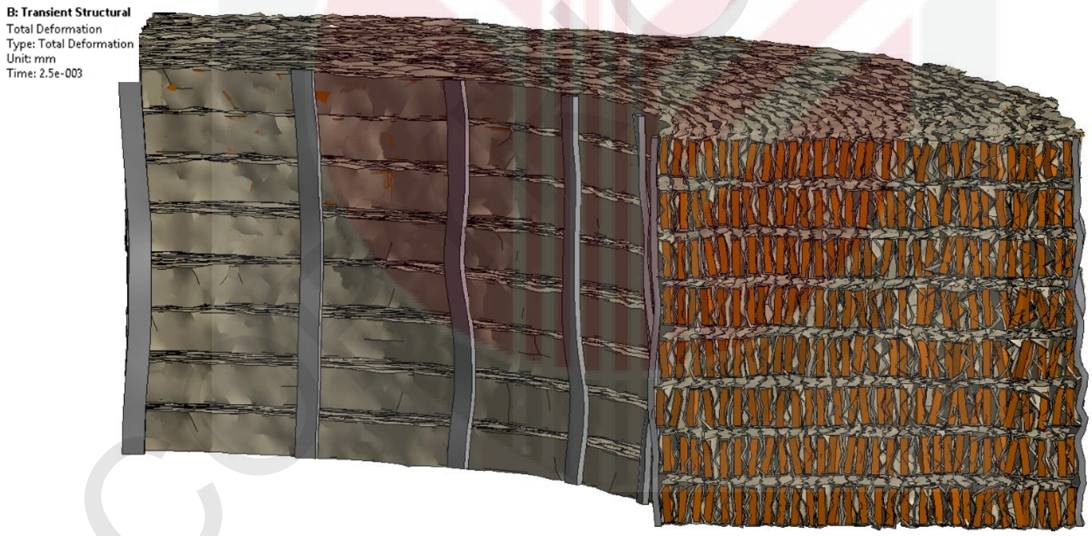

(b)

© COPYRIGHT UPM

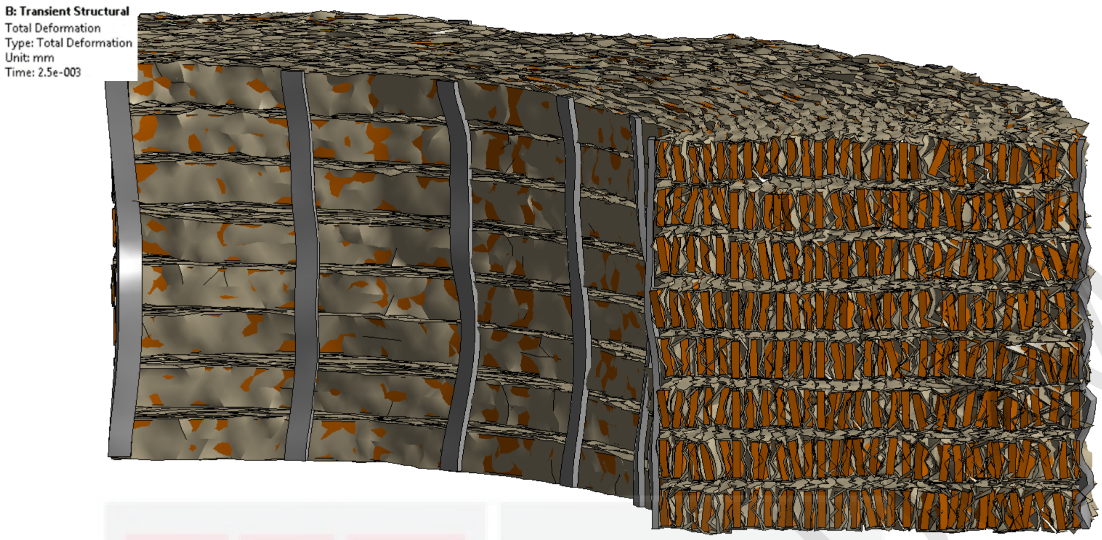

(c)

Figure 4.23: Total deformation of disc winding due to thermal effect with (a) true scale, (b) 0.5x auto-scale and (c) auto-scale

Detailed deformation of the copper conductor due to thermal effects under SSI voltage is shown in Figure 4.24. The side view of the copper conductors shown in Figure 4.24 (a) reveals apparent misalignment and separation between the copper conductors. The gaps between each of the disc layers indicate that the thermal stress leads to differential expansion, which causes the copper conductor to expand at different rates and results in axial displacement. The copper conductors between the structural steel fixed supports seem to experience more significant deformation compared to those near the fixed supports due to the mechanical constraints imposed by the fixed supports.

The top view of the conductor disc winding in Figure 4.24 (b) reveals the radial expansion of the copper conductors. The copper conductors show significant ripple radial deformation patterns as it experience significant radial expansion due to the thermal effects. The outer copper conductors at the circumferences appear to experience more radial expansion, which results in significant deformation and greater misalignment than the inner conductors. The radial expansion causes the copper conductors at the circumferences to buckle inward more significantly than the inner conductors.

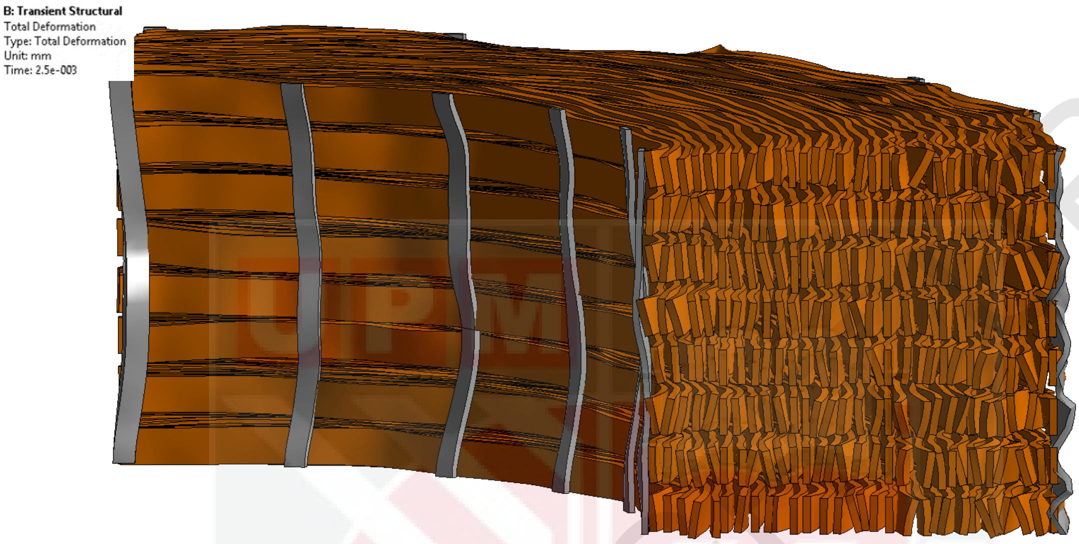

(a)

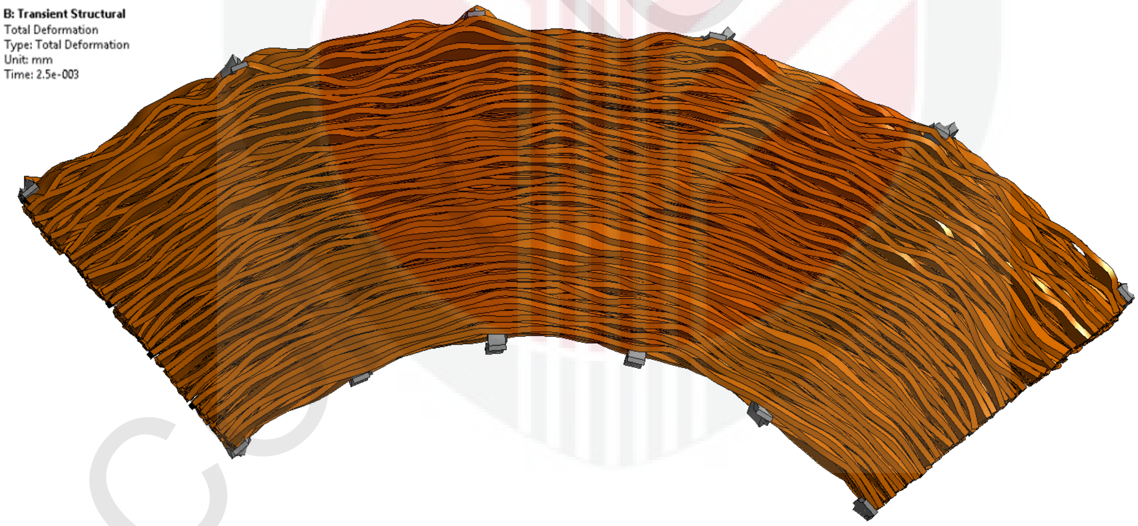

(b)

Figure 4.24: Details deformation of (a) side and (b) top view of conductor disc winding due to the thermal effect

The deformations observed on the disc winding show clear indications of thermal expansion effects on the copper conductors. The restrained expanding copper conductors create ripple bending and displacement that cause conductors misalignment throughout the disc winding structure which is in line with previous study in [51].

4.4.3.2 Relationship between thermal and structural deformation

Figure 4.25 illustrates the relationship between the applied stress and strain of disc winding under the SSI voltage at different temperatures. As the temperature increases from 20 °C to 40 °C and from 60 °C to 80 °C, the strain increases by 17% and 62%. Meanwhile, the tensile strength decreases with the increment of the temperature by 10.5% and 25% respectively. The stress shifts downwards as the temperature increases, which indicates that the ability of the disc winding to withstand stress decreases for the same amount of strain. For example, at 2.5% strain, the stresses for 20°C, 40°C, 60°C and 80°C are around 9.5 MPa, 8.5 MPa, 8.0 MPa and 6.0 MPa respectively.

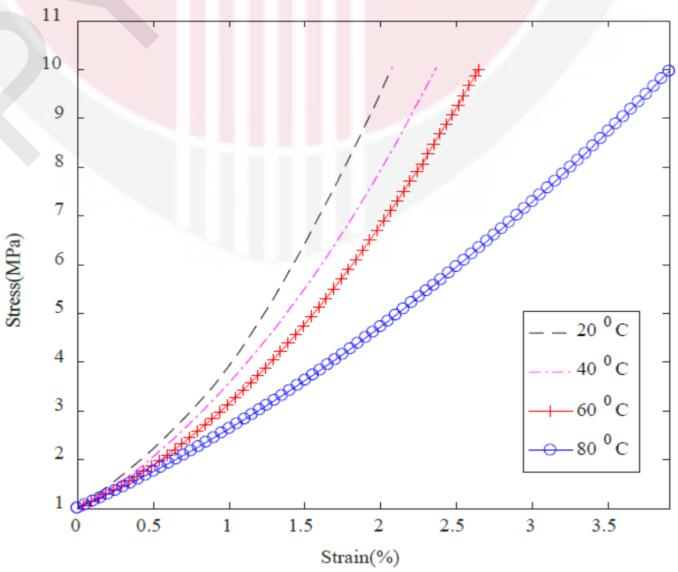

Figure 4.25: Effect of the temperature on the relationship between stress and strain of disc winding

© COPYRIGHT UPM

4.5 The structural mechanical response and stability of disc winding under switching transient

The structural buckling behaviour of disc windings is a critical factor that influences its mechanical stability during the switching transient. Buckling can be induced by mechanical stresses, which result from electromagnetic forces and thermal stresses from the thermal expansion within the disc winding.

4.5.1 Structural buckling behaviours of disc winding under SSI voltage

The buckling load factors for 5 modes of electromagnetic force and thermal dependent buckling of the disc winding are shown in Figure 4.26. The supporting data of the load factors are presented in Table 4.8. Generally, the load factor increases as the buckling mode increases. The first mode of buckling under electromagnetic force occurs at a load factor of 1.1, while the fifth mode occurs at a load factor of 3.2. As shown in Table 4.8, the loads for electromagnetic force dependent buckling mode 1 and mode 5 are 31.98 kN and 83.36 kN, respectively. It indicates that as the buckling mode increases, the disc winding structure's resistance to buckling also increases, which lead to high loads for each of the successive modes.

The thermal dependent buckling modes show similar patterns as the electromagnetic force dependent. However, the thermal dependent buckling load factors are higher than the electromagnetic force dependent. The load factors for mode 1 and mode 5 are 1.2 and 3.8, respectively. This indicates that the disc winding structure is more resilient to thermal effects as compared

© COPYRIGHT UPM

to electromagnetic force since it requires a higher load factor to cause instability.

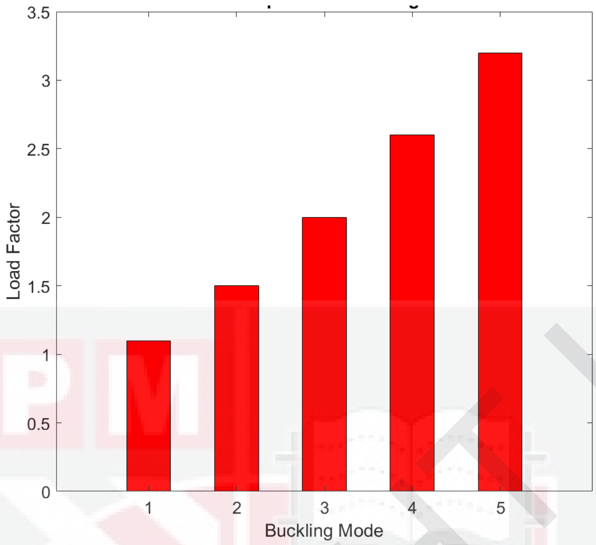

(a)

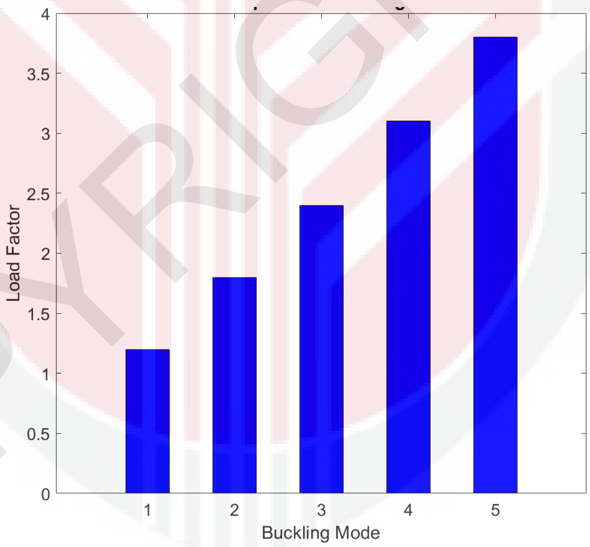

(b)

Figure 4.26: (a) Electromagnetic force and (b) thermal dependent buckling load factors

© COPYRIGHT UPM

Table 4.8: Buckling load factors

Buckling load	Mode 1	Mode 2	Mode 3	Mode 4	Mode 5
Force dependent (kN)	31.98	35.97	53.15	64.09	83.36
Thermal dependent (°C)	57.10	65.88	95.04	120.08	159.38

Figure 4.27 shows the electromagnetic force dependent buckling deformation patterns that are associated with the 5 buckling modes. Each of the modes represents a specific buckling pattern that the disc winding structure exhibits under the electromagnetic force. The increment of the oscillations along the length of the disc winding is associated with the increment of the mode, which leads to significant deformation. It is found that the weak points or areas prone to deformations vary accordingly based on the variations of the oscillation amplitudes.

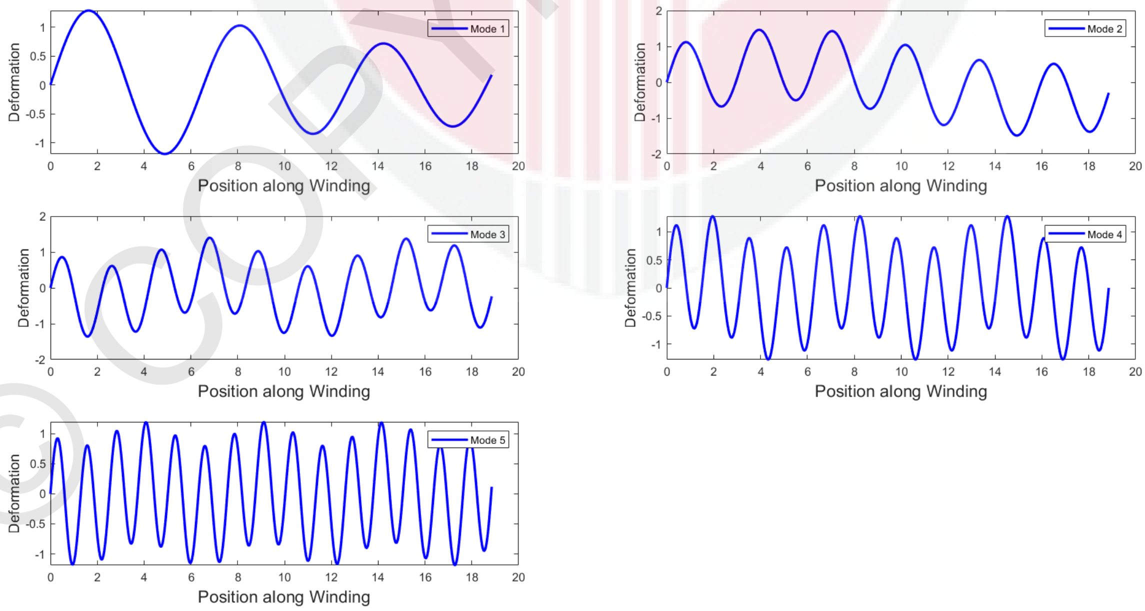

Figure 4.27: The deformation patterns associated with 5 force dependent buckling modes

© COPYRIGHT UPM

The thermal dependent buckling deformation patterns of the disc winding can be seen in Figure 4.28. Each of the modes exhibits a uniform deformation pattern that indicates a homogeneous thermal effect on the disc winding structure. Similar to the buckling due to electromagnetic forces, the oscillations increase with the increment of the modes that signifies pronounced deformations. The uniformities of amplitudes for all modes indicate that thermal effects are distributed more evenly as compared to the electromagnetic forces. While the disc winding may experience uniform expansion or contraction, the high oscillations at high modes indicate regions with concentrated thermal stress.

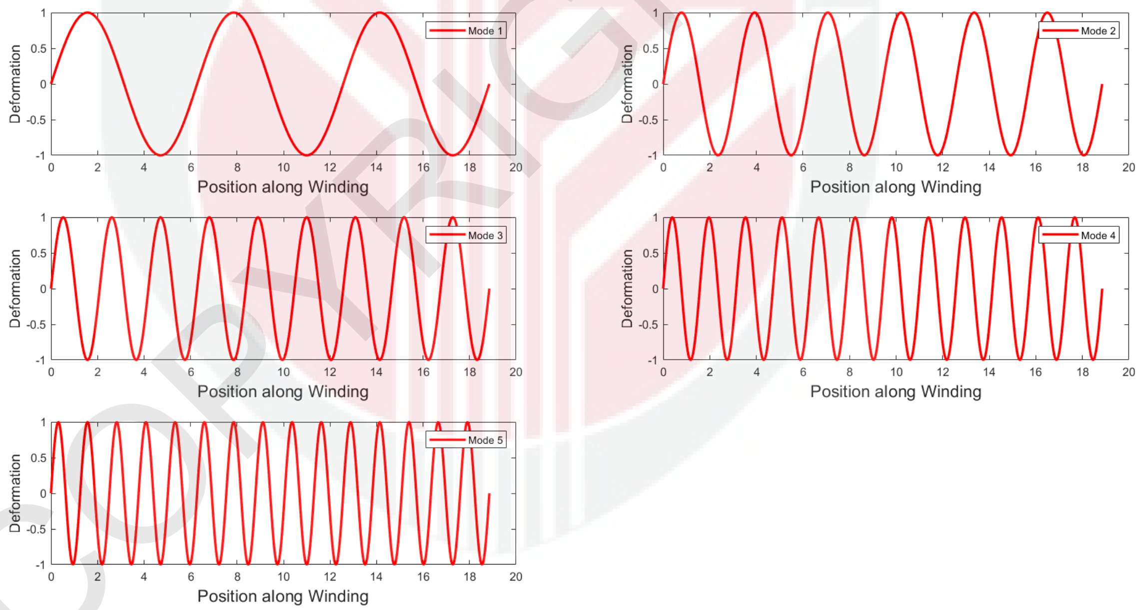

Figure 4.28: The deformation patterns associated with 5 thermal dependent buckling modes

The first 4 modes of buckling behaviours of the disc winding due to electromagnetic force under the SSI voltage are shown in Figure 4.29. The first buckling mode seen in Figure 4.29 (a) shows that the outer and inner

© COPYRIGHT UPM

circumference of the disc winding bends slightly outward. This condition indicates structural instability as the disc winding begins to lose its ability to withstand the tensile stress induced by the electromagnetic forces. The subsequent buckling modes in Figure 4.29 (b), (c) and (d) reveal the increment of severity for buckling deformation patterns. Multiple buckling points are pronounced at the outer circumference of the disc winding, where different sections of the disc winding bend outwardly in non-uniform manners. These conditions show that the disc winding experiences high tensile stresses and different responses are observed at several parts of the disc winding. The progressions from the first to fourth modes show the mechanical instability of the disc winding.

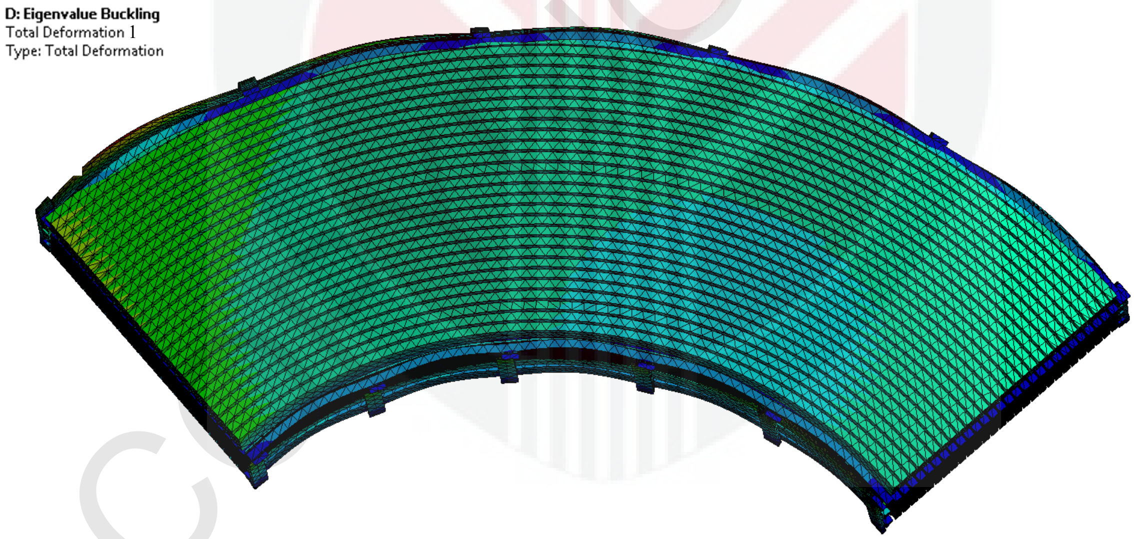

(a)

© COPYRIGHT UPM

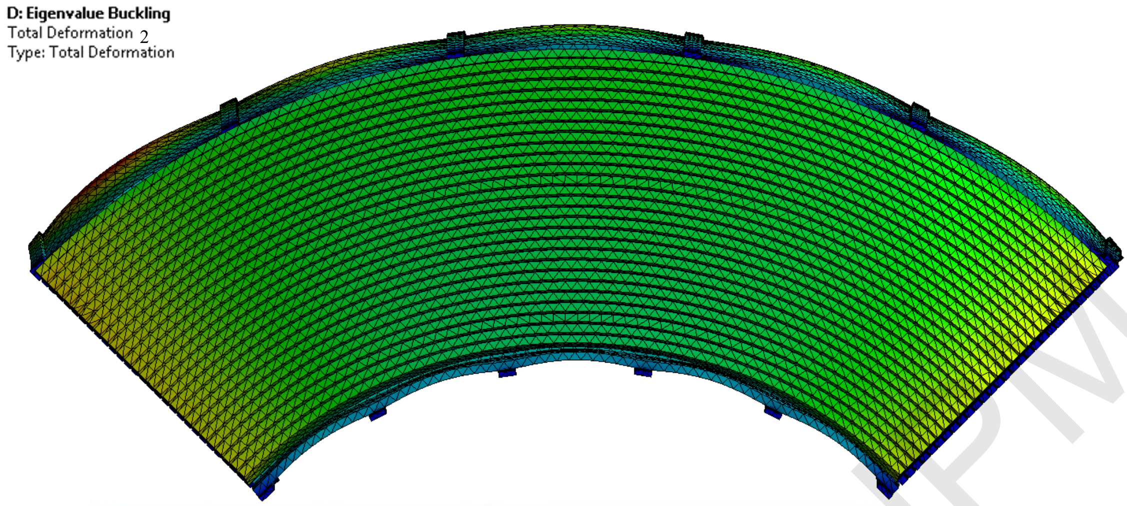

(b)

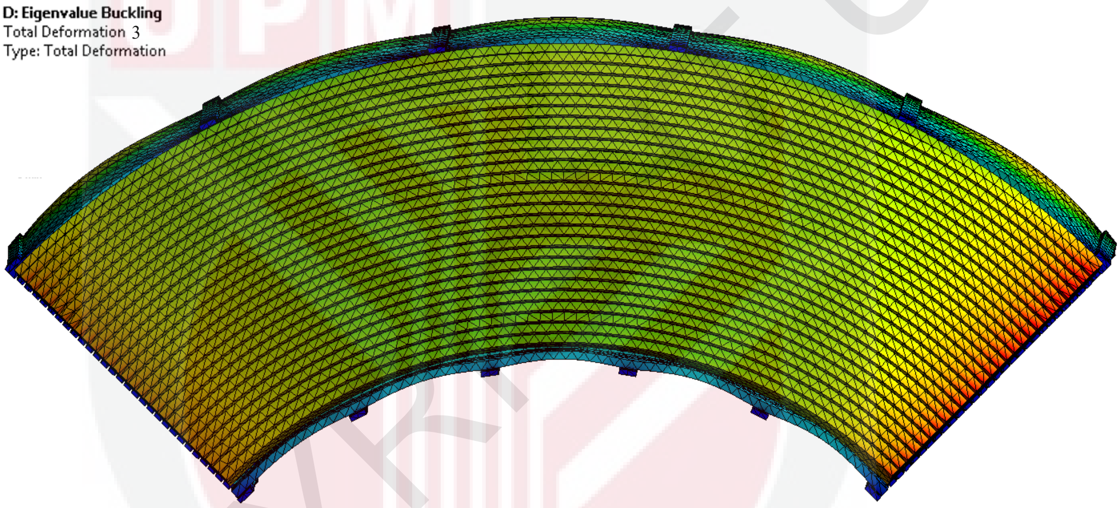

(c)

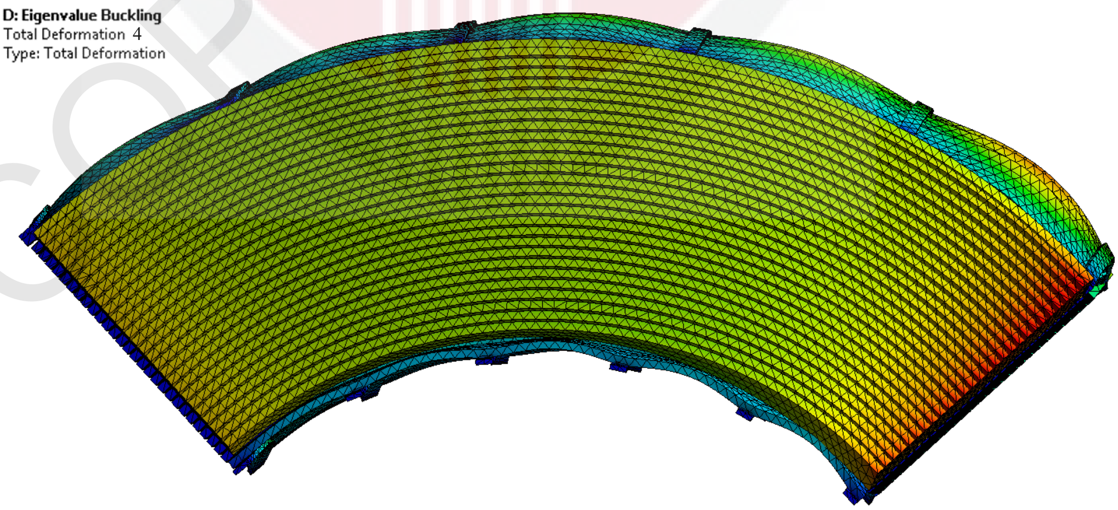

(d)

Figure 4.29: (a) Mode 1, (b) mode 2, (c) mode 3 and (d) mode 4 of electromagnetic force dependent buckling behaviour of disc winding

© COPYRIGHT UPM

The first 4 modes of buckling behaviours of the disc winding structure due to thermal effect under the SSI voltage are shown in Figure 4.30. The first mode in Figure 4.30 (a) shows that the buckling deformation appears minimal, as the disc winding retains its overall shape with wrinkles on the Kraft insulation paper. As the buckling mode increases, the buckling deformations become severe with visible bending and distortion throughout the length of the copper conductors. The copper conductors exhibit a wavy pattern due to the structural steel fixed supports restrain the thermal expansion of the copper conductors. The buckling appears significant at the outer circumference of disc winding, which is subjected to significant thermal expansion. As the copper conductors expand under thermal stress, the Kraft insulation paper begins to buckle, which results in surface irregularities. The Kraft insulation paper exhibits irregular folds and wrinkle patterns of buckling throughout its layers.

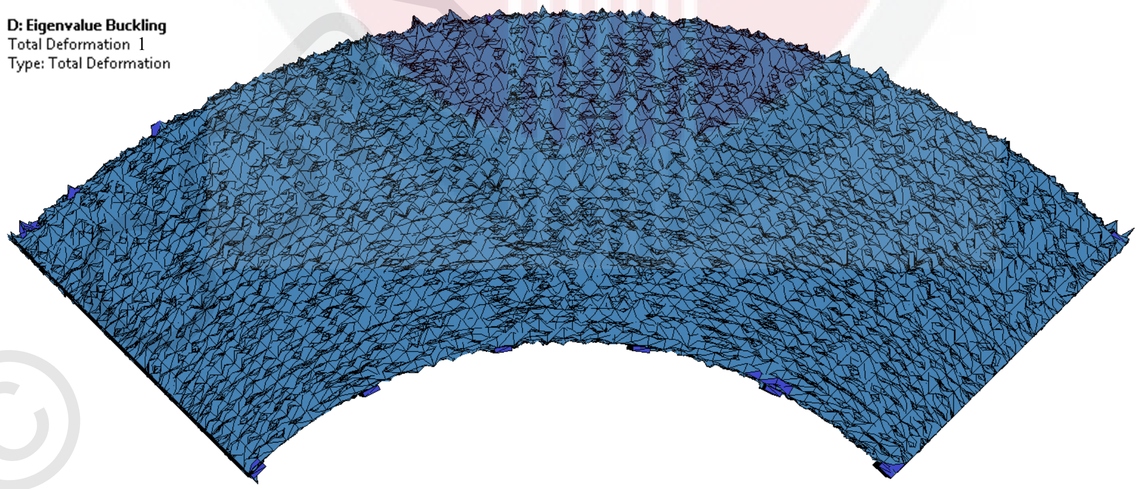

(a)

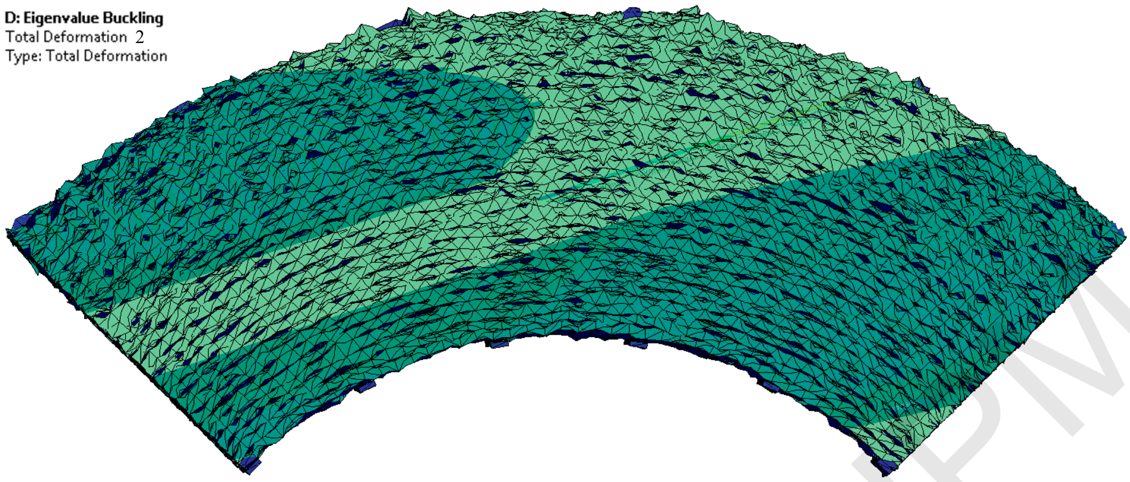

(b)

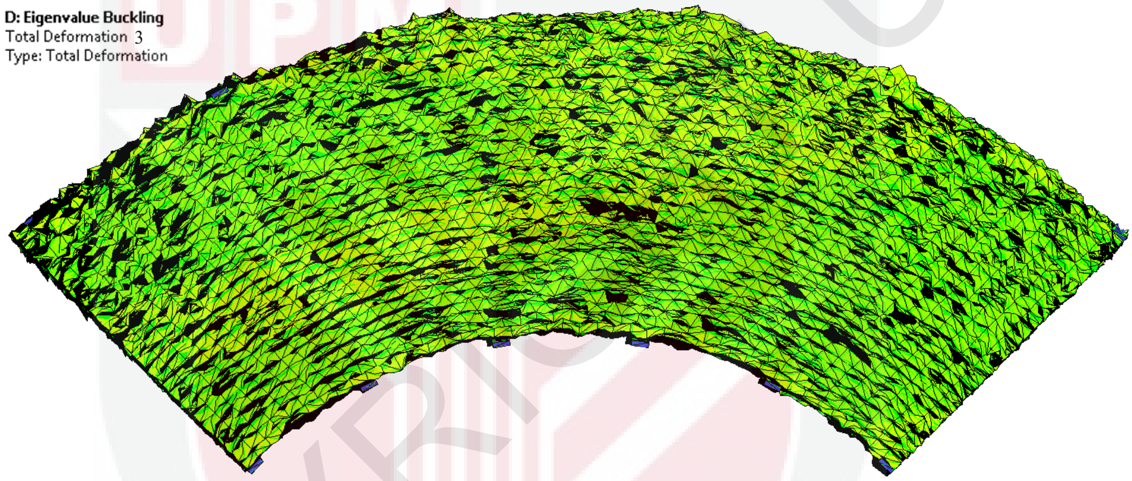

(c)

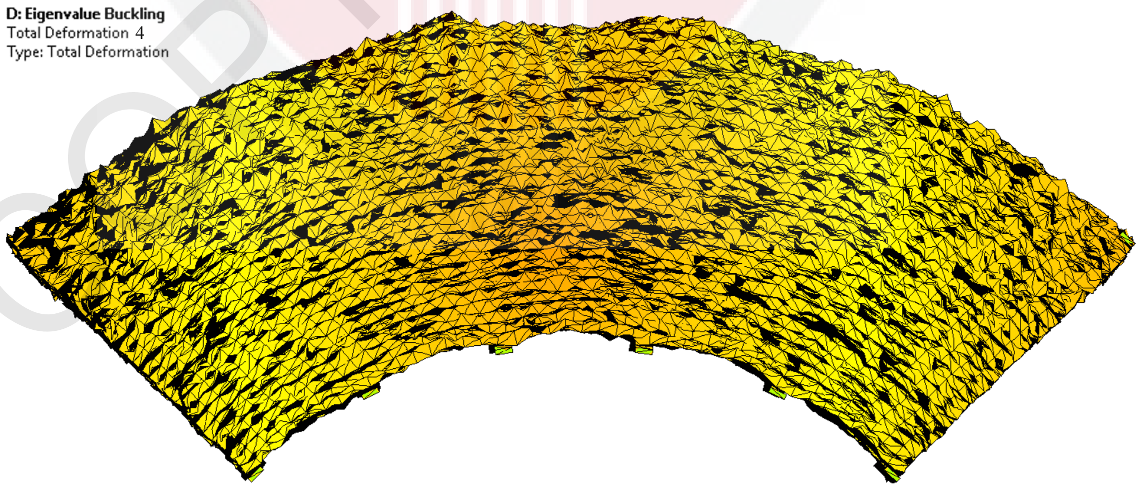

(d)

Figure 4.30: (a) Mode 1, (b) mode 2, (c) mode 3 and (d) mode 4 of thermal dependent buckling behaviour of disc winding

© COPYRIGHT UPM

4.5.2 Electromagnetic force and thermal dependent buckling analysis

The side views of electromagnetic force and thermal dependent buckling mode 4 are shown in Figure 4.31. The electromagnetic force dependent buckling deformation shown in Figure 4.31 (a) and Figure 4.29 (d) shows the combination of buckling deformation mode 4 across the disc winding structure. The overall deformation pattern shows a localised buckling deformation, where the circumferences and outer disc layers experience significant deformation and displacement. The other buckling modes also exhibit localised buckling deformations. The buckling analysis shows that electromagnetic forces cause localised mechanical stability, particularly at the outer disc layers and circumferences of the disc winding where the highest stress concentration is found.

The thermal dependent buckling deformation across the disc winding structure mode 4 is shown in Figure 4.31 (b) and Figure 4.30 (d). The thermal expansion of the copper conductors results in widespread deformation throughout the disc winding structure, with both the radial and vertical disc layers experience significant buckling deformation. The buckling deformation due to thermal expansion leads to global buckling that results in widespread instability across the entire structure of disc winding.

© COPYRIGHT UPM

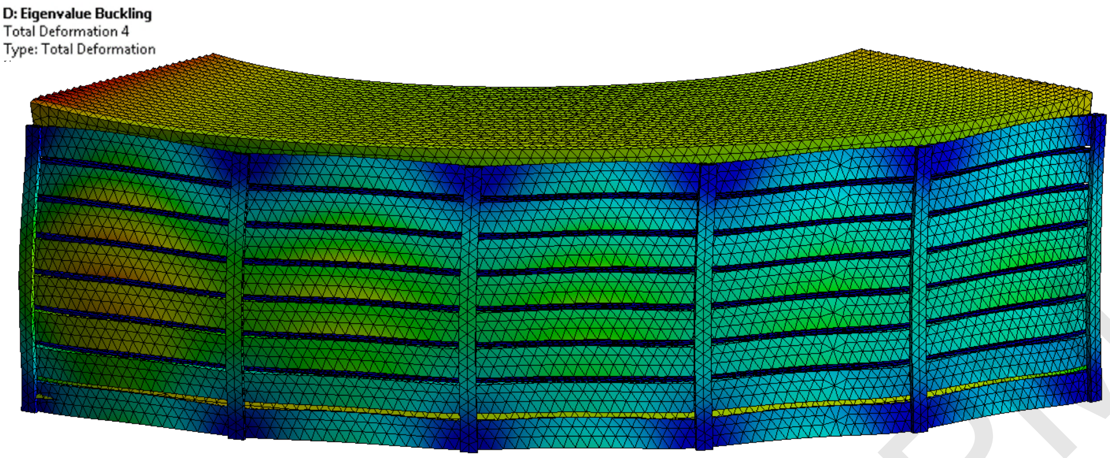

(a)

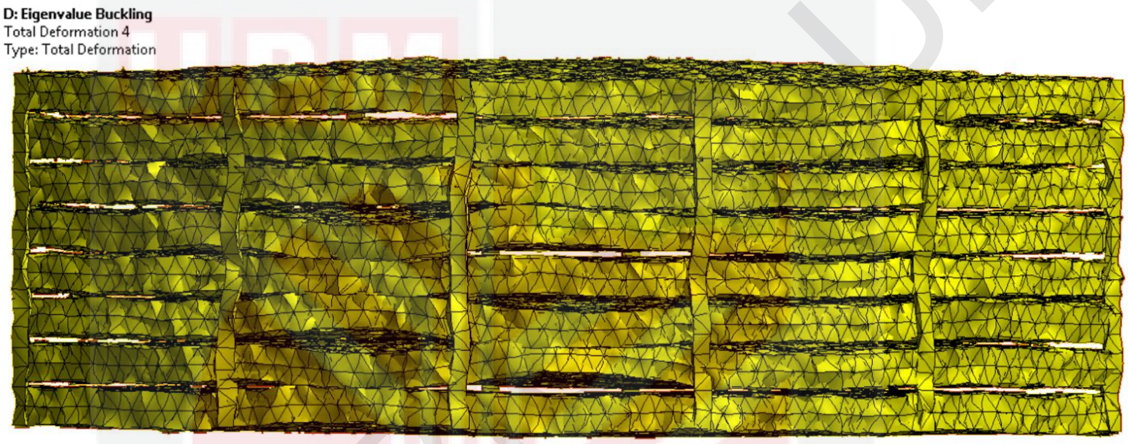

(b)

Figure 4.31: (a) Electromagnetic force and (b) thermal dependent buckling mode 4

4.5.3 Mechanical response of disc winding parts

4.5.3.1 The relationship between applied stress and strain of disc winding materials

The relationships between the applied stresses and strains for different disc winding materials under 5 electromagnetic forces are shown in Figure 4.32. It is found in Figure 4.32 (a) that at electromagnetic force factors 0.6 and 1.0, the strains are 0.8 % and 0.5 % at 100 MPa stress. This indicates that the copper conductors experience less strain as electromagnetic force increases. The graph shows that load factor 1.0 leads to a steeper curve than load factor 0.6, which indicates higher strain rates. This means that the copper conductors deform faster as electromagnetic force increases.

Figure 4.32 (b) shows a linear increment of the strain as the stress increases, followed by a sharp drop to zero stress when the strain reaches 38%. This indicates that the Kraft insulation paper deforms linearly up to 38% strain before it undergoes tears or fractures which leads to a sharp drop to zero stress. The structural steel fixed support in Figure 4.32 (c) shows similar stress and strain behaviours to copper conductors but with higher initial amplitudes of stress. This indicates that the structural steel fixed support is more robust than copper conductors and Kraft insulation paper.

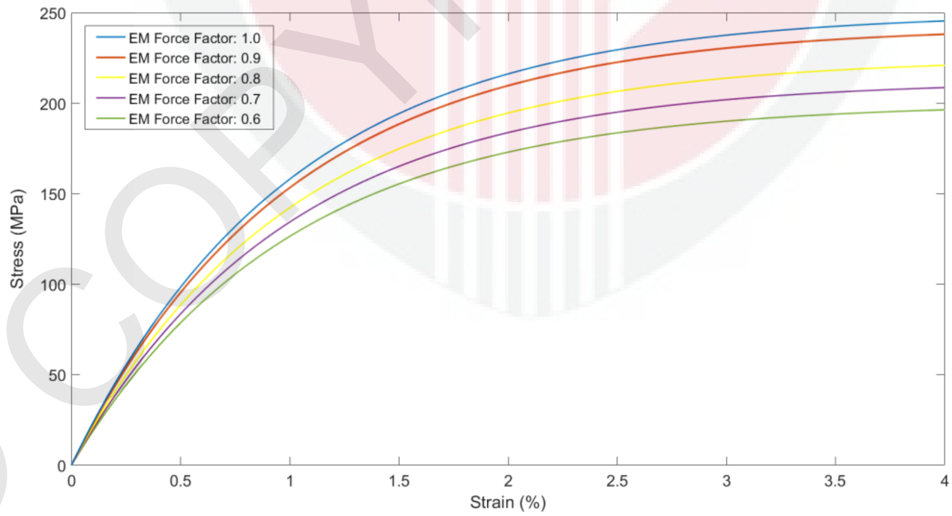

(a)

© COPYRIGHT UPM

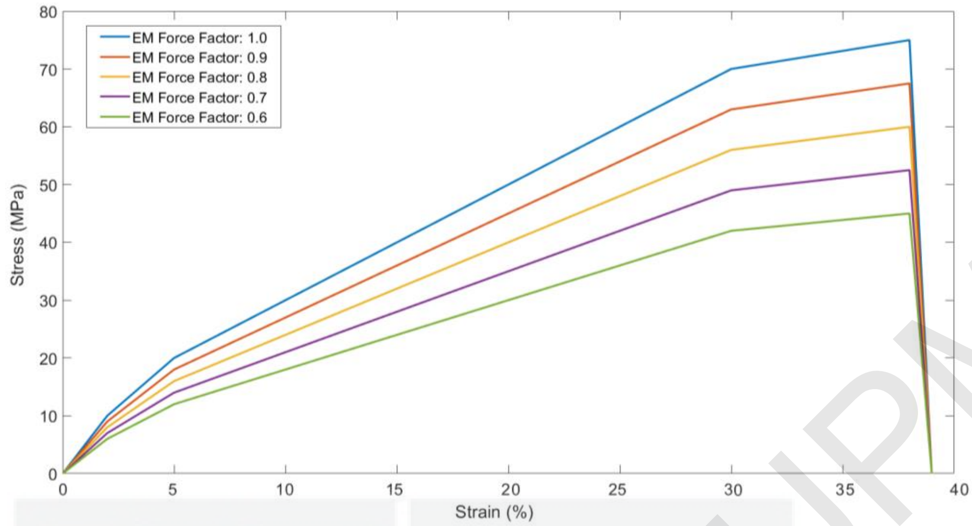

(b)

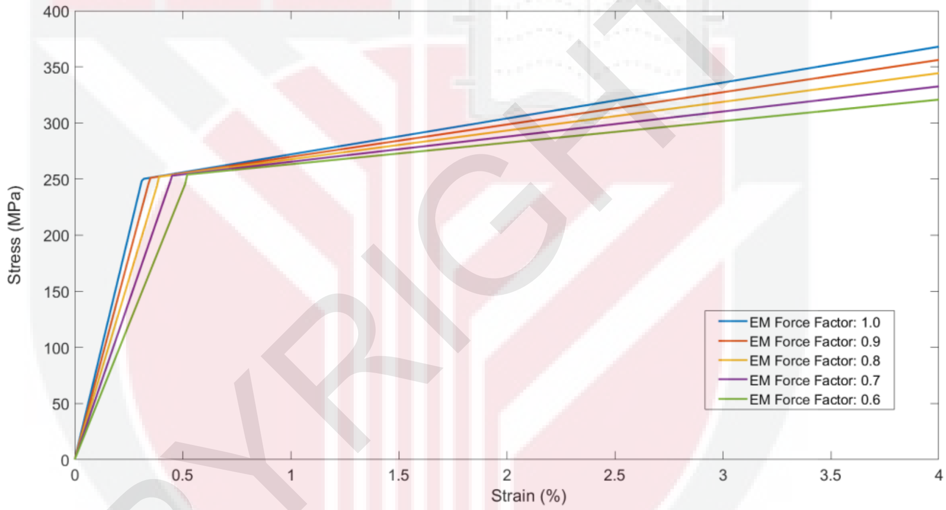

(c)

Figure 4.32: The relationship between applied stress and strain under different electromagnetic forces for (a) copper conductors, (b) Kraft insulation paper and (c) structural steel fixed support of disc winding

The relationship between stress and strain for different disc winding materials under 5 thermal loads can be seen in Figure 4.33. Figure 4.33 (a) shows that as temperature increases from 25 °C to 50 °C and from 100 °C to 125 °C, strain corresponding to 70 MPa has increased by about 0.2 % and 0.4 %, respectively. This indicates that the strain of copper conductors increases at

© COPYRIGHT UPM

higher temperatures for the same level of stress. High temperatures cause copper conductors to soften and lead to an increase of deformation [164].

The stress of Kraft insulation paper at 25 °C and 125 °C is 37 Mpa with 0.14 % strain and 16 Mpa with 0.1 % strain as shown in Figure 4.33 (b). This indicates that the Kraft insulation paper can resist high stress at low temperatures and withstand less stress at higher temperatures. As temperature increases, Kraft insulation paper deforms easily under low stress. The structural steel fixed support experiences the same strain of 0.03% at 25°C and 125°C with corresponding stresses of 240 MPa and 140 MPa as shown in Figure 4.33 (c). The relationship between applied stress and strain for the structural steel fixed support is similar to copper conductors.

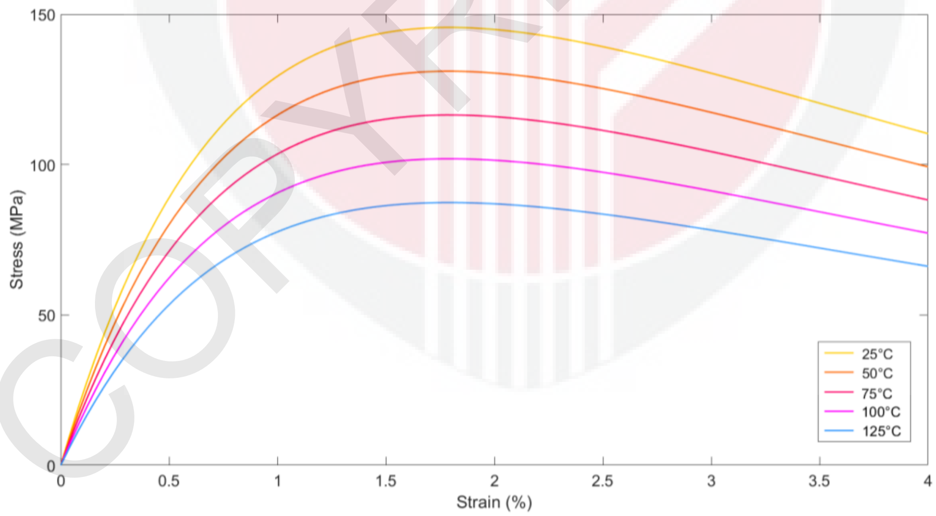

(a)

© COPYRIGHT UPM

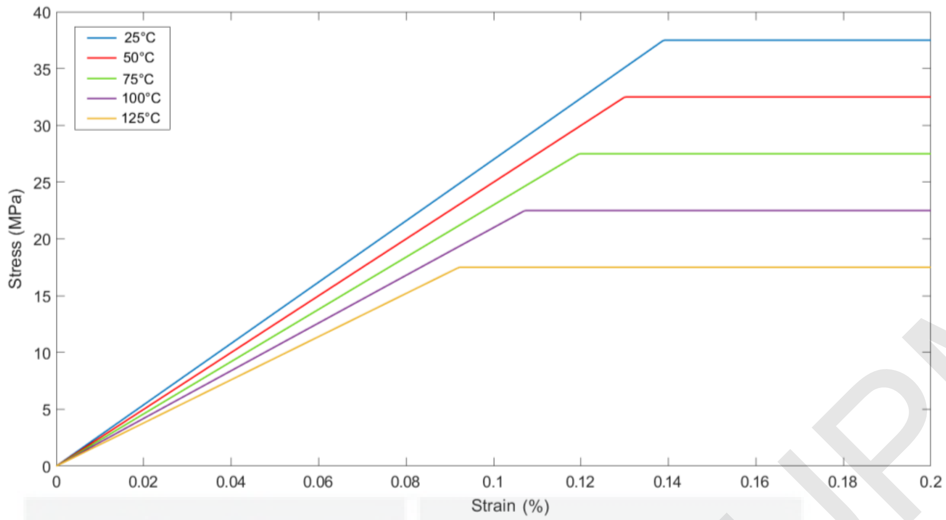

(b)

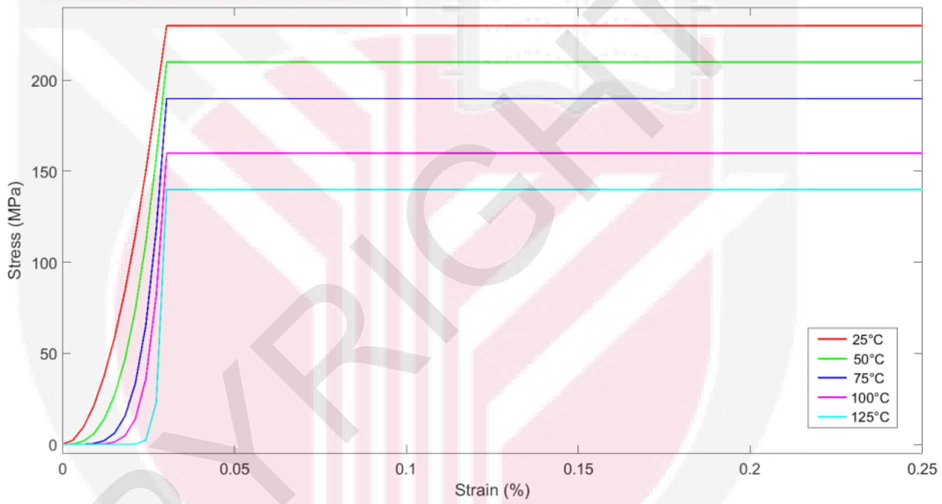

(c)

Figure 4.33: The relationship between stress and strain under different temperatures for (a) copper conductor, (b) kraft paper insulation and (c) structural fixed support of disc winding

4.5.3.2 The relationship between load and displacement of disc winding materials

The relationships between load and displacement for different disc winding materials under electromagnetic force are shown in Figure 4.34. Figure 4.34 (a) shows that the displacement of copper conductors increases linearly with

© COPYRIGHT UPM

the increment of load. This indicates that the copper conductor experiences high deformation at high electromagnetic force, which reflects the reduction of its stiffness and load-bearing capacity.

The Kraft insulation paper and structural steel fixed supports show similar trend of load and displacement as copper conductors. The Kraft insulation paper shows a more gradual response with lower maximum loads compared to copper conductors, as seen in Figure 4.34 (b). This indicates that it has a lower load-bearing capacity than copper conductors when under the same electromagnetic force. Figure 4.34 (c) shows that the structural steel fixed supports experience a high increase in load factors at low displacement. This indicates it has higher load-bearing capacity than copper conductors and structural steel fixed supports.

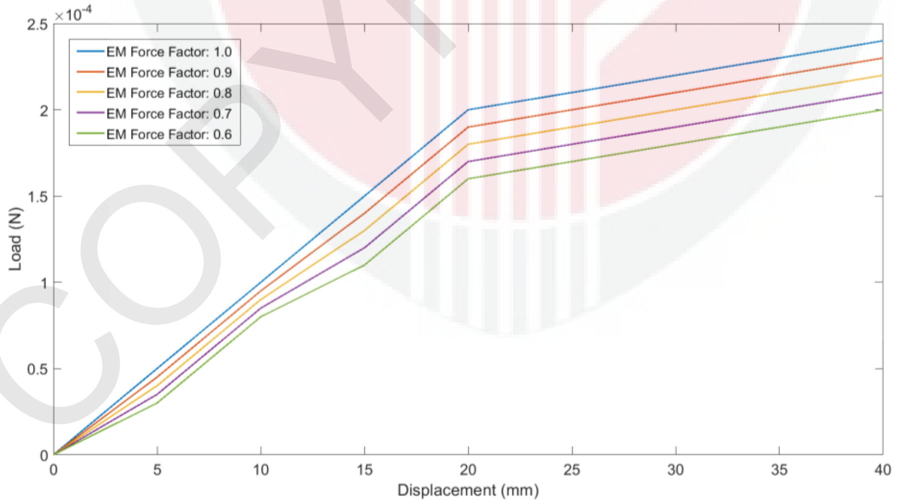

(a)

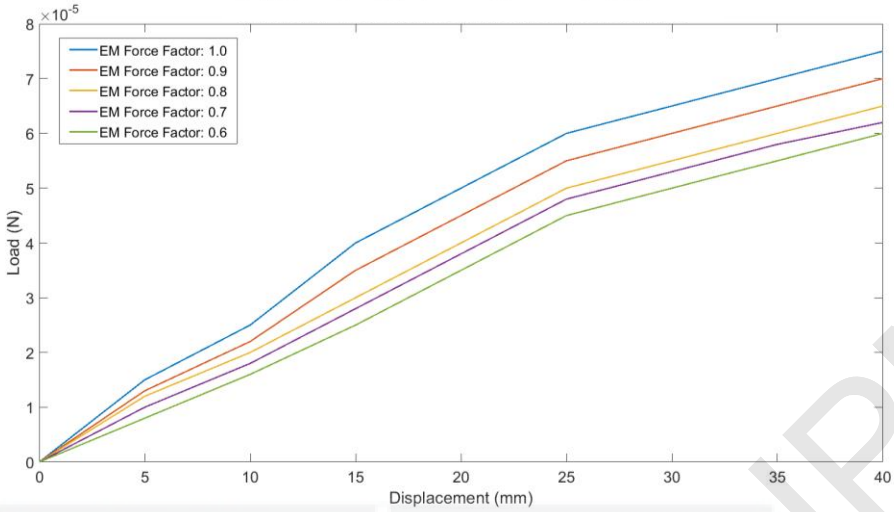

(b)

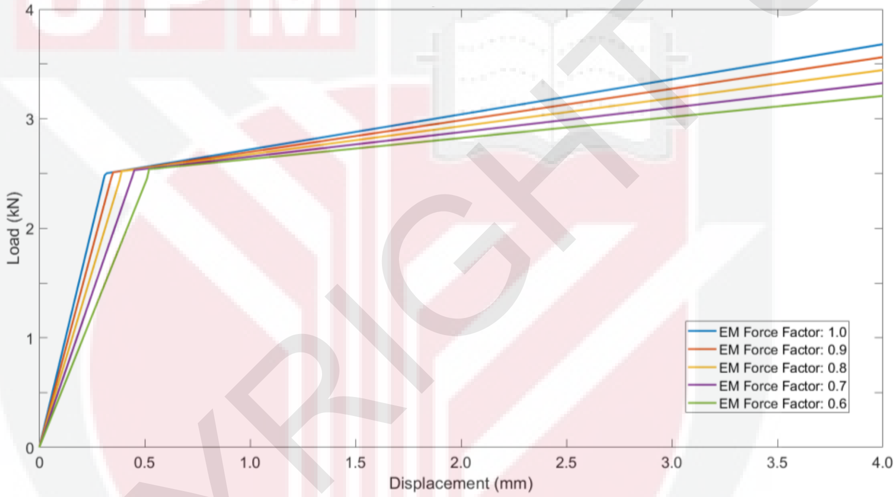

(c)

Figure 4.34: Relationship between load and displacement under different electromagnetic force for (a) copper conductors, (b) Kraft insulation paper and (c) structural steel fixed supports of disc winding

The relationships between load and displacement for different disc winding materials under temperature variations are shown in Figure 4.35. Figure 4.35 (a) shows that the peak load capacity of copper conductors decreases as the temperature increases. This indicates that as temperature increases, the load-bearing capacity of the copper conductor decreases and results in significant displacement. The Kraft insulation paper and structural steel fixed support in Figures 4.35 (b) and 4.35 (c) demonstrate a similar trend of load and

© COPYRIGHT UPM

displacement trends to copper conductors where high temperatures result in an increment of displacement. This occurs because the disc winding materials experience thermal softening as the temperature increases that leads to thermal expansion and causes displacement [89].

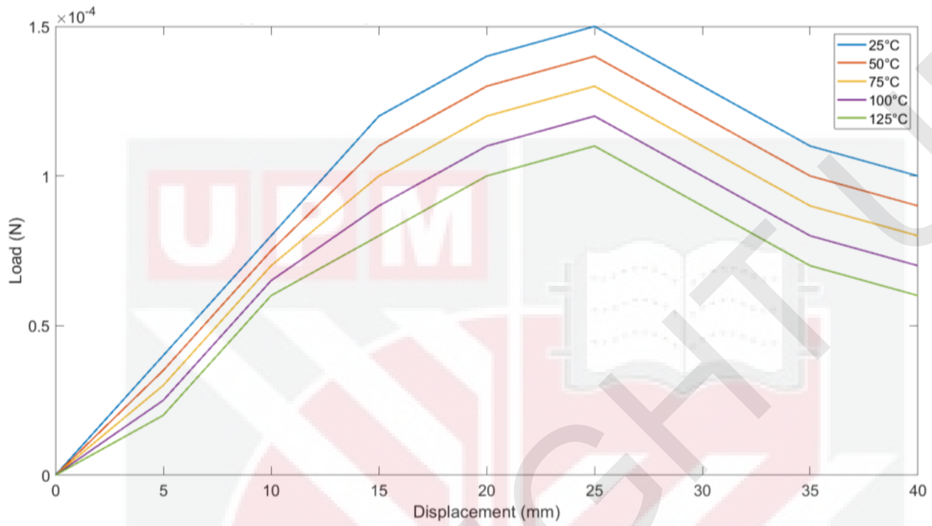

(a)

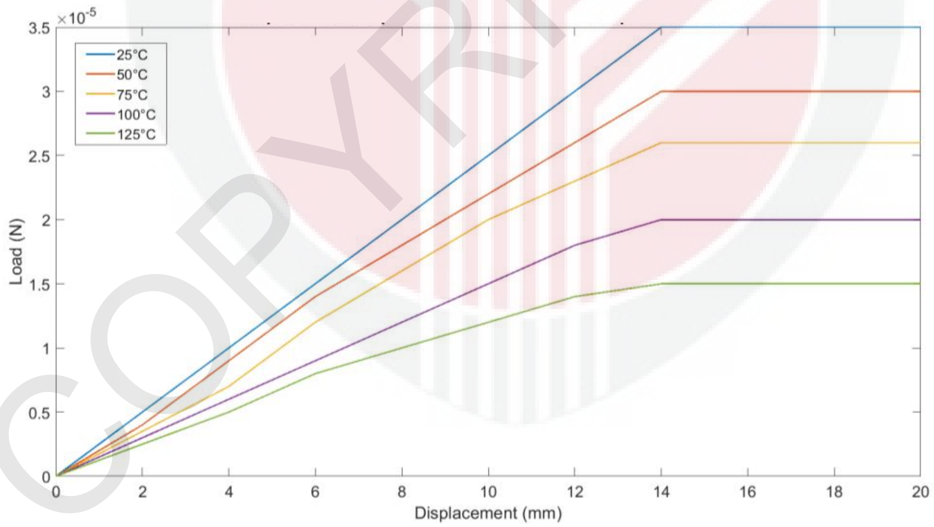

(b)

© COPYRIGHT UPM

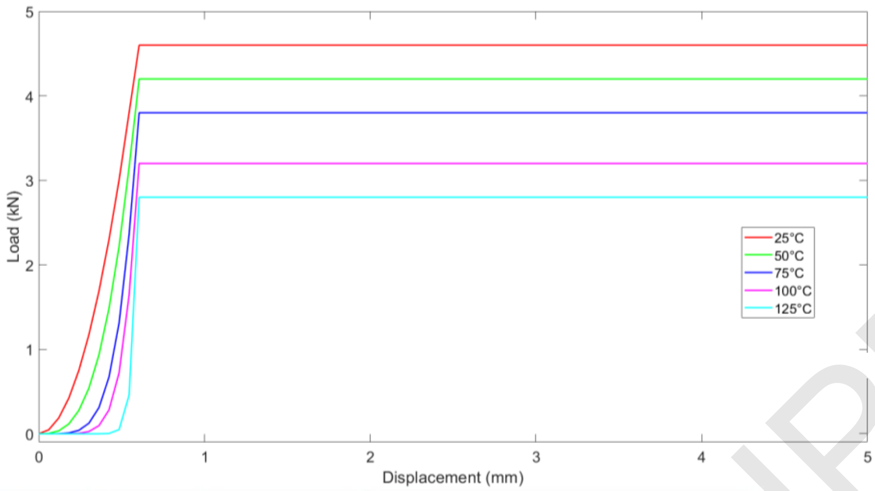

(c)

Figure 4.35: The relationship between load and displacement under different temperatures for (a) copper conductors, (b) Kraft insulation paper and (c) structural fixed support of disc winding

4.5.4 Safety factors of disc winding under standard switching impulse

Figure 4.36 shows the safety factor of the disc winding structure due to electromagnetic force and thermal effect under SSI voltage. The safety factor of disc winding under electromagnetic force is shown in Figure 4.36 (a), where most of the disc winding structures are well within the safe limit. The top disc layer of the winding is subjected to high localised stress with a low safety factor of 4.45. This is primarily due to the high impulse voltage at the top layers, where electromagnetic forces exert additional mechanical stress. The bottom disc layer and circumference experience moderate stress with large safety factors between 10 and 15.

The safety factor of the disc winding under thermal effect in Figure 4.36 (b) shows a low safety factor from 0 to 1 throughout the entire disc winding structure. This condition indicates that thermal stress causes significant stress

© COPYRIGHT UPM

concentration across all disc layers. The low safety factor is attributed to uneven thermal expansion, where temperature gradients create differential expansion rates between adjacent disc layers. As some regions expand more than others, mechanical strain accumulates and weakens the disc winding structural integrity.

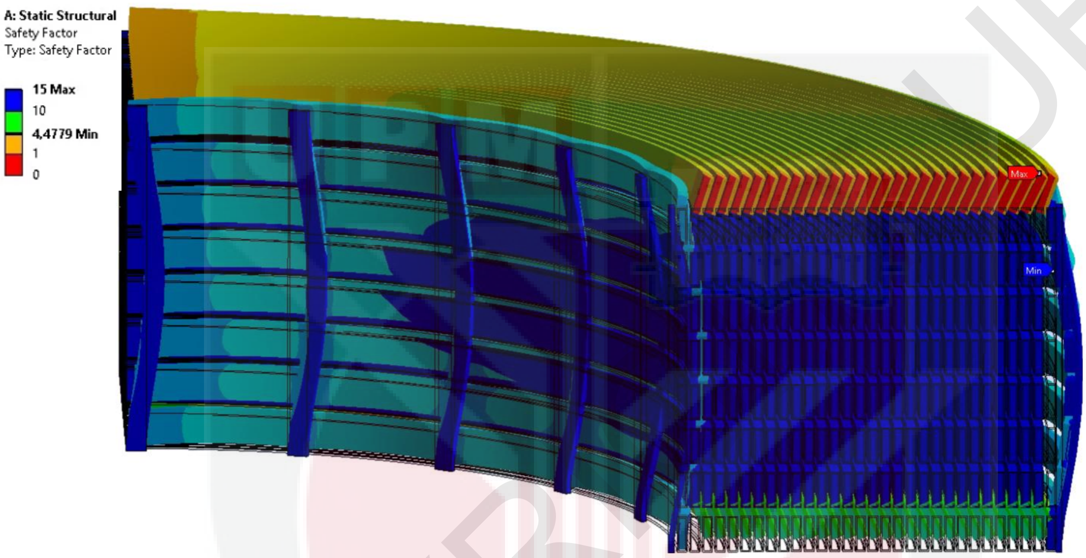

(a)

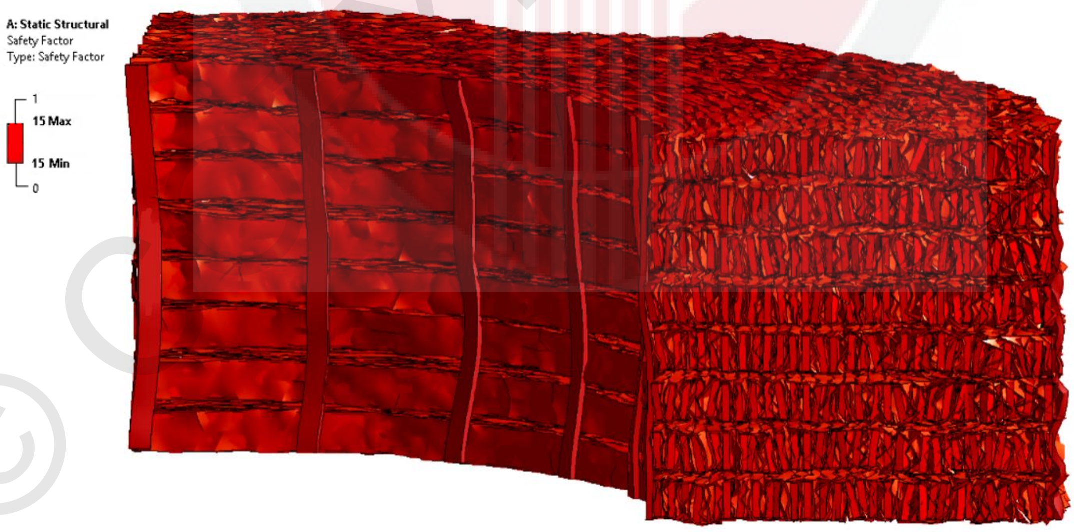

(b)

Figure 4.36: Simulation results of safety factors in the HV winding under (a) electromagnetic force and (b) thermal effect

4.6 Summary

The resonance due to the SSI voltage oscillates more uniformly as compared to due to the NSSI voltage. The resonance of NSSI voltage is pronounced and varied with high amplitudes and complex oscillations. It is observed that the pattern of resonance oscillations is influenced by the position of the disc, where top disc layers show pronounced resonance effects. Both SSI and NSSI voltages cause significant axial force, with NSSI voltage shows a broad range of force magnitudes.

For the electric transient analysis, the ohmic losses are found unevenly distributed, with high concentrations at the outermost disc layers, especially towards the edges of winding and the topmost disc layer. The thermal transient analysis shows high heat flux and temperature distribution at the outer disc layers. The structural analysis of Kraft insulation paper shows significant deformation, with signs of wrinkle, distortion and tear. The copper conductor displays signs of restraint expansion as it shows wavy bends. The restrained expansion of the copper conductors causes pressure exerted on the fixed supports, especially at the contact points and results in bends.

The buckling analysis under electromagnetic force caused localised instability, particularly in the circumferences and outer disc layers. Thermal dependent buckling analysis causes global instability in the overall disc winding structure. The stress-strain analysis shows that copper conductors and structural steel fixed supports exhibit a high strain rate at high electromagnetic forces. Kraft insulation paper becomes brittle and loses strength after it reaches a certain strain level. As temperature increases, the ability of copper conductors, Kraft insulation paper, and

© COPYRIGHT UPM

structural steel fixed supports to withstand stress decreases, which makes the materials deform more easily.

All materials exhibit similar behaviour under thermal loads, in which high temperatures result in low load-bearing capacity and greater displacement due to thermal softening and expansion. The safety factor analysis shows that the disc winding structure remains mostly within safe limits under electromagnetic force, except for the top disc layer with a low safety factor of 4.45. Under thermal effects, the entire disc winding structure experiences significant stress with a low safety factor ranging from 0 to 1.

© COPYRIGHT UPM

CHAPTER 5

CONCLUSIONS AND RECOMMENDATIONS

5.1 Introduction

This chapter presents the conclusion and recommendations/future works based on the research on the cumulative impact of switching impulses on disc-type transformer windings through the Finite Element Method (FEM). All objectives are successfully met through FEM analysis.

5.2 Conclusion

The electromagnetic force behaviours generated within a disc winding during switching transients are examined as the first objective of study. The RLC equivalent circuit analysis reveals significant differences between the resonances of Standard Switching Impulse (SSI) and Non-Standard Switching Impulse (NSSI) voltages. The SSI voltage exhibits uniform oscillations, while the NSSI voltage shows complex oscillations with high amplitudes as it propagates through the disc layers. It is found that the position of the disc layer affects the pattern of oscillations. Pronounced resonance effects are at the top disc layer due to its proximity to the impulse injection point. The FEM analysis reveals that both SSI and NSSI voltages lead to significant axial force on the disc winding compared to radial force, with broad ranges of force magnitudes for NSSI voltage. The SSI voltage causes localised hoop tension, axial

© COPYRIGHT UPM

displacement and tilt of conductors, particularly at the outer layers of the disc winding. The NSSI leads to widespread deformations throughout the disc winding structure which can cause global structural deformation under extreme conditions. Based on the structural deformation analysis, the deformation and displacement caused by NSSI voltage are more apparent as compared to SSI voltage.

The interrelated response of electrical, thermal and structural aspects of the disc winding under SSI voltage is evaluated as the second objective of study. The electric transient analysis reveals that the distribution of ohmic losses is non-uniform throughout the disc winding. High ohmic losses are observed at the outer circumference and topmost disc layers. Thermal analysis demonstrates that the uneven distribution of ohmic losses results in a significant rise in temperature, with hot-spot temperatures reached 428.6 °C. The structural analysis shows that the copper conductors experience thermal expansion, which causes noticeable wavy bends that lead to misalignment. As the structural steel fixed supports restrain the expansion of the copper conductors, substantial pressure is exerted. This condition causes the fixed support to bend at the contact points. The Kraft insulation paper experiences significant deformation with clear signs of wrinkles, distortion and tear due to stresses caused by the deformed copper conductors under the thermal stress.

The disc winding mechanical response and structural stability under the effects of electromagnetic force and thermal stress due to recurrent switching transient is evaluated as the third objective of the study. The structural stability

© COPYRIGHT UPM

through buckling analysis shows that the electromagnetic force causes localised instability at the topmost disc layers and outer circumferences of the disc winding. The thermal stress induces widespread deformation across the disc winding structure, which leads to global instability. The stress-strain analysis shows that copper conductors and structural steel fixed supports exhibit high strain rates under high electromagnetic forces, while Kraft insulation paper becomes brittle once a certain strain level is reached. High temperature decreases the yield strength and increases the strain rate for copper conductors and structural steel fixed supports, make them more susceptible to deformation. Kraft insulation paper maintains high yield strength at elevated temperatures before it is subjected to permanent deformation. The safety factor analysis under electromagnetic force shows that most parts of the disc winding remain within safe operational limits. However, the top and bottom disc layers, including the outer circumference exhibit lower to moderate safety factors. The entire disc winding structure exhibits low safety factors under thermal effects which indicate a significant risk of global failure.

In conclusion, this study demonstrates that the cumulative switching impulse voltages can significantly impact the electromagnetic force, thermal and structural characteristics of a disc winding. The finding emphasises the importance of considering both electromagnetic force and thermal effects in the design and analysis of transformer windings to ensure long-term stability and reliability under recurrent switching transients.

© COPYRIGHT UPM

5.3 Recommendations and future works

Based on this study, several recommendations for future research are identified and proposed as follows:

While FEM simulations provide valuable insights, experimental validation of the findings is crucial to verify the accuracy of the findings. Future research should conduct high voltage impulse tests on actual transformer windings to study the electromagnetic force and thermal effects. By comparing experimental results with FEM simulations, potential discrepancies can be identified and addressed, leads to improved modelling techniques and more reliable predictive capabilities for transformer behaviour under switching impulses. The analysis could be expanded to examine different transformer windings configurations such as layer, helical and interleaved windings under similar conditions. Comparative studies will provide a deeper understanding of winding performance, aiding in the selection of optimal designs for high-voltage applications.

Future research should integrate multi-physics coupling that includes fluid dynamics to analyse the effect of oil-based cooling system. Study on how cooling mechanisms influence winding temperature distribution and structural deformation is crucial to improve transformer cooling strategies. By incorporating computational fluid dynamics (CFD) into FEM simulations, future studies can evaluate the convective heat transfer properties of transformer oil and assess its efficiency in reducing thermal stress. Additionally, the

© COPYRIGHT UPM

interaction between oil flow, electromagnetic forces and structural deformation could be analysed to identify potential weaknesses in transformer cooling designs. Understanding these complex interactions will help develop more effective cooling solutions, preventing overheating, reducing insulation degradation and ultimately enhance transformer lifespan and reliability.

Finally, as switching impulses can cause cumulative damage to transformer windings, making real-time monitoring essential for early fault detection. Future research should focus on developing predictive maintenance strategies specifically tailored for switching impulse-induced stresses. High-precision sensors should be integrated into transformers to measure impulse-related parameters such as transient voltage spikes, electromagnetic force fluctuations and localised thermal stress. These sensors, when connected to an Internet of Things (IoT)-based framework, can enable continuous condition monitoring and provide early warning signals for impulse-related anomalies. Additionally, machine learning and artificial intelligence (AI) algorithms can be applied to analyse historical data, detect switching impulse patterns and predict potential transformer failures. Implementing such predictive maintenance strategies can significantly enhance transformer reliability, minimise unplanned downtime and optimise maintenance schedules to extend the lifespan of transformers.

© COPYRIGHT UPM

REFERENCES

[1] IEEE, "IEEE Standard Terminology for Power and Distribution Transformers," Nov. 2002 doi: 10.1109/IEEESTD.2002.94146.

[2] S. Chakravorti, D. Dey, and B. Chatterjee, *Recent Trends in the Condition Monitoring of Transformers: Theory, Implementation and Analysis*, vol. 67. 2013. doi: 10.1007/978-1-4471-5550-8.

[3] Joint Working A2/C4.39, "Electrical Transient Interaction Between Transformer and the Power System, Part-1: Expertise," 2014.

[4] A. Da Costa Oliveira Rocha, A. Holdyk, B. Gustavsen, B. J. Van Jaarsveld, A. Portillo, and B. Badrazadeh, "Electrical Transient Interaction Between Transformer and the Power System, Part-2: Case studies, JWG A2/C4.39," 2014. [Online]. Available: https://e-cigre.org/publication/577B-electrical-transient-interaction-between-transformers-and-the-power-system-part-2-case-studies

[5] U. R. R. Massaro and R. Antunes, "Electrical Transient Interaction between Transformers and Power System - Brazilian Experience," *42nd Int. Conf. Large High Volt. Electr. Syst. 2008, CIGRE 2008*, vol. 3, no. 6, pp. 1–9, 2009, [Online]. Available: https://api.semanticscholar.org/CorpusID:201037091

[6] M. Hori, M. Nishioka, Y. Ikeda, K. Noguchi, K. Kajimura, and H. Motoyama, "Internal winding failure due to resonance overvoltage in distribution transformer caused by winter lightning," *2006 IEEE Power Eng. Soc. Gen. Meet. PES*, vol. 21, no. 3, pp. 1600–1606, 2006, doi: 10.1109/pes.2006.1708981.

[7] S. Tenbohlen, J. Jagers, and F. Vahidi, "Standardized survey of transformer reliability: On behalf of CIGRE WG A2.37," *Proc. Int. Symp. Electr. Insul. Mater.*, vol. 2, no. 1, pp. 593–596, 2017, doi: 10.23919/ISEIM.2017.8166559.

[8] G. D. Hermann, "Short-Circuit Withstand Capability of Power Transformers," in *Karlsruhe Institute of Technology*, vol. 49, 2015, pp. 1–10.

[9] M. Zile, "Routine Test Analysis in Power Transformers by Using Firefly Algorithm and Computer Program," *IEEE Access*, vol. 7, pp. 132033–132040, 2019, doi: 10.1109/ACCESS.2019.2939764.

[10] S. Urooj, T. Singh, M. Amir, and M. Tariq, "Optimal Design of Power Transformer with Advance Core Material using ANSYS Technique," *Eur. J. Electr. Eng. Comput. Sci.*, vol. 4, no. 5, 2020, doi: 10.24018/ejece.2020.4.5.249.

[11] M. A. Rao, M. R. Khanna, K. J. Somaiya, and M. Gangopadhyay,

© COPYRIGHT UPM

"Applications of Finite Elements Method (FEM) - An Overview," *Int. Conf. Math. Sci.*, vol. 28, no. 31, pp. 1–8, 2012, doi: 10.13140/RG.2.2.36294.42565.

[12] S. S. Rao, "Overview of Finite Element Method," in *The Finite Element Method in Engineering*, Elsevier, 2005, pp. 3–45. doi: 10.1016/B978-0-7506-7828-5.X5000-8.

[13] X. Yan, X. Yu, M. Shen, D. Xie, B. Bai, and Y. Wang, "Calculation of stray losses in power transformer structural parts using finite element method combined with analytical method," *Int. Conf. Electr. Mach. Syst.*, pp. 320–324, 2016, doi: 10.1109/ICEMS.2015.7385051.

[14] S. Hasan, S. Taib, S. Hardi, A. Rahim, and A. Shukri, "Core loss characteristics analysis of power transformer under different frequencies excitation," *Proc. 2013 IEEE 7th Int. Power Eng. Optim. Conf. PEOCO 2013*, no. June, pp. 619–623, 2013, doi: 10.1109/PEOCO.2013.6564622.

[15] Shutterstock, "3D High Voltage Power Distribution Transformer," *TurboSquid*, 2024. https://www.turbosquid.com/Search/3D-Models/transformer

[16] S. D. Chaitkin, "No-load versus load loss," *IEEE Industry Applications Magazine*, pp. 21–28, 2003.

[17] H. R. and T. S. G. (D-8450), "US Department of the interior bureau of reclamation: Transformer Maintenance, facilities instructions, standards, and techniques," 2000. doi: 10.1109/EIC.1975.7458540.

[18] J. Sanchez, "Classic Power Transformer Windings," *Technology*, pp. 9–13, 2019. [Online]. Available: www.transformers-magazine.com

[19] A. S. Murthy, N. Azis, J. Jasni, M. L. Othman, M. F. M. Yousof, and M. A. Talib, "Effect of shield placement for transient voltage mitigation due to switching surges in a 33/11 kV transformer windings," *PLoS One*, vol. 15, no. 10, 2020, doi: 10.1371/journal.pone.0240368.

[20] M. Daghrah, "Experimental Study of Transformer Liquid Flow and Temperature Distributions," 2017.

[21] K. D. Choi, W.-C. Kim, Y. Y. Hwang, and S.-H. Lee, "Continuous disk winding for high voltage superconducting transformer," 2007

[22] J. C. Olivares-Galván, F. De León, P. S. Georgilakis, and R. Escarela-Pérez, "Selection of copper against aluminium windings for distribution transformers," *IET Electr. Power Appl.*, vol. 4, no. 6, pp. 474–485, 2010, doi: 10.1049/iet-epa.2009.0297.

[23] H. Rebecca, "Cellulose-based electrical insulation materials. Dielectric and mechanical properties," 2017.

© COPYRIGHT UPM

[24] B. Li, J. He, Y. Li, and Y. Zheng, “Overvoltage,” *Prot. Technol. Ultra-High-Voltage AC Transm. Syst.*, pp. 149–162, Jan. 2020, doi: 10.1016/B978-0-12-816205-7.00009-1.

[25] D. Thukaram, H. P. Khincha, and S. Khandelwal, “Estimation of switching transient peak overvoltages during transmission line energization using artificial neural network,” *Electric Power Systems Research*, vol. 76, no. 4. pp. 259–269, 2006. doi: 10.1016/j.epsr.2005.07.001.

[26] E. Bjerkan, “High frequency modeling of power transformers - Stresses and Diagnostic,” Doctoral dissertation, Norwegian University of Science and Technology, 2005.

[27] U. Massaro and R. Antunes, “Electrical transient interaction between transformers and power system–Brazilian experience,” *Int. Conf. Power Syst. Transients (IPST2009), Kyoto, Japan*, vol. 3, no. 6, pp. 1–9, 2009, [Online]. Available: http://www.ipst.org/techpapers/2009/papers/257.pdf

[28] J. Furgał, M. Kuniewski, and P. Paja¸k, “Analysis of internal overvoltages in transformer windings during transients in electrical networks,” *Energies*, vol. 13, no. 10, 2020, doi: 10.3390/en13102644.

[29] J. J. Smit, “Over voltage in electrical power system,” 2017.

[30] M. S. Naidu and V. Kamaraju, *High Voltage Engineering*. 1996.

[31] V. Lackovic, “Introduction to Switching Transients Analysis Fundamentals,” 2019. [Online]. Available: info@cedengineering.com

[32] D. D. Shipp, T. J. Dionise, V. Lorch, and B. G. MacFarlane, “Transformer failure due to circuit-breaker-induced switching transients,” *IEEE Trans. Ind. Appl.*, vol. 47, no. 2, pp. 707–718, 2011, doi: 10.1109/TIA.2010.2101996.

[33] M. Arthur, M. Joseph, F. Reto, M. Jim, P. Bertrand, and R. Pierre, “IEEE Guide for Transformer Impulse Tests,” New York, 2012.

[34] J. A. Martinez-Velasco, *Power System Transients : Parameter Determination*, Second. CRC press, 2010.

[35] B. Filipović-Grčić and D. Filipović-Grčić, “A new method for estimation of time parameters of standard and non-standard switching impulse voltages,” *Int. J. Electr. Power Energy Syst.*, vol. 96, no. August 2017, pp. 126–131, 2018, doi: 10.1016/j.ijepes.2017.10.001.

[36] A. Das Gupta, Hisham-Al-Rashid, and A. F. Faiyaz, “Study and analysis of switching transients in high voltage transmission line from Barapukuria to Bibiyana of Bangladesh,” *Int. Conf. Energy Power Eng. Power Progress, ICEPE 2019*, pp. 1–5, 2019, doi: 10.1109/CEPE.2019.8726840.

© COPYRIGHT UPM

[37] K. C. Agrawal, “Surge Arresters: Application and Selection,” in *Industrial Power Engineering Handbook*, vol. 18, 2001, pp. 587–625. doi: 10.1016/b978-075067351-8/50096-9.

[38] D. C. McDermit, D. D. Shipp, T. J. Dionise, and V. Lorch, “Medium-voltage switching transient-induced potential transformer failures: Prediction, measurement, and practical solutions,” *IEEE Trans. Ind. Appl.*, vol. 49, no. 4, pp. 1726–1736, 2013, doi: 10.1109/TIA.2013.2258453.

[39] S. S. Kandil, P. S. P. El-sewedy, and A. M. Ibrahim, “Multiple-Arm Passive Filters Design Based on Different Reactive Power Sharing Approaches,” *Power Syst. Conf. (MEPCON), IEEE*, pp. 147–155, 2016, doi: 978-1-4673-9063-7/16.

[40] K. C. Agrawal, “Surge Arresters: Application and Selection,” in *Industrial Power Engineering Handbook*, vol. 18, Butterworth-Heinemann, 2001, pp. 681–719. doi: 10.1016/b978-075067351-8/50096-9.

[41] M. Florkowski, J. Furgał, and M. Kuniewski, “Propagation of overvoltages in the form of impulse, chopped and oscillating waveforms in transformer windings—Time and frequency domain approach,” *Energies*, vol. 13, no. 2, pp. 1–17, 2020, doi: 10.3390/en13020304.

[42] D. Smugała, W. Piasecki, M. Ostrogorska, M. Florkowski, M. Fulczyk, and P. Kłys, “Distribution transformers protection against high frequency switching transients,” *Prz. Elektrotechniczny*, vol. 88, no. 5 A, pp. 296–300, 2012.

[43] S. V. Kulkarni and S. A. Khaparde, *Transformer Engineering: Design, Technology and Diagnostics*, Second. CRC press, 2017. doi: 10.1201/b13011.

[44] J. M. Weed, “Abnormal voltages in transformers,” *Proc. Am. Inst. Electr. Eng.*, vol. 34, no. 8, pp. 1621–1656, 1915, doi: 10.1109/paiee.1915.6590780.

[45] H. Sun, G. Liang, X. Zhang, and X. Cui, “Analysis of resonance in transformer windings under very fast transient overvoltages,” *17th Int. Zurich Symp. Electromagn. Compat. 2006*, vol. 2006, no. 1, pp. 432–435, 2006, doi: 10.1109/emczur.2006.214964.

[46] A. R. M. de Sousa, M. V. A. Nunes, W. da S. Fonseca, R. C. F. Araujo, and D. de S. Lima, “Magneto-thermo-structural analysis of power transformers under inrush and short circuit conditions,” *Energies*, vol. 14, no. 11, pp. 1–19, 2021, doi: 10.3390/en14113266.

[47] V. Nurmanova, M. Bagheri, A. Zollanvari, K. Aliakhmet, Y. Akhmetov, and G. B. Gharehpetian, “A New Transformer FRA Measurement Technique to Reach Smart Interpretation for Inter-Disk Faults,” *IEEE Trans. Power Deliv.*, vol. 34, no. 4, pp. 1508–1519, 2019, doi: 10.1109/TPWRD.2019.2909144.

© COPYRIGHT UPM

[48] Q. Ou, L. Luo, Y. Li, Y. Lin, and Y. Tian, “A dynamic relative displacement evaluation method for extra-high voltage transformer withstanding short-circuit impact,” *IET Gener. Transm. Distrib.*, vol. 17, no. 6, pp. 1310–1320, 2022, doi: 10.1049/gtd2.12736.

[49] M. Gutten, J. J. U. R. Č. Ik, M. Brandt, and R. Polansky, “Mechanical effects of short-circuit currents analysis on autotransformer windings,” *Electr. Eng.*, vol. 87, no. 7, pp. 272–275, 2011, [Online]. Available: http://pe.org.pl/articles/2011/7/62.pdf

[50] M. Tahir and S. Tenbohlen, “A comprehensive analysis of windings electrical and mechanical faults using a high-frequency model,” *Energies*, vol. 13, no. 1, 2019, doi: 10.3390/en13010105.

[51] M. Bagheri, M. Naderi, and T. Blackburn, “Advanced transformer winding deformation diagnosis: Moving from off-line to on-line,” *IEEE Trans. Dielectr. Electr. Insul.*, vol. 19, no. 6, pp. 1860–1870, 2012, doi: 10.1109/TDEI.2012.6396941.

[52] M. Bagheri, “Transformer Winding Deformation and Insulation Characteristic Effects on Frequency Response Analysis,” *Doctor of Philosophy thesis, University of New South Wales*. pp. 18–24, 2014.

[53] M. Bagheri, M. S. Naderi, T. Blackburn, and T. Phung, “FRA vs. short circuit impedance measurement in detection of mechanical defects within large power transformer,” *Conf. Rec. IEEE Int. Symp. Electr. Insul.*, vol. 224, pp. 301–305, 2012, doi: 10.1109/ELINSL.2012.6251477.

[54] W. M. L. B. Naranpanawe, “Understanding the Moisture Temperature and Ageing Dependency of Power Transformer Winding Clamping Pressure,” 2018.

[55] I. Z. F. bin Hussien, A. A. Rahim, and N. Abdullah, “Electric power transmission,” *Power Electron. Handb.*, vol. 3000, pp. 1357–1374, 2011, doi: 10.1016/B978-0-12-382036-5.00047-1.

[56] Transformer Committee, “IEEE Guide for Transformer Impulse Tests,” 1993.

[57] Transformer Committee, “IEEE Std C57.98-2011: Guide for Transformer Impulse Tests,” 2011.

[58] Matthew N.O. Sadiku, *Elements of Electromagnetics*, Seventh. Oxford University Press, 2018.

[59] G. N. T. Farouk A.M Rizk, *High Voltage Engineering*, vol. 53, no. 9. 2017.

[60] L. Weidong, L. Shanghe, and H. Xiaofeng, “Transient electric field measurement system analysis and optimization design,” in *2013 International Workshop on Microwave and Millimeter Wave Circuits and System Technology*, Oct. 2013, pp. 1–4. doi:

© COPYRIGHT UPM

10.1109/MMWCST.2013.6814524.

[61] J. A. Martinez, D. Goldsworthy, and R. Horton, “Switching Overvoltage Measurements and Simulations—Part I: Field Test Overvoltage Measurements,” *IEEE Trans. Power Deliv.*, vol. 29, no. 6, pp. 2502–2509, 2014, doi: 10.1109/TPWRD.2014.2303575.

[62] Q. Fengyun, C. Jia, L. Yu, W. Yu, and H. Wangling, “Calculation and Analysis of Transformer Transient Over-Voltage in no- Load Switching,” *2nd Int. Conf. Adv. Mater. Mechatronics Civ. Eng. (ICAMMCE 2017)*, vol. 121, no. 1, pp. 1–9, 2017, [Online]. Available: http://creativecommons.org/licenses/by-nc/4.0/

[63] A. Hayati Soloot, A. Gholami, E. Agheb, A. Ghorbandaeipour, and P. Mokhtari, “Investigation of Transmission Line Overvoltages and their Deduction Approach,” *Innternational J. Electr. Electron. Eng. 2010*, vol. 3, no. 5, pp. 18–26, 2009, doi: doi.org/10.5281/zenodo.1072429.

[64] D. D. Shipp, T. J. Dionise, and V. Lorch, “Transformer failure due to circuit breaker induced switching transients appplicable to the cement industry,” *IEEE Trans. Ind. Appl.*, vol. 47, no. 2, pp. 707–717, 2011, doi: 10.1109/CITCON.2013.6525287.

[65] A. A. Taheri, A. Abdali, and A. Rabiee, “Indoor distribution transformers oil temperature prediction using new electro-thermal resistance model and normal cyclic overloading strategy: an experimental case study,” *IET Gener. Transm. Distrib.*, vol. 14, no. 24, pp. 5816–5822, 2020, doi: 10.1049/iet-gtd.2020.0457.

[66] P. A. Abetti, “Survey and Classification of Published Data on the Surge Performance of Transformer and Rotating Machines,” *Trans. Am. Inst. Electr. Eng. Part III Power Appar. Syst.*, vol. 77, no. 3, pp. 1403–1413, 1958, doi: 10.1109/AIEEPAS.1958.4500166.

[67] V. Jalili-Marandi, V. Dinavahi, K. Strunz, J. A. Martinez, and A. Ramirez, “Interfacing techniques for transient stability and electromagnetic transient programs: IEEE task force on interfacing techniques for simulation tools,” *IEEE Trans. Power Deliv.*, vol. 24, no. 4, pp. 2385–2395, 2009, doi: 10.1109/TPWRD.2008.2002889.

[68] IEEE Electromagnetic Compatibility Society, *IEEE Recommended Practice for Validation of Computational Electromagnetics Computer Modeling and Simulations*. 2011.

[69] H. Al-Sheikh and N. Moubayed, “An overview of simulation tools for renewable applications in power systems,” *2012 2nd Int. Conf. Adv. Comput. Tools Eng. Appl. ACTEA 2012*, pp. 257–261, 2012, doi: 10.1109/ICTEA.2012.6462878.

[70] J. A. Martinez-Velasco, J. Jatskevich, S. Filizadeh, M. Popov, M. Rioual, and J. L. Naredo, “Power System Transients - Modeling of Power Components for Transient Analysis,” *Encyclopaedia of Life Support*

© COPYRIGHT UPM

Systems (EOLSS). pp. 1–45, 2018. [Online]. Available: https://www.eolss.net/sample-chapters/C05/E6-39-59-02.pdf

[71] K. K. Palueff, "Effect of Transient Voltages on Power Transformer Design," *Trans. Am. Inst. Electr. Eng.*, vol. 48, no. 3, pp. 681–701, 1929, doi: 10.1109/T-AIEE.1931.5055872.

[72] International Commission Electrotechnical, "IEC 60076-4 (2002) - Guide to the lightning impulse & switching impulse testing," 2012.

[73] R. Rudenberg, "Performance of traveling waves in coils and windings," *Electr. Eng.*, vol. 59, no. 12, pp. 1031–1040, 1940, doi: 10.1109/ee.1940.6435277.

[74] Y. Shibuya, S. Fujita, and E. Tamaki, "Analysis of Very Fast Transient Overvoltage in Transformer Winding," *IEE Proceedings-Generation, Transm. …*, vol. 148, no. 5, pp. 377–383, 2001, doi: 10.1049/ip-gtd.

[75] N. Bowler, "Frequency-dependence of relative permeability in steel," *AIP Conf. Proc.*, vol. 820 II, no. March 2006, pp. 1269–1276, 2006, doi: 10.1063/1.2184670.

[76] A. S. Murthy, "Frequency Response of Transformer Winding Deformation Based on Finite Element Modeling Under Transient Overvoltage Impulses," Ph.D dissertation, Dept. Elect. and Elec. Eng., Universiti Putra Malaysia, 2020.

[77] A. S. Murthy, N. Azis, M. F. Mohd Yousof, J. Jasni, M. L. Othman, and M. A. Talib, "Investigation on the resonant oscillations in an 11 kV distribution transformer under standard and chopped lightning impulse overvoltages with different shield placement configurations," *Energies*, vol. 12, no. 8, pp. 1–20, 2019, doi: 10.3390/en12081466.

[78] H. B. Zaninelli and E. C. Bortoni, "Optimized Modeling Process for Air Core Reactors using Finite Element Analysis," *IEEE Power Energy Soc. Gen. Meet.*, vol. 2021-July, pp. 1–5, 2021, doi: 10.1109/PESGM46819.2021.9638197.

[79] E. Schmidt, "Finite element analysis of electrical machines and transformers: State of the art and future trends," *COMPEL - Int. J. Comput. Math. Electr. Electron. Eng.*, vol. 30, no. 6, pp. 1899–1913, 2011, doi: 10.1108/03321641111168183.

[80] A. Santisteban, F. Delgado, A. Ortiz, I. Fernandez, C. J. Renedo, and F. Ortiz, "Numerical analysis of the hot-spot temperature of a power transformer with alternative dielectric liquids," *IEEE Trans. Dielectr. Electr. Insul.*, vol. 24, no. 5, pp. 3226–3235, 2017, doi: 10.1109/TDEI.2017.006228.

[81] S. Wang, H. Zhang, S. Wang, H. Li, and D. Yuan, "Cumulative Deformation Analysis for Transformer Winding Under Short-Circuit Fault Using Magnetic – Structural Coupling Model," *IEEE Trans. Appl.*

© COPYRIGHT UPM

Supercond., vol. 26, no. 7, pp. 1–5, 2016, doi: 10.1109/TASC.2016.2584984.

[82] I. J. Jebur and K. R. Hameed, “Evaluation and improvement of the main insulation structure of 33kV distribution transformer based on FEM,” *Indones. J. Electr. Eng. Comput. Sci.*, vol. 15, no. 1, pp. 36–47, 2019, doi: 10.11591/ijeecs.v15.i1.pp36-47.

[83] A. Khaligh and M. Vakilian, “Power Transformers Internal Insulation Design Improvements Using Electric Field Analysis Through Finite-Element Methods,” *IEEE Trans. Magn.*, vol. 44, no. 2, pp. 273–278, 2008, doi: 10.1109/TMAG.2007.912771.

[84] M. Mikha-Beyranvand, J. Faiz, B. Rezaeealam, A. Rezaei-Zare, and M. Jafarboland, “Thermal analysis of power transformers under unbalanced supply voltage,” *IET Electr. Power Appl.*, vol. 13, no. 4, pp. 503–512, 2019, doi: 10.1049/iet-epa.2018.5799.

[85] R. Gong, J. Ruan, J. Chen, Y. Quan, J. Wang, and S. Jin, “A 3-D coupled magneto-fluid-thermal analysis of a 220 kV three-phase three-limb transformer under DC bias,” *Energies*, vol. 10, no. 4, 2017, doi: 10.3390/en10040422.

[86] J. Wang, Y. Li, P. Li, X. Wang, Z. Yu, and T. Meng, “Analysis of temperature characteristics of power transformer withstand short circuit shock for two seconds,” *Energy Reports*, vol. 9, pp. 1049–1059, 2023, doi: 10.1016/j.egyr.2023.05.210.

[87] W. S. Fonseca, D. S. Lima, A. K. F. Lima, M. V. A. Nunes, U. H. Bezerra, and N. S. Soeiro, “Analysis of Structural Behavior of Transformer’s Winding under Inrush Current Conditions,” *IEEE Trans. Ind. Appl.*, vol. 54, no. 3, pp. 2285–2294, 2018, doi: 10.1109/TIA.2018.2808273.

[88] H. Kojima, H. Miyata, S. Shida, and K. Okuyama, “Buckling Strength Analysis of Large Power Transformer Winding Subjected To Electromagnetic Force Under Short Circuit,” *IEEE Trans. power Appar. Syst.*, vol. PAS-99, no. 3, pp. 1288–1297, 1980, doi: 10.1109/TPAS.1980.319761.

[89] L. Naranpanawe and C. Ekanayake, “Applications of FEM in condition monitoring of transformer clamping system,” *2017 Australas. Univ. Power Eng. Conf. AUPEC 2017*, vol. 2017-Novem, pp. 1–6, 2018, doi: 10.1109/AUPEC.2017.8282419.

[90] A. Ahmad, I. Javed, W. Nazar, and M. A. Mukhtar, “Short Circuit Stress Analysis Using FEM in Power Transformer on H-V Winding Displaced Vertically & Horizontally,” *Alexandria Eng. J.*, pp. 1–11, 2016, doi: 10.1016/j.aej.2016.10.006.

[91] J. Steinbrink, “Design and analysis of windings of electrical machines,” *SPEEDAM 2008 - Int. Symp. Power Electron. Electr. Drives, Autom. Motion*, no. July 2008, pp. 717–720, 2008, doi:

© COPYRIGHT UPM

10.1109/SPEEDHAM.2008.4581183.

[92] J.-S. Rincon-Tabares, J. C. Velasquez-Gonzalez, D. Ramirez-Tamayo, A. Montoya, H. Millwater, and D. Restrepo, “Sensitivity Analysis for Transient Thermal Problems Using the Complex-Variable Finite Element Method,” *Appl. Sci.*, vol. 12, no. 5, 2022, doi: 10.3390/app12052738.

[93] A. Rayed, B. Esakki, P. Arunkumar, S. Banik, and K. Aly, “Optimization of UAV structure and evaluation of vibrational and fatigue characteristics through simulation studies,” *Int. J. Simul. Multidiscip. Des. Optim.*, vol. 12, p. 17, Jan. 2021, doi: 10.1051/smdo/2021020.

[94] P. Witczak and M. Swiatkowski, “Transmission of Vibrations from Windings to Tank in High Power Transformers,” *Energies*, vol. 16, no. 6, 2023, doi: 10.3390/en16062886.

[95] E. A. Avallone and T. Baumeister, *Marks’ Standard Handbook for Mechanical Engineers*. McGraw-Hill, 1996. [Online]. Available: https://books.google.com.my/books?id=MLERAQAAMAAJ

[96] A. S. Murthy, N. A. Id, and J. Jasni, “Extraction of winding parameters for 33 / 11 kV , 30 MVA transformer based on finite element method for frequency response modelling,” no. August, 2020, doi: 10.1371/journal.pone.0236409.

[97] X. Liu, Y. Wang, J. Zhu, Y. Guo, G. Lei, and C. Liu, “Calculation of Capacitance in High-Frequency Transformer Windings,” *IEEE Trans. Magn.*, vol. 52, no. 7, pp. 14–17, 2016, doi: 10.1109/TMAG.2016.2522976.

[98] M. Popov, L. Van der Sluis, G. C. Paap, and H. De Herdt, “Computation of very fast transient overvoltages in transformer windings,” *IEEE Trans. Power Deliv.*, vol. 18, no. 4, pp. 1268–1274, 2003, doi: 10.1109/ICEMS12746.2007.4412335.

[99] X.-C. Wei, *Modeling and design of electromagnetic compability for high-speed printed circuit boards and packaging*, CRC Press. Rosewood Drive, Danvers: Boca Raton, 2017. [Online]. Available: https://www.ptonline.com/articles/how-to-get-better-mfi-results

[100] S. M. Hassan Hosseini, M. Vakilian, and G. B. Gharehpetian, “Comparison of transformer detailed models for fast and very fast transient studies,” *IEEE Trans. Power Deliv.*, vol. 23, no. 2, pp. 733–741, 2008, doi: 10.1109/TPWRD.2008.915795.

[101] Standards Development Committee of IEEE Electromagnetic Compatibility Society, “IEEE Standard for Validation of Computational Electromagnetics Computer Modeling and Simulations,” 2022.

[102] Z. Cheng, N. Takahashi, and B. Forghani, *Modeling and application of electromagnetic and thermal field in electrical engineering*. 2019. doi: 10.1007/978-981-15-0173-9.

© COPYRIGHT UPM

[103] G. Liang, H. Sun, X. Zhang, and X. Cui, “Modeling of transformer windings under very fast transient overvoltages,” *IEEE Trans. Electromagn. Compat.*, vol. 48, no. 4, pp. 621–627, 2006, doi: 10.1109/TEMC.2006.884537.

[104] J. R. Espinoza, C. Pérez-Rojas, and S. García-Martínez, “Validation of the transformer magnetic circuit model,” *2012 North Am. Power Symp. NAPS 2012*, no. 2, pp. 1–6, 2012, doi: 10.1109/NAPS.2012.6336432.

[105] R. Murugan and R. Ramasamy, “Understanding the power transformer component failures for health index-based maintenance planning in electric utilities,” *Eng. Fail. Anal.*, vol. 96, no. July 2018, pp. 274–288, 2019, doi: 10.1016/j.engfailanal.2018.10.011.

[106] G. H. Chitaliya and S. K. Joshi, “Finite Element Method for Designing and Analysis of the Transformer - A Retrospective,” *Int. Conf. Recent Trends Power, Control Instrum. Eng. PCIE*, pp. 54–58, 2013, doi: 03.LSCS.2013.7.524.

[107] H. M. Ahn, J. Y. Lee, J. K. Kim, Y. H. Oh, S. Y. Jung, and S. C. Hahn, “Finite-element analysis of short-circuit electromagnetic force in power transformer,” *IEEE Trans. Ind. Appl.*, vol. 47, no. 3, pp. 1267–1272, 2011, doi: 10.1109/TIA.2011.2126031.

[108] H. M. Ahn, Y. H. Oh, J. K. Kim, J. S. Song, and S. C. Hahn, “Experimental verification and finite element analysis of short-circuit electromagnetic force for dry-type transformer,” *IEEE Trans. Magn.*, vol. 48, no. 2, pp. 819–822, 2012, doi: 10.1109/TMAG.2011.2174212.

[109] J. Faiz, B. M. Ebrahimi, and W. Abu-Elhaija, “Computation of static and dynamic axial and radial forces on power transformer windings due to inrush and short circuit currents,” *IEEE Jordan Conf. Appl. Electr. Eng. Comput. Technol.*, pp. 1–8, 2011, doi: 10.1109/AEECT.2011.6132487.

[110] W. Fonseca, D. Lima, A. Lima, N. S. Soeiro, and M. V. A. Nunes, “Analysis of electromagnetic-mechanical stresses on the winding of a transformer under inrush currents conditions,” *Int. J. Appl. Electromagn. Mech.*, vol. 50, no. 4, pp. 511–524, 2016, doi: 10.3233/JAE-150044.

[111] K. Dawood, G. Komurgoz, and F. Isik, “Computation of the Axial and Radial forces in the Windings of the Power Transformer,” *Proc. - 2019 4th Int. Conf. Power Electron. their Appl. ICPEA 2019*, vol. 25, no. 27, pp. 1–6, 2019, doi: 10.1109/ICPEA1.2019.8911132.

[112] M. Arivamudhan and S. Santhi, “Analysis of Mechanical integrity in power transformer using statistical techniques,” *2019 IEEE Int. Conf. Electr. Comput. Commun. Technol.*, pp. 1–6, 2019, doi: 10.1109/ICECCT.2019.8869152.

[113] Y. Hodhigere, J S Jha, A. Tewari, and S. Mishra, “Finite Element Analysis-Based Approach for Stress Concentration Factor Calculation,” in *Proceedings of Fatigue, Durability and Fracture Mechanic*, 2018, pp.

© COPYRIGHT UPM

1–6. doi: 10.1007/978-981-10-6002-1.

[114] A. J. Muminovic, I. Saric, and N. Repcic, “Numerical Analysis of Stress Concentration Factors,” *Procedia Eng.*, vol. 100, pp. 707–713, 2015, doi: 10.1016/j.proeng.2015.01.423.

[115] W. J. Hussein and K. R. Hameed, “Finite-Element Calculation of Electromagnetic Forces in the Deferent Shapes of Distribution Transformers Winding Under Short Circuit Condition,” *J. Eng. Sustain. Dev.*, vol. 26, no. 3, pp. 44–61, 2022, doi: 10.31272/jeasd.26.3.6.

[116] C. Zhang, W. Ge, Y. I. Xie, and Y. Li, “Comprehensive Analysis of Winding Electromagnetic Force and Deformation During No-Load Closing and Short-Circuiting of Power Transformers,” *IEEE Access*, vol. 9, pp. 73335–73345, 2021, doi: 10.1109/ACCESS.2021.3068054.

[117] A. Nazari, “Leakage fluxes and mechanical forces calculation on the single phase shell- type transformer winding under over currents by 2-D and 3-D finite element methods,” *J. Electr. Eng.*, vol. 13, no. 4, pp. 1–8, 2013, [Online]. Available: http://www.jee.ro/index.php/jee/article/view/WT1364759317W5158931 5e44fa

[118] T. Dao and B. T. Phung, “Effects of voltage harmonic on losses and temperature rise in distribution transformers,” *IET Gener. Transm. Distrib.*, vol. 12, no. 2, pp. 347–354, 2018, doi: 10.1049/iet-gtd.2017.0498.

[119] Y. Deng, J. Ruan, Y. Quan, R. Gong, D. Huang, and C. Duan, “A Method for Hot Spot Temperature Prediction of a 10 kV Oil-Immersed Transformer,” *IEEE Access*, vol. 7, pp. 107380–107388, 2019, doi: 10.1109/ACCESS.2019.2924709.

[120] C. Liao, J. Ruan, C. Liu, W. Wen, and Z. Du, “3-D coupled electromagnetic-fluid-thermal analysis of oil-immersed triangular wound core transformer,” *IEEE Trans. Magn.*, vol. 50, no. 11, pp. 1–4, 2014, doi: 10.1109/TMAG.2014.2330953.

[121] W. H. Tang and Q. H. Wu, *Condition Monitoring and Assessment of Power Transformers Using Computational Intelligence*. 2011.

[122] K. Hameyer and R. Belmans, *Numerical modelling and design of electrical machines and devices*, vol. 37, no. 08. 2000. doi: 10.5860/choice.37-4527.

[123] K. Hameyer, J. Driesen, H. De Gersem, and R. Belmans, “The classification of coupled field problems,” *IEEE Trans. Magn.*, vol. 35, no. 3 PART 1, pp. 1618–1621, 1999, doi: 10.1109/20.767304.

[124] S. Wang, S. Wang, N. Zhang, D. Yuan, and H. Qiu, “Calculation and Analysis of Mechanical Characteristics of Transformer Windings under Short-Circuit Condition,” *IEEE Trans. Magn.*, vol. 55, no. 7, pp. 1–4,

© COPYRIGHT UPM

2019, doi: 10.1109/TMAG.2019.2898183.

[125] Y. Li, X. Yan, C. Wang, Q. Yang, and C. Zhang, “Eddy Current Loss Effect in Foil Winding of Transformer Based on Magneto-Fluid-Thermal Simulation,” *IEEE Trans. Magn.*, vol. 55, no. 7, pp. 1–5, 2019, doi: 10.1109/TMAG.2019.2897503.

[126] B. Zhang, N. Yan, S. Ma, and H. Wang, “Buckling strength analysis of transformer windings based on electromagnetic thermal structural coupling method,” *IEEE Trans. Appl. Supercond.*, vol. 29, no. 2, 2019, doi: 10.1109/TASC.2019.2893996.

[127] M. G. Pantelyat, “Coupled Magneto-Thermo-Mechanical Phenomena in Electromagnetic Devices : Main Interactions and their Graphical Representation,” *Int. Symp. Theor. Electr. Eng.*, pp. 13–14, 2013, [Online]. Available: http://hdl.handle.net/11025/11503

[128] S. D. Fabiyi, A. J. Falade, S. D. Fabiyi, and A. Abdulkarim, “Reliability Assessment of Power Transformers for Oshogbo Area Control Center in Nigeria,” *J. Res. Inf. Civ. Eng.*, vol. 14, no. 1, pp. 1066–1080, 2016, [Online]. Available: https://www.researchgate.net/publication/323541718

[129] S. Tenbohlen and J. Jagers, “Transformer reliability survey : Interim report, WG A2 . 37,” 2012.

[130] A. Van Schijndel, J. M. Wetzer, and P. A. A. F. Wouters, “Forecasting transformer reliability,” *Annu. Rep. - Conf. Electr. Insul. Dielectr. Phenomena, CEIDP*, pp. 577–582, 2006, doi: 10.1109/CEIDP.2006.311998.

[131] D. Carreno and D. Chhajer, “Transformer Winding Resistance Measurement: Field Challenges,” *Megger*, 2022. https://www.megger.com/en-ca/category-faq/transformer-winding-resistance-measurement

[132] Engr. Isaac Ojochogwu Onuh, “A Critical Assessment of Power Transformers Reliability in the Nigerian Electricity Supply Industry (A Case Study),” *Int. J. Eng. Res.*, vol. V8, no. 06, pp. 495–536, 2019, doi: 10.17577/ijertv8is060279.

[133] A. Bakshi and S. V. Kulkarni, “Analysis of buckling strength of inner windings in transformers under radial short-circuit forces,” *IEEE Trans. Power Deliv.*, vol. 29, no. 1, pp. 241–245, 2014, doi: 10.1109/TPWRD.2013.2272102.

[134] M. Calvário, Z. Li, and C. Guedes Soares, “Buckling strength of a composite material wave energy converter structure under slamming loads,” *Ocean Eng.*, vol. 241, no. August, 2021, doi: 10.1016/j.oceaneng.2021.110044.

[135] H. Xiao, Z. Yin, X. Chen, Z. Deng, P. Wang, and S. Chen,

© COPYRIGHT UPM

"Comprehensive analyses of buckling and stress failure of high-field pulsed magnets under biaxial Lorentz force body load," *Thin-Walled Struct.*, vol. 183, no. November 2022, p. 110341, 2023, doi: 10.1016/j.tws.2022.110341.

[136] A. Bakshi, "Effect of Width of Axial Supporting Spacers on the Buckling Strength of Transformer Inner Winding," *IEEE Trans. Power Deliv.*, vol. 34, no. 6, pp. 2278–2280, 2019, doi: 10.1109/TPWRD.2019.2914834.

[137] L. Ari, N. Wibawa, M. Ibadi, and H. Purnomo, "Static stress and fatigue life analysis of rocket trolley leaf spring using numerical simulation," *MATEC Web Conf. 402, 01003 4th ICETIR 2022*, vol. 01003, pp. 1–5, 2024, doi: https://doi.org/10.1051/matecconf/202440201003.

[138] M. Bagheri, B. T. Phung, and M. S. Naderi, "Impulse voltage distribution and frequency response of intershield windings," *IEEE Electr. Insul. Mag.*, vol. 32, no. 5, pp. 32–40, 2016, doi: 10.1109/MEI.2016.7552374.

[139] M. Eslamian, B. Vahidi, and S. H. Hosseinian, "Combined analytical and FEM methods for parameters calculation of detailed model for dry-type transformer," *Simul. Model. Pract. Theory*, vol. 18, no. 3, pp. 390–403, 2010, doi: 10.1016/j.simpat.2009.12.005.

[140] M. Ghaffarian Niasar and W. Zhao, "Impulse voltage distribution on disk winding: Calculation of disk series capacitance using analytical method," *7th IEEE Int. Conf. High Volt. Eng. Appl. ICHVE 2020 - Proc.*, 2020, doi: 10.1109/ICHVE49031.2020.9279969.

[141] N. F. M. Yasid, "The Characteristic of Frequency Response on Winding Faults and Configurations of Transformer," 2019.

[142] N. F. M. Yasid, N. Azis, M. F. M. Yousof, M. A. Talib, and A. S. Murthy, "Axial and Radial Force Distributions Computation in Disc-Type Winding Under Switching Surge," in *2022 EEE International Conference in Power Engineering Application (ICPEA)*, 2022, no. March, pp. 1–4. doi: 1.1109/ICPEA53519.2022.9744688.

[143] A. C. De Azevedo, I. Rezende, A. C. Delaiba, J. C. De Oliveira, B. C. Carvalho, and S. B. De Herivelto, "Investigation of transformer electromagnetic forces caused by external faults using FEM," *2006 IEEE PES Transmission and Distribution Conference and Exposition: Latin America, TDC'06*. 2006. doi: 10.1109/TDCLA.2006.311522.

[144] M. R. Feyzi and M. Sabahi, "Finite element analyses of short circuit forces in power transformers with asymmetric conditions," *IEEE Int. Symp. Ind. Electron.*, pp. 576–581, 2008, doi: 10.1109/ISIE.2008.4677272.

[145] Y. Wang, Z. Wang, and S. Fang, "Three-Dimensional Magnetic and Temperature Field Coupling Analysis of Dry-Type Transformer Core under Different Excitations," *Prog. Electromagn. Res. C*, vol. 95, no. August, pp. 75–89, 2019, doi: 10.2528/PIERC19070401.

© COPYRIGHT UPM

[146] H. Wheeler, “Formulas the Skin Effect,” *Proc. IRE*, vol. 30, no. 9, pp. 412–124, 1942, doi: 10.1109/JRPROC.1942.232015.

[147] Y. B. Zhang, Y. L. Xin, T. Qian, X. Lin, W. H. Tang, and Q. H. Wu, “2-D Coupled Fluid-Thermal Analysis of Oil-Immersed Power Transformers Based on Finite Element Method,” pp. 1060–1064, 2016, doi: 10.1109/ISGT-Asia.2016.7796532.

[148] Z. Guo and X. Shi, “Chapter 4 - Mechanical Behavior and Constitutive Relation of Reinforcement at Elevated Temperatures,” in *Experiment and Calculation of Reinforced Concrete at Elevated Temperatures*, Z. Guo and X. Shi, Eds. Boston: Butterworth-Heinemann, 2011, pp. 56–74. doi: https://doi.org/10.1016/B978-0-12-386962-3.10004-X.

[149] H. Zhang, B. Yang, W. Xu, S. Wang, G. Wang, and Y. Huangfu, “Dynamic deformation analysis of power transformer windings in short-circuit fault by FEM,” *IEEE Trans. Appl. Supercond.*, vol. 24, no. 3, pp. 5–8, 2014, doi: 10.1109/TASC.2013.2285335.

[150] T. Huang, J. J. Ruan, Y. J. Zhang, Y. D. Zhang, J. P. Liao, and Y. C. Hu, “Effect of geometry change on the deformation in C-shaped armatures through 3-D magnetic-structural coupling finite-element analysis,” *Conf. Proc. - 2012 16th Int. Symp. Electromagn. Launch Technol. EML 2012*, no. 2, pp. 1–5, 2012, doi: 10.1109/EML.2012.6325102.

[151] W. M. L. B. Naranpanawe, “Understanding the Moisture Temperature and Ageing Dependency of Power Transformer Winding Clamping Pressure,” 2018.

[152] H. Ye, Y. Gao, H. Wu, Y. Li, Z. Wu, and G. Ma, “Voltage Distribution in Power Transformer Winding under Transient Impulse,” *Adv. Eng. Res.*, vol. 124, pp. 375–378, 2017, doi: 10.2991/isaeece-17.2017.72.

[153] M. Samal, K. Lakshmi Prasanna, P. Mishra, and M. Mondal, “Accurate Estimation of Transformer Winding Capacitances and Voltage Distribution Factor Using Driving Point Impedance Measurements,” *IEEE Access*, vol. 12, no. August, 2024, doi: 10.1109/ACCESS.2024.3460968.

[154] V. Larin, D. Matveev, and A. Volkov, “Study of Transient Interaction in a System with Transformer Supplied from Network through a Cable: Assessment of Interaction Frequencies and Resonance Evolvement,” *J. Energy*, vol. 63, no. December, pp. 252–261, 2014, doi: https://doi.org/10.37798/2014631-4185.

[155] F. Yasid, N. Azis, F. Yousof, M. Talib, and A. Srikanta Murthy, “Electromagnetic Force Distribution Computations Due to Switching Surge in Disc-type Winding,” *Indones. J. Electr. Eng. Comput. Sci.*, vol. 30, pp. 659–669, Feb. 2023, doi: 10.11591/ijeecs.v30.i2.pp659-669.

[156] W. J. McNutt, T. J. Blalock, and R. A. Hinton, “Response of transformer windings to system transient voltages,” *IEEE Trans. Power Appar. Syst.*,

© COPYRIGHT UPM

vol. PAS-93, no. 2, pp. 457–467, 1974, doi: 10.1109/TPAS.1974.293992.

[157] Y. Li, W. Zhou, Y. Jing, and X. Sun, “Axial vibration analysis of power transformer active part under short-circuit,” *2011 Int. Conf. Electr. Mach. Syst. ICEMS 2011*, pp. 1–4, 2011, doi: 10.1109/ICEMS.2011.6073998.

[158] Z. Meng and Z. Wang, “The analysis of mechanical strength of HV winding using finite element method, part I calculation of electromagnetic forces,” *39th Int. Univ. Power Eng. Conf. UPEC 2004 - Conf. Proc.*, vol. 1, pp. 170–174, 2004, [Online]. Available: https://ieeexplore.ieee.org/document/1491985

[159] V. Behjat, A. Shams, and V. Tamjidi, “Characterization of power transformer electromagnetic forces affected by winding faults,” *J. Oper. Autom. Power Eng.*, vol. 6, no. 1, pp. 40–49, 2018, doi: 10.22098/joape.2018.2436.1210.

[160] F. Ren, S. Ji, and L. Zhu, “Experimental Research on Cumulative Deformation of Transformer Winding Induced by Short-Circuit Current Impacts,” 2019. [Online]. Available: https://api.semanticscholar.org/CorpusID:213144788

[161] X. Yu, Y. Tan, H. Wang, X. Wang, Y. Zang, and P. Guo, “Thermal analysis and optimization on a transformer winding based on non-uniform loss distribution,” *Appl. Therm. Eng.*, vol. 226, no. December 2022, p. 120296, 2023, doi: 10.1016/j.applthermaleng.2023.120296.

[162] R. Gong, J. Ruan, J. Chen, Y. Quan, J. Wang, and C. Duan, “Analysis and experiment of hot-Spot temperature rise of 110 kV three-Phase three-Limb transformer,” *Energies*, vol. 10, no. 8, 2017, doi: 10.3390/en10081079.

[163] S. Lee, J. Y. Lee, J. C. Yun, J. Y. Park, and J. H. Woo, “Development of thermal and structural design technology for a hermetically sealed oil transformer,” *WIT Trans. Built Environ.*, vol. 126, pp. 179–190, 2012, doi: 10.2495/SU120161.

[164] M. Li and S. J. Zinkle, “4.20 - Physical and Mechanical Properties of Copper and Copper Alloys,” in *Comprehensive Nuclear Materials: Volume 1-5*, vol. 1–5, 2012, pp. 667–690. doi: 10.1016/B978-0-08-056033-5.00122-1.

© COPYRIGHT UPM

APPENDICES

APPENDIX A

Simulink circuit

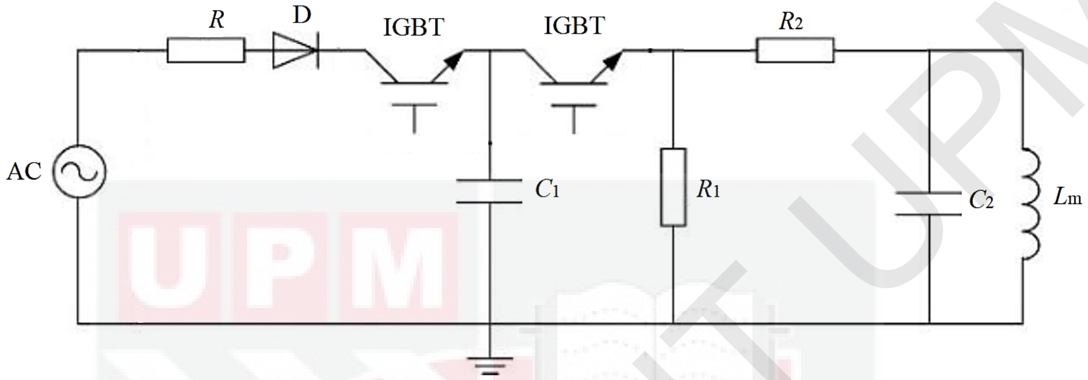

Figure A.1: Standard switching impulse voltage generator circuit

A series connection of 2 IGBTs with a diode was employed in the circuit to withstand negative voltage, forming the charging and discharging circuits. Each of the IGBTs included an anti-parallel diode for current tracing and protection. A current-limiting resistor, *r* was incorporated into the charging circuit. The IGBT at the charging side was turned ON to fully charge the primary capacitor, C_1 before the discharge. Additional wave-modulating components, inductances *L* and capacitance C_2 were also set. The discharge from C_1 induced a high-amplitude voltage across C_2 on the secondary side. Two resistors, R_1 and R_2 were placed in the circuit to control the wave-tail and -head. The SSI voltage was measured across the C_2. The specification of the SSI waveform generator circuit is shown in Table A.1.1.

© COPYRIGHT UPM

Table A.1.1: The impulse generator circuit specification for SSI waveform

Parameters	Units
The leakage inductance, L	0
The primary capacitance, C_1	10 µF
The wave modulating capacitance, C_2	1 µF
The modulating inductance, L_m	0.9 H
The current limiting resistor, R	1000 Ω
The wave-tail resistor, R_1	1155 Ω
The wave-head resistor, R_2	56 Ω
Amplitude of discharge voltage, U_{c1}	400 V

.

© COPYRIGHT UPM

APPENDIX B

Details of disc winding model material properties:

Properties of Outline Row 5: Copper

	A	B	C	D	E
1	Property	Value	Unit		
2	Material Field Variables	Table			
3	Density	7850	kg m^-3		
4	Isotropic Elasticity				
5	Derive from	Young's Modulus and Poisson...			
6	Young's Modulus	1.136E+11	Pa		
7	Poisson's Ratio	0.3			
8	Bulk Modulus	9.4667E+10	Pa		
9	Shear Modulus	4.3692E+10	Pa		
10	Strain-Life Parameters				
11	Display Curve Type	Strain-Life			
12	Strength Coefficient	5.73E+08	Pa		
13	Strength Exponent	-0.143			
14	Ductility Coefficient	0.492			
15	Ductility Exponent	-0.537			
16	Cyclic Strength Coefficient	7.19E+08	Pa		
17	Cyclic Strain Hardening Exponent	0.27			
18	Tensile Yield Strength	5E+07	Pa		
19	Tensile Ultimate Strength	2.06E+08	Pa		

Figure B.1: Copper properties

Properties of Outline Row 4: Kraft Paper

	A	B	C	D	E
1	Property	Value	Unit		
2	Material Field Variables	Table			
3	Density	930	kg m^-3		
4	Isotropic Elasticity				
5	Derive from	Young's Modulus and Poisson...			
6	Young's Modulus	1.1E+09	Pa		
7	Poisson's Ratio	0.001			
8	Bulk Modulus	3.674E+08	Pa		
9	Shear Modulus	5.4945E+08	Pa		
10	Strain-Life Parameters				
11	Display Curve Type	Strain-Life			
12	Strength Coefficient	4.07E-06	MPa		
13	Strength Exponent	12.3			
14	Ductility Coefficient	3.88			
15	Ductility Exponent	9.4			
16	Cyclic Strength Coefficient	3.2	Pa		
17	Cyclic Strain Hardening Exponent	0.003			
18	Tensile Yield Strength	10.9	MPa		
19	Tensile Ultimate Strength	3.3E+07	Pa		

Figure B.2: Kraft insulation paper properties

© COPYRIGHT UPM

Properties of Outline Row 3: Structural Steel

	A	B	C	D	E
1	Property	Value	Unit		
2	Material Field Variables	Table			
3	Density	7850	kg m^-3		
4	Isotropic Secant Coefficient of Thermal Expansion				
5	Coefficient of Thermal Expansion	1.2E-05	C^-1		
6	Isotropic Elasticity				
7	Derive from	Young's Modulus and Poisson...			
8	Young's Modulus	2E+11	Pa		
9	Poisson's Ratio	0.3			
10	Bulk Modulus	1.6667E+11	Pa		
11	Shear Modulus	7.6923E+10	Pa		
12	Strain-Life Parameters				
13	Display Curve Type	Strain-Life			
14	Strength Coefficient	9.2E+08	Pa		
15	Strength Exponent	-0.106			
16	Ductility Coefficient	0.213			
17	Ductility Exponent	-0.47			
18	Cyclic Strength Coefficient	1E+09	Pa		
19	Cyclic Strain Hardening Exponent	0.2			
20	Tensile Yield Strength	2.5E+08	Pa		
21	Compressive Yield Strength	2.5E+08	Pa		
22	Tensile Ultimate Strength	4.6E+08	Pa		
23	Compressive Ultimate Strength	0	Pa		

Figure B.3: Structural steel fixed support properties

© COPYRIGHT UPM

APPENDIX C

Details of settings in simulation:

1. The settings for object connections in the disc winding model.

Table C.1: Model Connections

Object Name	*Connections*
State	Fully Defined
Auto Detection	
Generate Automatic Connection on Refresh	Yes
Transparency	
Enabled	Yes

Table C.1 shows that the connections between objects are fully defined to ensure that no additional connections need to be manually set. Automatic detection and generation of connections are enabled, making it easier to handle complex models with many elements. Transparency is enabled which improves visual analysis during simulation.

Table C.2: Model Connections Contacts

Object Name	*Contacts*
State	Fully Defined
Definition	
Connection Type	Contact
Scope	
Scoping Method	Geometry Selection
Geometry	All Bodies
Auto Detection	
Tolerance Type	Slider
Tolerance Slider	0.
Tolerance Value	1.0479 mm
Use Range	No
Face/Face	Yes
Face-Face Angle Tolerance	75. °

© COPYRIGHT UPM

Face Overlap Tolerance	Off
Cylindrical Faces	Include
Face/Edge	No
Edge/Edge	No
Statistics	
Connections	616
Active Connections	616

Table C.2 shows that the contact type is defined as "Face-to-Face" with a tolerance of 1.0479 mm. This ensures proper alignment between geometrical features. Various tolerances and settings are optimised for accuracy, such as face angle tolerance and cylindrical face inclusion, ensuring that all contacts in the simulation are correctly resolved without overlap.

2. Details of mesh setup

Table C.3: Mesh setup

Object Name	*Mesh*
State	Solved
Display	
Display Style	Use Geometry Setting
Sizing	
Use Adaptive Sizing	Yes
Resolution	Default
Mesh Defeaturing	Yes
Defeature Size	Default
Transition	Fast
Span Angle Center	Coarse
Initial Size Seed	Assembly
Bounding Box Diagonal	469.03 mm
Average Surface Area	2140.5 mm²
Minimum Edge Length	2.0505 mm
Quality	
Check Mesh Quality	Yes, Errors
Error Limits	Standard Mechanical
Target Quality	Default (0.050000)
Smoothing	Medium

© COPYRIGHT UPM

Mesh Metric	None
Inflation	
Use Automatic Inflation	None
Inflation Option	Smooth Transition
Transition Ratio	0.272
Maximum Layers	5
Growth Rate	1.2
Inflation Algorithm	Pre
View Advanced Options	No
Statistics	
Nodes	2677711
Elements	1275257

Table C.3 shows that the mesh is fully solved which indicate that all elements in the model have been discretized appropriately. Adaptive sizing is enabled for more efficient meshing. The default physics and solver preferences are optimized for mechanical analysis and mesh quality is verified with medium smoothing to ensure accurate simulation results. The number of nodes and elements, 2,677,711 and 1,275,257 respectively, demonstrate a highly detailed mesh, suitable for precise simulations.

Table C.4: Mesh controls

Object Name	*Patch Conforming Method*	*Body Sizing*
State	Fully Defined	
Scope		
Scoping Method	Geometry Selection	
Geometry	492 Bodies	
Definition		
Suppressed	No	
Method	Tetrahedrons	
Algorithm	Patch Conforming	
Element Order	Use Global Setting	
Type		Element Size
Element Size		4.0 mm
Defeature Size		Default
Behaviour		Soft

© COPYRIGHT UPM

The body sizing is defined using tetrahedral elements, which are appropriate for complex geometries. The patch conforming algorithm ensures the mesh adheres to the geometry without distortion. With 492 bodies involved, the meshing process has been carefully configured to maintain accuracy while keeping the computational load manageable.

© COPYRIGHT UPM

3. Analysis settings

Table C.5: Transient Thermal Initial Condition

Object Name	*Initial Temperature*
State	Fully Defined
Definition	
Initial Temperature	Uniform Temperature
Initial Temperature Value	30. °C

Table C.5 outlines the initial condition for transient thermal analysis. The model begins with a uniform temperature of 30 °C to ensure that all parts of the model are at the same starting temperature. This uniformity is crucial for accurate thermal analysis, as it provides a controlled baseline for transient studies.

Table C.6: Transient Analysis Settings

Object Name	*Analysis Settings*
State	Fully Defined
Step Controls	
Number Of Steps	1.
Current Step Number	1.
Step End Time	2.5e-003 s
Auto Time Stepping	On
Define By	Time
Initial Time Step	1.e-006 s
Minimum Time Step	1.e-007 s
Maximum Time Step	1.e-005 s
Time Integration	On
Solver Controls	
Solver Type	Program Controlled
Weak Springs	Off
Large Deflection	On
Restart Controls	
Generate Restart Points	Program Controlled
Retain Files After Full Solve	No
Combine Restart Files	Program Controlled
Nonlinear Controls	

© COPYRIGHT UPM

Newton-Raphson Option	Program Controlled
Force Convergence	Program Controlled
Moment Convergence	Program Controlled
Displacement Convergence	Program Controlled
Rotation Convergence	Program Controlled
Line Search	Program Controlled
Stabilization	Program Controlled
--Method	Energy
--Energy Dissipation Ratio	1.e-004
--Activation For First Substep	No
--Stabilization Force Limit	0.2
Output Controls	
Stress	Yes
Surface Stress	No
Back Stress	No
Strain	Yes
Contact Data	Yes
Nonlinear Data	Yes
Nodal Forces	No
Contact Miscellaneous	No
General Miscellaneous	No
Store Results At	All Time Points
Result File Compression	Program Controlled
Damping Controls	
Stiffness Coefficient Define By	Direct Input
Stiffness Coefficient	0.
Mass Coefficient	0.
Numerical Damping	Program Controlled
Numerical Damping Value	0.1

The transient analysis is set to a single step, with a total simulation time of 2.5 milliseconds. Auto time-stepping is enabled, allowing the simulation to dynamically adjust time step based on the behaviour of the model. Solver settings are program-controlled, ensuring that the solver optimally handles the nonlinearity and deflection. Output controls specify that stress, strain, and contact data will be recorded at all time points, providing detailed results for post-processing and analysis.

© COPYRIGHT UPM

BIODATA OF STUDENT

Nurul Farahwahida bt Md Yasid obtained her B.Eng. and M.Eng. Degrees in Electrical Engineering from Universiti Tun Hussein Onn Malaysia (UTHM) in 2017 and 2019, respectively. She is currently pursuing Ph.D. degree in Electrical Power Engineering at Universiti Putra Malaysia. Her research interest includes high voltage equipment as well as condition-based monitoring of transformers using Frequency Response Analysis (FRA), Finite Element Method (FEM) and others.

© COPYRIGHT UPM

LIST OF PUBLICATIONS

Journals

Yasid, N. F. M., Azis, N., Yousof, M. F. M., Jasni, J., Talib, M. A., & Murthy, A. S. "Structural Deformation and Displacement of a Disc Winding Due to Standard Switching Impulse Voltage via Finite Element Method", *Pertanika Journal of Science & Technology,* Volume 32, Issue 2, pp. 781 – 795, 2024.

Yasid, N. F. M., Azis, N., Yousof, M. F. M., Jasni, J., Talib, M. A., & Murthy, A. S. "Electromagnetic force distribution computations due to switching surge in disc-type winding", Indonesian Journal of Electrical Engineering and Computer Science, vol. 30, no. 2, pp. 659–669, 2023.

Conference proceeding

N. F. M. Yasid, N. Azis, M. F. M. Yousof, M. A. Talib, and A. S. Murthy, "Axial and Radial Force Distributions Computation in Disc-Type Winding Under Switching Surge", *2022 IEEE International Conference in Power Engineering Application (ICPEA)*, pp. 1–4, 2022.

© COPYRIGHT UPM